Order Number 9000069

Thermodynamics of pyroxene solid solution: Synthesis of theory and experiments

Sykes, Julia Ann, Ph.D.

City University of New York, 1989

U·M·I
300 N. Zeeb Rd.
Ann Arbor, MI 48106

THERMODYNAMICS OF PYROXENE SOLID SOLUTION:

SYNTHESIS OF THEORY AND EXPERIMENTS

by

Julia Ann Sykes

A dissertation submitted to the Graduate Faculty
in Earth and Environmental Sciences in partial
fulfillment of the requirements for the degree of
Doctor of Philosophy, The City University of New York.

1989

This manuscript has been read and accepted for the Graduate Faculty in Earth and Environmental Sciences in satisfaction of the dissertation requirement for the degree of Doctor of Philosophy.

January 17, 1989
Date

S K Saxena
Chair of Examining Committee

January 19, 1989
Date

Daniel Habib
Executive Officer

Professor Cherukupalli E. Nehru

Professor David H. Speidel

Professor Alberto Dal Negro

Professor Allan Ludman

Supervisory Committee

The City University of New York

Abstract

THERMODYNAMICS OF PYROXENE SOLID SOLUTION:

SYNTHESIS OF THEORY AND EXPERIMENTS.

by

Julia Ann Sykes

Adviser: Professor Surendra K. Saxena

Theoretical modeling and experimental studies were undertaken to study the subsolidus relations in pyroxenes. Intercrystalline (two-pyroxene) and intracrystalline (orthopyroxene) reactions were used to develop graphical geothermometers and determine thermal histories.

Experimental phase equilibrium data on coexisting pyroxenes (700 to 1400°C) in the pyroxene quadrilateral have been used to model the solvus resulting in the following set of thermochemical data and simple mixture parameters (W_{ij}). Standard (T=298.15K) enthalpy and entropy of formation from the elements for metastable orthohedenbergite are -1416.8 kJ and 84.88 J/m/K respectively. The heat capacity is given by 114.67 + 17.09E-3 T - 31.40E5 T^{-2}. The W_{ij} data are: (Enstatite=1, diopside=2, ferrosilite=3, hedenbergite=4) Opx: $W_{12} = W_{21}$= 25; W_{13} = (13.1-0.015 T); W_{31} = (3.37 - 0.005 T); W_{23} = 20; W_{32} = 16; W_{24} = 5; W_{42} = 7; W_{34} = 15; W_{43} = 15; W_{14} = 60; W_{41} = 30-0.00834 T; Cpx: W_{12} = (25.484 + 0.0812 P); W_{21} = (31.216 - 0.0061 P); $W_{31} = W_{13}$ = 0; W14 = (9 .3 - 0.045 T); W_{41} = (-20.0 + 0.028 T); W_{23} = 24; W_{32} = 15; W_{24} = 12; W_{42} = 12; W_{34} = (16.941 + 0.00592 P); W_{43} = (20.697 - 0.00235 P).

Two graphical geothermometers have been constructed based on the hypothesis that Fe^{2+}-Mg exchange has a lower closure temperature than

the Ca-transfer. Quenched igneous rocks yielded similar temperatures for both geothermometers; plutonic rocks showed a lower closure temperature for the Fe^{2+}-Mg exchange; metamorphic rocks agreed with other geothermometers but gave mixed temperature relations.

Single crystal X-ray techniques were used to study isothermal Fe^{2+}-Mg disordering in two orthopyroxene samples, Fs62 and Fs82, at temperatures of 625, 675, 725°C and 525, 575 and 625°C respectively. The structural data provides an internal constraint on the degree of ordering. Disordering rate constants yielded activation energies of 49 and 51 kcal/mol respectively.

Time-temperature-transformation (TTT) diagrams have been calculated for the extent of ordering in the natural samples (Fs 62; Fs82), both from granulitic terranes. Calculated cooling rates are 140 and 11°/million years respectively; the latter is within geophysical expectations. Errors introduced and propagated by this method are estimated and it is believed these cooling rates can never be better than "order of magnitude"; equivalent to many geophysical estimates.

Acknowledgements

Firstly, a deeply felt thank you to my advisor, Professor S. K. Saxena. Since our first meeting at GSA in Indianapolis, Professor Saxena has been a source of strength and guidence. He has helped me through my early days of acclimation to Brooklyn, steered me through the intricacies of the City University system and has provided the advice necessary for me to achieve this goal.

I wish to thank the other members of my committee, A. Dal Negro, A. Ludman, C.E. Nehru and D. Spiedel. Professor Nehru provided both scientific advice and financial aid. His belief in me as a teacher has given me confidence in many aspects of my geological career. Professors Ludman and Spiedel greatly improved this text with their in depth reviews and gave to me new insight into several facets of this work. Professor Dal Negro supervised and reviewed the experimental work and his presence at my defence was greatly appreciated.

Experimental work for this dissertation was carried out during thr e wonderful summers at the Istituto di Mineralogy, Universita di Padova, Italy. My thanks are extended to A. Dal Negro, S.K. Saxena and G.M. Molin for making this possible. GianMario Molin is my scientific collaborator for the experimental work and I thank him for his help, advise and friendship. Further, my thanks for technical advice, friendship and hospitality are extended to all at the Istituto, especially Suzi, Enzo and Antonio.

In addition I would like to acknowledge grant #3502-85 from the Committee on Research Grants of GSA which enabled me to make my initial trip to Italy. Ginger Wandless at the U.S. Geological Survey, Reston

VA, prepared samples for study by the Transmission Electron Microscope. The U.S. Geological Survey also provided library facilities and sample identification.

Finally, I wish to thank my husband, Dr. G.L. Nord for his continued support and patience during the later stages of the formulation of this dissertation.

Table of Contents

List of Tables

List of Figures

Figure Number

List of Figures (Continued)

I. INTRODUCTION

Pyroxenes are common minerals in the crust and mantle and, therefore, a successful elucidation of theory and completion of experiments relating their composition and thermodynamic properties is of vital importance. Such basic research is important for studying the formation of the crust and mantle and could also make a contribution to the study of recent and fossil geotherms.

This study is concerned with two structural groups of the chain silicate, pyroxene, in the compositional quadrilateral, diopside, $CaMgSi_2O_6$; hedenbergite, $CaFeSi_2O_6$; enstatite, $Mg_2Si_2O_6$; and ferrosilite, $Fe_2Si_2O_6$. Orthopyroxene, has an orthorhombic *Pbca* structure and is essentially a solid solution of $MgSiO_3$-$FeSiO_3$. A solid solution may be defined as a homogeneous phase composed of different chemical substances whose concentrations may be varied (here Mg and Fe^{2+}) without the precipitation of a new phase (Upadhyaya and Dube, 1982). In natural orthopyroxenes, a small amount of Ca (<2%) is always present in the structure. Clinopyroxene is monoclinic in structure and consists of a wide range of compositions essentially in the four component system $CaMgSi_2O_6$-$CaFeSi_2O_6$-$Mg_2Si_2O_6$-$Fe_2Si_2O_6$ known as the pyroxene quadrilateral. In this study we shall be concerned with the high-Ca clinopyroxenes with a *C2/c* structure. The divalent cations in both subgroups lie in two non-equivalent octahedral sites, M1 and M2. Figure 1.1 shows a diagram of the pyroxene quadrilateral and the composition of the minerals of interest.

As a rock heats or cools, ion-exchange occurs between the various

minerals (intercrystalline) and between the sites within these minerals (intracrystalline). In pyroxenes, the intercrystalline exchange reactions between the end members enstatite ($Mg_2Si_2O_6$, orthopyroxene) and diopside ($CaMgSi_2O_6$, clinopyroxene) are fairly well understood and a phase diagram is shown in figure 1.2. At high temperatures, the reactions are quite complex, however, at the range of interest of this study (900-400°C) there is a simple solvus between orthoenstatite and diopside. At 900°C, for example, for compositions from pure enstatite to approximately 3 mole% diopside only orthopyroxene will be stable. Likewise from pure diopside to approximately 8 mole% enstatite only the clinopyroxene structure will be seen. At ranges between these extremes, both phases occur resulting in an intergrowth of the two structural groups, the proportions of each phase dependant on the initial composition of the rock or mineral. Experimental work has also been done on the hedenbergite-ferrosilite join in the 800-1000°C temperature range by Lindsley (1981). However, the topology of the solvus within the pyroxene quadrilateral is still in question.

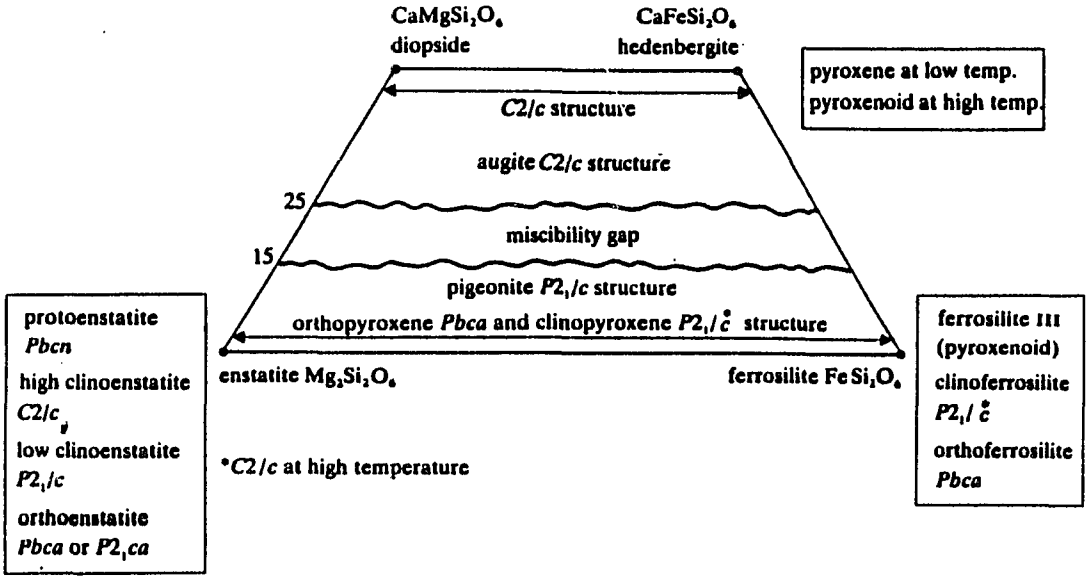

Figure 1.1. Structural and compositional relationships in the pyroxene quadrilateral; diopside-hedenbergite-enstatite-ferrosilite. From Deer, Howie and Zussman (1978).

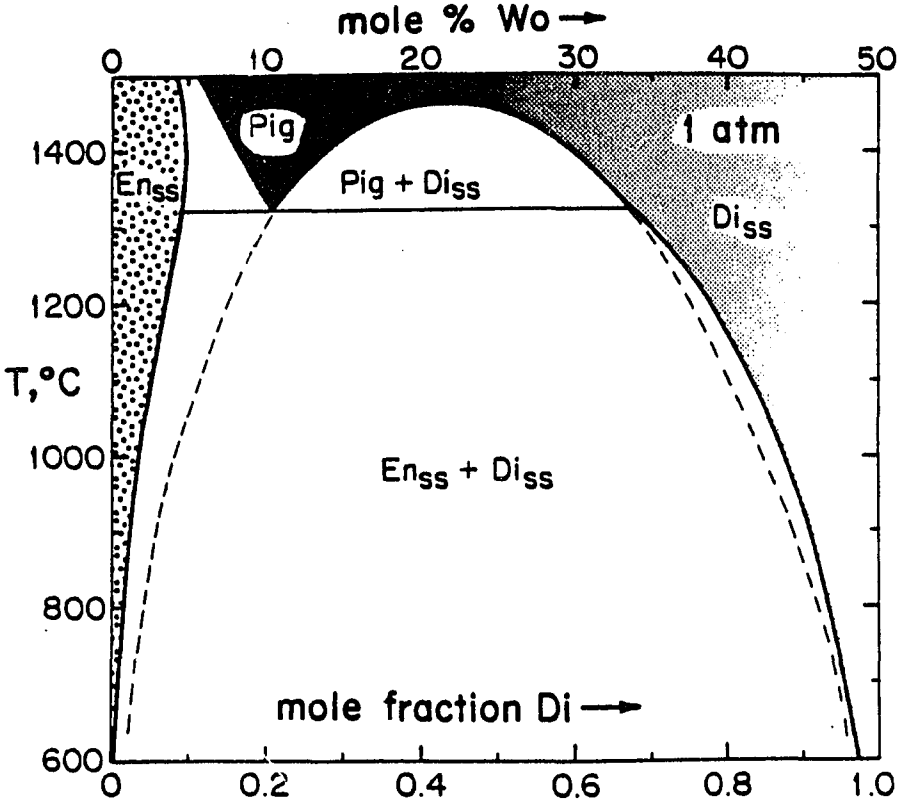

Figure 1.2. Phase relations for the diopside-enstatite join at one atmosphere. The dotted line indicates the metastable extension of the pigeonite-diopside solid solution field. From Lindsley (1983).

The first part of this thesis is to model the quadrilateral solvus using thermodynamics. The model will be tested by its ability to reproduce experimentally derived intercrystalline equilibrium ion distribution between the two structural groups of pyroxene. This work will then be applied to natural samples as geothermometry: a tool to measure past and present temperatures in the lithosphere. For igneous rocks it is used to obtain indications of crystallization temperatures, for metamorphic rocks, information on possible peak metamorphic temperatures. Geothermometry can help us understand various processes (i.e. crystal growth, deformation, and degassing) occurring in the earth, and thus help us model the formation and evolution of these regions.

The second part of this study concerns the intracrystalline ion-exchange. This, in comparison to intercrystalline ion-exchange, operates over extremely small lengths of diffusive paths and, therefore, continues to a much lower temperature. The temperature corresponding to the observed distribution of ions in the rock (assuming equilibrium is maintained) is defined as the closure temperature. If we assume (theoretical work and field observations discussed on page 43), that the diffusion kinetics of these reactions are different, distinct closure temperatures can be expected. When the cooling rate of the whole rock is fast (as in some volcanic rocks) there will be little difference between the closure temperatures for intercrystalline and intracrystalline reactions. For slow cooling (as in metamorphic rocks and deep-seated plutonic rocks) a large difference would be noted. For the whole system, the first reaction to slow significantly would be that of intercrystalline transfer reaction which determines the

Ca-distribution between clinopyroxene and orthopyroxene, next would be the intercrystalline exchange of Fe2+ and Mg across the phase boundary and finally, the intracrystalline exchange of Fe2+ and Mg between sites in both the orthopyroxene and clinopyroxene crystals. This would result in four different closure temperatures reflecting the cooling of the rock. Relative thermal histories, disequilibrium and kinetic rate processes could all be better understood by geothermometric analysis of these four events (see also Lasaga, 1983, Saxena, 1983b).

A schematic diagram of the different reaction rates, applicable for slowly cooled metamorphic rocks can be seen in Figure 1.3 (after Saxena, 1983b). If we assume that a rock cools with a constant rate, the rate would plot as a straight horizontal line on Figure 1.3. The rates of the four possible reactions are not constant:- (a) intercrystalline Ca ion-exchange between orthopyroxene and clinopyroxene, (b) intercrystalline Fe^{2+}-Mg ion-exchange between orthopyroxene and clinopyroxene and (c) and (d) the intracrystalline ion-exchange between the two non-equivalent sites in both clinopyroxene and orthopyroxene. At higher temperatures the rates of the ion-exchange reactions are faster than that of the cooling of the whole rock and equilibrium is maintained (Saxena, 1983b). As temperature decreases, the ion-exchange rates slow and eventually the reactions are slower than the cooling of the whole rock. At these low temperatures equilibrium ion-distribution is not maintained. The ion-exchange reactions do continue, however, but at a slower pace.

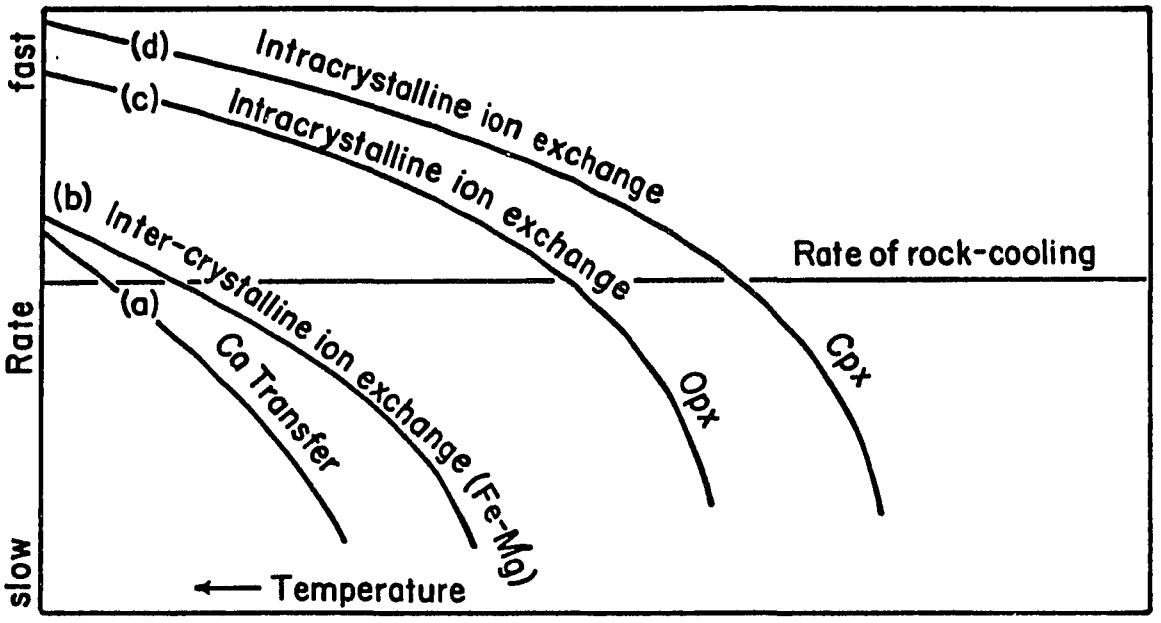

Figure 1.3. Relationship between intercrystalline and intracrystalline ion exchange reactions. The figure shows the relative rates of (a) Ca transfer, (b) Fe-Mg exchange between crystals, (c) Fe-Mg exchange between M1 and M2 sites of orthopyroxene and (d) Fe-Mg exchange between M1 and M2 sites of clinopyroxene and of the cooling of the rock. After Saxena (1983b).

The intracrystalline exchange reaction in orthopyroxene is studied experimentally in the second part of this thesis, and kinetic rates and activation energies for the reaction are derived. This information is important to understand the processes occurring within the pyroxene crystal and how fast these can occur.

These two areas of concentration, although both concerning pyroxenes, have tended to be (and are continuing to be), studied independently by experimental methods. This is because it is difficult to determine site occupancies of a single phase in multiphase materials; no microtechnique is available. The urgency regarding the experiments in, and the completion of, a thermodynamic model for the system diopside-enstatite-ferrosilite-hedenbergite,is clearly recognized (see especially papers by Lindsley and coworkers e.g. Lindsley, 1983, Turnock and Lindsley, 1981). Solutions to many petrogenetic problems pertaining to the formation and evolution of the earth's crust and mantle are awaiting the completion of a pyroxene-geothermometer, consistent with both thermodynamic data and site-occupancy data. This goal can be achieved both economically and rapidly if the data on site occupancies are available along with the phase equilibrium data (see also Davidson and Lindsley, 1985, Davidson, 1985). Such a model is then a combination of macroscopic parameters (i.e. the total Gibbs Free Energy) and microscopic parameters (i.e. the environments of the atoms in the sites and their interactions).

The third part of this thesis is an attempt to obtain a consistent set of equilibrium site occupancies taking into account experimental methods, temperatures and times of heating, and composition. This can then be used to model the pyroxene quadrilateral incorporating the site

occupancy data. Theory relating the inter- and intra-crystalline ion-exchange will be discussed in the fourth section of this thesis.

With the sucessful completion of all this work, a complete thermal history of any pyroxene bearing rock can be obtained. The work is applied to the natural samples by means of time-temperature-transformation (TTT) diagrams and a thermal cooling history of the pyroxene, and hence of the rock, can be obtained. General application to natural systems is beyond the scope of this thesis but an illustration of the method and some of the inherent problems are discussed in the final section. It is hoped that the cooling histories of natural systems can be developed in future research.

II. PYROXENE PHASE EQUILIBRIA; A MACROSCOPIC MODEL.

Kretz (1961) showed that the distribution of Mg and Fe^{2+} in coexisting orthopyroxenes and clinopyroxenes is different in igneous rocks from that in metamorphic rocks. Since then, many attempts have been made to establish a quantitative relationship between the Mg-Fe^{2+} distribution and the pressures and temperatures of pyroxene crystallization or thermal history. The completion of this work is important because pyroxenes are abundant in both igneous and metamorphic rocks and, therefore, a pyroxene geothermometer can be used successfully in many terranes and for the comparison of various areas.

During the last decade a plethora of two-pyroxene geothermometers has been developed. These include:- Davidson (1985); Davidson and Lindsley (1985); Fonarev and Graphchikov (1982); Kretz (1963, 1982); Lindsley (1983); Lindsley and Anderson (1983); Powell (1978); Ross and Huebner (1975); Saxena (1976); Saxena and Nehru (1975); Wells (1977); Wood and Banno (1973). These geothermometers can be subdivided according to their approach: directly calibrated methods; natural samples; and internally consistent data set methods.

The directly calibrated method uses experimental data derived in the laboratory which is then applied directly to the rock. Inconsistencies occur between the various experimental results. A problem in this method is that the experiments are usually carried out at relatively high temperatures and pressures, in order for equilibration to occur in a reasonable length of time. However, the geothermometers thus developed are then applied to rocks that experienced conditions below these temperatures with simple

extrapolations being performed.

The natural samples method can be used in rocks where coexisting orthopyroxene and clinopyroxene are found, along with other mineral phases that can be used for geothermometry; an estimate of the temperature and pressure of equilibration can thus be made. These results can then be used to develop a graphical geothermometer. The model can be tested by its ability to reproduce the experimental data.

The internally consistent data set method uses thermochemical data to produce a thermodynamic model for the system. The values calculated for the model are adjusted to agree with the available experimental and natural data on mineral equilibria.

In this thesis the third method is being re-examined. The reason for the addition of another model is to formulate a thermodynamic data set consistent with all the experimental and thermochemical data and to use this to produce a graphical geothermometer, the easiest to use. Lindsley (1983), developed a graphic geothermometer, but the close spacing of the lines, especially for orthopyroxene, makes the graph somewhat difficult to use. The thermochemical model developed in this thesis, once determined, can be used to easily produce distribution data for all compositions with changing temperature and pressure. These data can be used to produce various graphs with an emphasis on clear, easy-to-utilize methods of estimating the temperature and pressure of natural samples. In addition, this data set can be used to study the different closure temperatures for the Mg-Fe^{2+} ion-exchange reaction and Ca-transfer reaction occurring in the system.

A major problem in correlating the compositions with pressure and temperature, for the pyroxene system, is the difficulty in designing

suitable solution models for the two multicomponent pyroxenes (Saxena, 1983a). For quadrilateral pyroxenes, an attempt to describe in moles the chemical composition of the four end member components meets with the obvious difficulty of an extra component because compositionally the pyroxenes belong to a ternary ($MgSiO_3$-$FeSiO_3$-$CaSiO_3$) system. In order to categorize the pyroxenes completely we have to use a reciprocal solution methodology (Wood and Nicols, 1978) which would involve components with explicit sites such as $Fe(M1)Fe(M2)Si_2O_6$, $Mg(M1)Mg(M2)Si_2O_6$, $Mg(M2)Fe(M1)Si_2O_6$, $Fe(M2)Mg(M1)Si_2O_6$, $Ca(M2)Mg(M1)Si_2O_6$ and $Ca(M2)Fe(M1)Si_2O_6$.

Davidson and Lindsley (1985), Davidson (1985), Davidson et al. (1982), and Lindsley et al. (1981) have succeeded in constructing models that quantitatively express binary solution properties. They used a solution model for non-convergent site disorder as first proposed by Thompson (1969, 1970). This leads to the calculation of the free energy of the quadrilateral pyroxenes derived from pair interactions of Fe^{2+}, Mg and Ca on the two non-equivalent sites M1 and M2.

However, in this section of the thesis I wish to develop a model with an internally consistent data set that is not dependent on site occupancy data as much of this is currently being revised (see Chapters III, p 71 and IV, p 146). In Chapter V (p 166), the modeling of two pyroxene phase equilibria with respect to site occupancies will be discussed.

A. Method of Multicomponent Phase Equilibria Modeling

Calculations of the temperature and pressure of a reaction in P-T space are utilized in the various fields of geology, especially

geochemistry and petrology. Today, many examples of multiple reactions in P-T space are seen in the form of elaborate "spider web" type diagrams. Some thermochemical data are now available for the majority of minerals found in the earth, either directly available from calorimetry or derived from the P-T diagrams.

Recent advances in computing have enabled the method of Gibbs Free Energy minimization to be used to advantage. For a certain system, thermochemical data on all of the end members and all of the possible solid solution parameters within the system are used. A computer program (described later) then determines all the possible assemblages that could occur at a determined temperature and pressure, and the free energy for each of these assemblages is calculated. As the system approaches chemical equilibrium, total free energy approaches a minimum and, therefore, the most stable assemblage for that particular set of parameters is known. This is then compared to experimental data on the system and the various thermochemical parameters are changed until a close fit of the model to the data is obtained. For this method no specific assemblages need to be defined.

The method is especially important when solid solutions are involved. It can be used to advantage when several solid solutions occur in a given system as ternary and quaternary solutions can be calculated from the binary solutions (Kohler formulation is used and will be discussed later).

There are several restrictions associated with the use of this method. Firstly, the thermochemical data are of prime importance. This data base is very extensive and contains all recent experimental work and is believed to be the best available. Secondly, the calculations

yield assemblages with the minimum Gibbs Free Energy. These assemblages sometimes do not correspond to those found in nature or produced in laboratory experiments. Some natural assemblages are metastable, i.e. pigeonite in low-temperature rocks, and, therefore do not represent the lowest Gibbs Free Energy assemblage for the rock. Metastability is not considered in the model because kinetics are not included. An associated problem involves the actual energies involved in forming a new phase e.g. the energy for nucleation. These energies may be very high and, therefore, a phase may not nucleate either in nature or in laboratory experiments but be the stable phase when only the Gibbs Free Energy is considered. However, these problems can be avoided if careful consideration is given to the results obtained from the calculations. The method is a valid and powerful tool. In all the examples in this thesis, both the experimental data and the natural samples have been considered, and assumptions, when made, have been stated.

Gibbs Free Energy minimization is used in this thesis to constrain the solid solutions in the pyroxene quadrilateral and is compared to the experimental data known for this system. It can also be used to monitor the interactions of two or more hypothetical solutions. An example of this is provided on page 23. This example uses the simple case of two interacting binary solutions and shows the effects of changing the individual solution models from ideal to strongly negative or positive.

1. Solid Solutions

Orthopyroxene forms a continuous solid solution between $MgSiO_3$-$FeSiO_3$ by the substitution of the two cations Mg and Fe^{2+}. A solid

solution is not a mechanical mixture and the individuality of the dissolving species is lost in the solution. For a solid solution, the stability of the solution depends on how alike the substituting cations are. If the exchanged cation and the original have the same charge and nearly the same size a stable (continuous) solid solution occurs readily (such is the case with orthoyroxene). Overall the symmetry does not change, however, microscopic details (such as bond lengths) may differ within the solution. If the exchanged cations are very different the structure will not be stable and a second phase will exsolve.

When two or more components are mixed together there is a change in the thermodynamic properties; the entropy will change due to the increased number of ways the atoms can be distributed and the enthalpy (or internal energy) will be affected by the preference of the atoms for their own kind or their opposite kind. Hence the overall free energy will change. The difference between the free energy of the solution and that of a mechanical mixture of the pure end members (both with the same proportions of end members) is called the "free energy of mixing", G^m.

$$\Delta G^m = G_{\text{real solution}} - (\text{sum of free energies of end members})$$

for a solution A-B

$$\Delta G^m = (X_A \bar{G}_A + X_B \bar{G}_B) - (X_A G_A^0 + X_B G_B^0)$$

$$\text{or} \quad \Delta G^m = X_A(\bar{G}_A - G_A^0) + X_B(\bar{G}_B - G_B^0) \qquad (2.1)$$

where, X_i is the mole fraction of component i, $\bar{G}_i$ is the molar free

energy of component i in the solution, and G_i^0 is the molar free energy of component i in the chosen standard state. The energy of mixing can be related to enthalpy and entropy by:

$$\Delta G^m = \Delta H^m - T\Delta S^m$$

The activity of component i, a_i, is related to the free energy by

$$G_i = G_i^0 + RT\ln a_i \qquad (2.2)$$

where R is the gas constant and T is temperature in degrees Kelvin. This can also be stated in terms of the chemical potential μ

$$\mu_i = \mu_i^0 + RT\ln a_i \qquad (2.3)$$

For an ideal solution the activity is equal to the mole fraction, $a_i = X_i$. In this case there is no change in enthalpy of mixing, the entropy of mixing is always positive, and hence the change in free energy of mixing is always negative. In addition, the volume of mixing for an ideal solution is also zero. The ideal solution is a useful reference state (see Fig. 2.1a).

The deviation from ideality can be expressed by

$$a_i = X_i\gamma_i \qquad (2.4)$$

where γ_i is the activity coefficient. The activity coefficient approaches 1 as the solution approaches ideality. The excess

thermodynamic functions may be defined as the difference between that of the real solution and that of the ideal solution. Again considering a binary solution A-B, the excess molar free energy of the solution, G^{xs}, is given by:

$$G^{xs} = \Delta G^{m}_{\text{real solution}} - \Delta G^{m}_{\text{ideal solution}}$$

therefore the excess free energy can be defined as

$$G^{xs} = RT(X_A \ln\gamma_A + X_B \ln\gamma_B) \qquad (2.5)$$

Two types of non-ideal solutions can be seen in Fig. 2.1b and 2.1c.

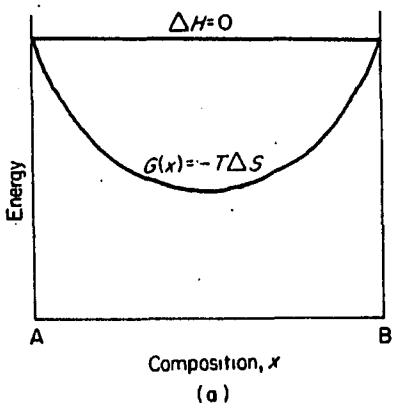

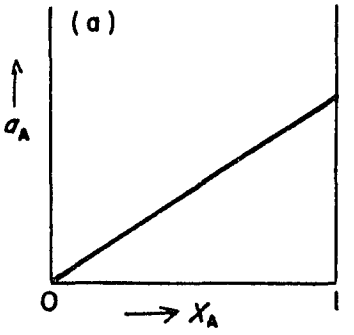

a) Ideal Solution

$\Delta H = 0$

$a_i = X_i$

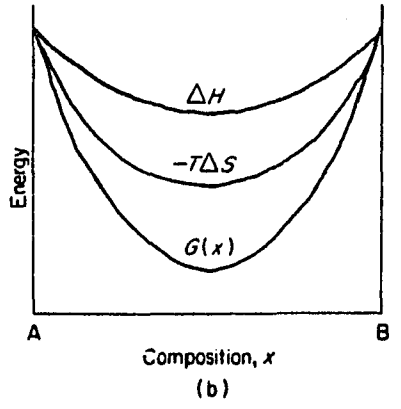

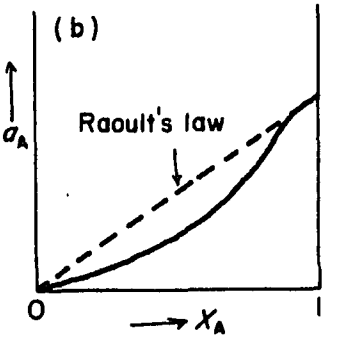

b) Solid Solution (non-ideal)

$\Delta H < 0$

$a_i < X_i$

attraction between A and B

C) Unmixing

$\Delta H > 0$

$a_i > X_i$

repulsion of A and B atoms

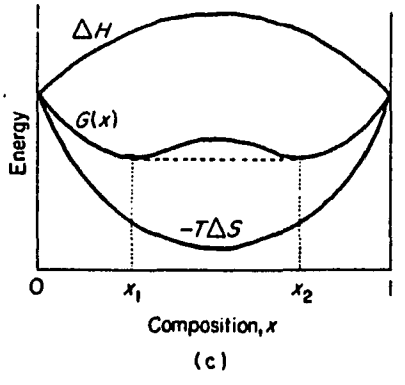

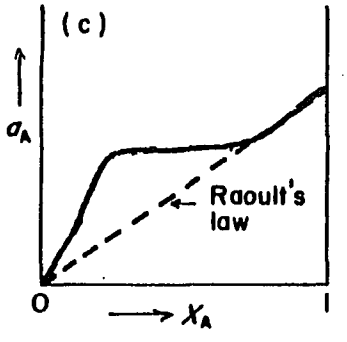

Figure 2.1 Free energy and activity diagrams as a function of mole fraction. After Putnis and McConnell (1980).

2. Combination of Binary Solution Models

It is necessary to use certain solution models to relate the observed compositional variables to the thermodynamic properties of mixing. Guggenheim (1937) suggested that G^{XS} can be expressed as a polynominal in X

$$\Delta G^{XS} = X_1X_2(A_0 + A_1(X_1 - X_2) + A_2(X_1 + X_2)^2 + ...) \qquad (2.6)$$

and in his book in 1967 reduced this equation for the simple mixture model as

$$\Delta G^{XS} = WX_1X_2 \qquad (2.7)$$

where W is the simple mixture parameter and is a function of pressure and temperature. For an ideal solution W=0; for a case where ΔG is negative and there is an attraction between A and B atoms W is negative; for exsolution, i.e. a repulsion of A and B atoms, W is positive. For exsolution to actually occur, $W \geq 2 \times R \times T$. At 800°C, W is approximately 4000 Joules (J), therefore, at any value of W ≥4000 J, exsolution will occur.

These solution models can then be combined. A comparison of the various calculations that can be used to combine solutions is given by Fei et al., (1986). The model used in this thesis is that of Kohler (1960) except that the ternary and other high order constants have been ignored. These high order constants are very difficult to evaluate and theoretical modeling of the values indicate that they have very little influence on the position of bimodal curves in the ternary system

(Saxena, 1973). In addition, experimental values obtained for several organic solutions (no data is available on crystalline solutions) have been determined to be negligible. Kohler (1960) proposed that the excess Gibbs Free Energy of mixing of a ternary solution (1-2-3) may be given by:

$$\Delta G^{xs}_{123} = (1-X_1)^2 \Delta G^{xs}_{23} + (1-X_2)^2 \Delta G^{xs}_{13} + (1-X_3)^2 \Delta G^{xs}_{12} \qquad (2.8)$$

where ΔG^{xs}_{ij} refers to the excess free energy of the binary mixture at composition X^o_i , X^o_j such that:

$$X^o_i = 1 - X^o_j = X_i/(X_i + X_j) \qquad (2.9)$$

In general for a multicomponent system we have,

$$\Delta G^{xs}_{12..N} = \Sigma_{i=1} \Sigma^{N}_{j>i} (X_i + X_j)^2 \ (\Delta G^{xs}_{ij}) \qquad (2.10)$$

Note that this formulation leaves the choice of binary solution models to the user. The binary model need not be the same for every binary solution. As compared to Wohl's (1953) multicomponent model which has been used, for example, by Ganguly & Saxena (1984), we find the Kohler formulation more convenient. It remains to be seen, however, whether its predictive ability for highly skewed (asymmetric) systems is any good. Barron's (1978) use of this formulation for melt systems has been quite successful. From expression (2.10) one obtains the following expression for the activity coefficient of component i

$$RT\ln\gamma_i = \Sigma_{j=i}(X_i + X_j)[RT\ln\gamma_{ij} + (1 - X_i + X_j)\ \Delta G^{xs}_{ij}] - (X_j + X_i)^2\ \Delta G^{xs}_{jk} \tag{2.11}$$

3. Method of Gibbs Free Energy Minimization

The method uses linear algebraic techniques that can be carried out rapidly on a computer. The program used in this thesis, SOLGASMIX, has been developed by G. Eriksson and S.K. Saxena. More detail on the method can be found in White et al. (1958), Van Zeggeren and Storey (1970), and Eriksson and Rosen (1973). This method has been used successfully; see Wood and Holloway (1982) and Saxena and Eriksson (1983). The thermodynamics follows that of Saxena (1982).

a. Thermodynamics

For a system, the total Gibbs free energy, G, can be expressed as

$$G = \Sigma n_i G_i = \Sigma n_i \mu_i \tag{2.12}$$

where n_i denotes the number of moles of i and μ_i is the chemical potential of i. If we consider a system with one ideal gas phase,"g", "q" liquid and solid solutions and "s" pure condensed phases, the total free energy of the system is

$$G = G^g + G^q + G^s \tag{2.13}$$

where, the total free energy for the gas phase G^g

$$G^g = \Sigma n_i G^o_{fi} + \Sigma n_i (RT\ln P + RT\ln X_i) \tag{2.14}$$

where T is temperature (K), P is pressure, R is the gas constant, G^o_{fi} is the standard Gibbs free energy of component i at 1 bar and T from elements in their standard state and X_i is the mole fraction of component i. For the solutions

$$G^q = \sum_{p=1}^{q} \sum_{i=1}^{m_p} n_{pi}[(G^o_{fi})_{pi} + RT\ln X_i) \tag{2.15}$$

(where n_{pi} is n_i in the pth phase, m_p is the total number of components in the pth phase), and for pure solids,

$$G^s = \Sigma_{p=1}^{s} n_{pi} (G^o_{fi})_{pi} \tag{2.16}$$

These equations may be combined by counting the phases consecutively, p=1 for the gas phase, from p=2 to p=(q+1) for the solid and liquid mixtures up to p = (q+s+1) for the last pure phase. For the total system

$$G = \sum_{p=1}^{1} \sum_{p=1}^{m_p} n_{pi} \left\| G^o_{fpi} + RT\ln P + \ln(n_{pi}/N_p) \right\| + \sum_{p=2}^{q+1} \sum_{i+1}^{m_p} n_{pi}[G^o_{fpi} + \ln X_i]$$

$$+ \Sigma_{p=q+2}^{q+s+1} \Sigma_{i=1}^{m_p} n_{pi} G^o_{fpi} \tag{2.17}$$

where N_p is the total amount of substances in the pth phase.

According to the free energy minimization method, the above

equation is minimized with the mass balance relationships

$$\sum_{p=1}^{q+s+1} \sum_{i=1}^{m_p} n_{pi} A_{pij} = b_j \qquad (j=1,2.....l) \qquad (2.18)$$

where A_{pij} represents the number of atoms of the jth element in a molecule of the ith component in the pth phase, l is the total number of elements and b is the initial amount of the element.

For each elememt j, in a pth phase we have

$$\sum_{i=1}^{m_p} n_{pi} A_{pij} - b_{pj} = 0 \qquad (2.19)$$

This is multiplied by an undetermined constant λ (Lagrangian multiplier) and the expression is summed up over all j, giving

$$\sum_{p=1}^{q+s+1} \left| \lambda_{pj} \left(\sum_{i=1}^{m_p} n_{pi} A_{pij} - b_{pj} \right) \right| = 0 \qquad (2.20)$$

This equation, added to that for the total free energy and partially differentiated (P,T,nj) yields several linear equations as shown below

For the gas phase

$$G^{o}_{fi} + RT\ln P + RT\ln X_i + \sum_{i=1}^{j} \lambda_j A_{ij} = 0 \qquad (2.21)$$

For the liquid and solid solutions

$$G^{o}_{fi} + RT\ln X_i + \sum_{i=1}^{j} \lambda_j A_{ij} = 0 \qquad (2.22)$$

For the pure phases

$$G^{o}_{fi} + \sum_{i=1}^{j} \lambda_j A_{ij} = 0 \qquad (2.23)$$

There will be as many equations as there are components (m_p). In addition there will be "s" equations for the pure phases, "1" material balances and other equations resulting from

$$\Sigma X_i = 1.0 \qquad (2.24)$$

b. Modeling of Binary Solutions

As an example of the SOLGASMIX program and as a useful illustration of the distribution of species between two coexisting non-ideal solutions, a series of diagrams has been reproduced in Fig. 2.2. A printout of the program is shown in Table 2.1. The printout shows the input amounts, in this case equal amounts of enstatite and ferrosilite. We have also inputted a negative amount of silica to ensure olivine is produced. (This is the opposite of the effect of adding silica to olivine in the hopes of producing orthopyroxene in an experimental run.) The second column shows the equilibrium amount in moles of the equilibrium assemblage for this particular T and P and thermochemical parameters. In this case, only olivine and orthopyroxene are stable within the system. The third column shows the mole fraction (clinopyroxene is not an equilibrium mineral as it is not present in the second column and, therefore, can be ignored in this column) and the final column shows the activity of the phases. Below this the entropy, enthalpy and excess energy loss are noted, the density of the phases produced and the average density for the whole system. The mole

fractions in the ternary pyroxenes are stated next, important for modeling the pyroxene system and finally, in this case, the distribution constant between olivine and orthopyroxene are noted.

Figure 2.2 illustrates the effect of changing the simple mixture parameter "W". For each case two diagrams have been drawn, the upper showing the plot of the mole fraction of iron in orthopyroxene (X-axis) against the mole fraction of iron in olivine (Y-axis). The lower diagram shows the variation in K_D against Fe/(Fe+Mg) for the whole system. The values of olivine and orthopyroxene used in this model are consistent with Chatterjee and Saxena, (1987).

The first figure shows the ideal solution case, i.e. all 4 values of W (Enstatite (En)-Ferrosilite (Fs); Fs-En; Fosterite (Fo) -Fayalite (Fa); Fa-Fo) are zero. There is a constant K_D for the distribution of elements between the olivine and the orthopyroxene. The plot of X_{Ol}^{Fe} against X_{Opx}^{Fe} shows the expected regular trend with Fe^{2+} going preferentially into the olivine. The thermochemical data for this example predict that only olivine will be stable at high iron ratios. The following diagrams indicate the differences caused by changing the W_{ij} parameters.

Of special interest are 2.2.e and 2.2.f. Although both binary solutions are strongly non-ideal the resulting distribution and K_D are almost identical to 2.2.a. Such instances as these can cause problems in modeling the systems as the true binary solutions could be very different than those chosen for the model. This effect will be much more complex when three or more solutions are being considered. For this reason the binary solutions quoted later in this paper for the pyroxene system can only be regarded as one set that reproduce the

experimental data. (However, W_{ij} values that are highly different from the theoretically expected values have not been accepted.) A second set of binary solutions may be possible which satisfy the data. However, as this data set extends to other phases and compositions the chances of several models reproducing the same data set decrease significantly and a complete thermodynamic model can be postulated. In addition, this set of figures is very useful in the modeling process to give an indication of the direction to change the binary solutions.

It is also to be noted that for 2.2.b, g, i, j, amd m, orthopyroxene is stable at high iron ratios, whereas, for 2.2.h. orthopyroxene ceases to be a stable phase at a much lower iron ratio and only olivine will be formed.

Table 2.1 Printout of SOLGASMIX

```
T = 1073.00 K
P = 6.00000E+03 BAR

THE SOLUTION IS NUMERICALLY UNSTABLE

                INPUT AMOUNT     EQUIL AMOUNT   MOLE FRACTION      ACTIVITY
                    MOL              MOL
MGSI.5O2        0.00000E+00      0.15771E+02     0.39423E+00     0.39425E+00
FESI.5O2        0.00000E+00      0.24233E+02     0.60577E+00     0.60582E+00
                                                 MOLE FRACTION      ACTIVITY
MGSIO3.OPX      0.50000E+02      0.34239E+02     0.57051E+00     0.57058E+00
FESIO3.OPX      0.50000E+02      0.25775E+02     0.42949E+00     0.42956E+00
                                                 MOLE FRACTION      ACTIVITY
MGSIO3.CPX      0.00000E+00      0.00000E+00     0.40230E+00     0.48968E+00
FESIO3.CPX      0.00000E+00      0.00000E+00     0.28982E+00     0.42325E+00
                                                 MOLE FRACTION      ACTIVITY
SIO2           -0.20000E+02      0.00000E+00                     0.62180E+00
COESITE         0.00000E+00      0.00000E+00                     0.35674E+00

ENTHALPY OF REACTION = 7.9263E+03 KJ
ENTROPY OF REACTION = 1.2606E+04 J.K-1
ENERGY LOSS = -4.1679E+03 KJ

ENTHALPY OF REACTION = 1.8581E+06 KJ
ENTROPY OF REACTION = -3.6541E+01 J.K-1
ENERGY LOSS =
PHASE                            DENSITY
OLIVINE                         3.92758
ORTHOPYROXENE                   3.55077
AVER DENSITY                    3.70148
   PHASE    DISTRIBUTION
MOLE FRACTIONS IN THE TERNARY PYROXENES:
MGSIO3.OPX  0.57051E+00 .50DI       0.00000E+00 FESIO3.OPX  0.42949E+00
FESIO3/(FESIO3+MGSIO3) =  0.42949E+00
DISTRIBUTION CONSTANTS:
OL-OPX  0.48993E+00
```

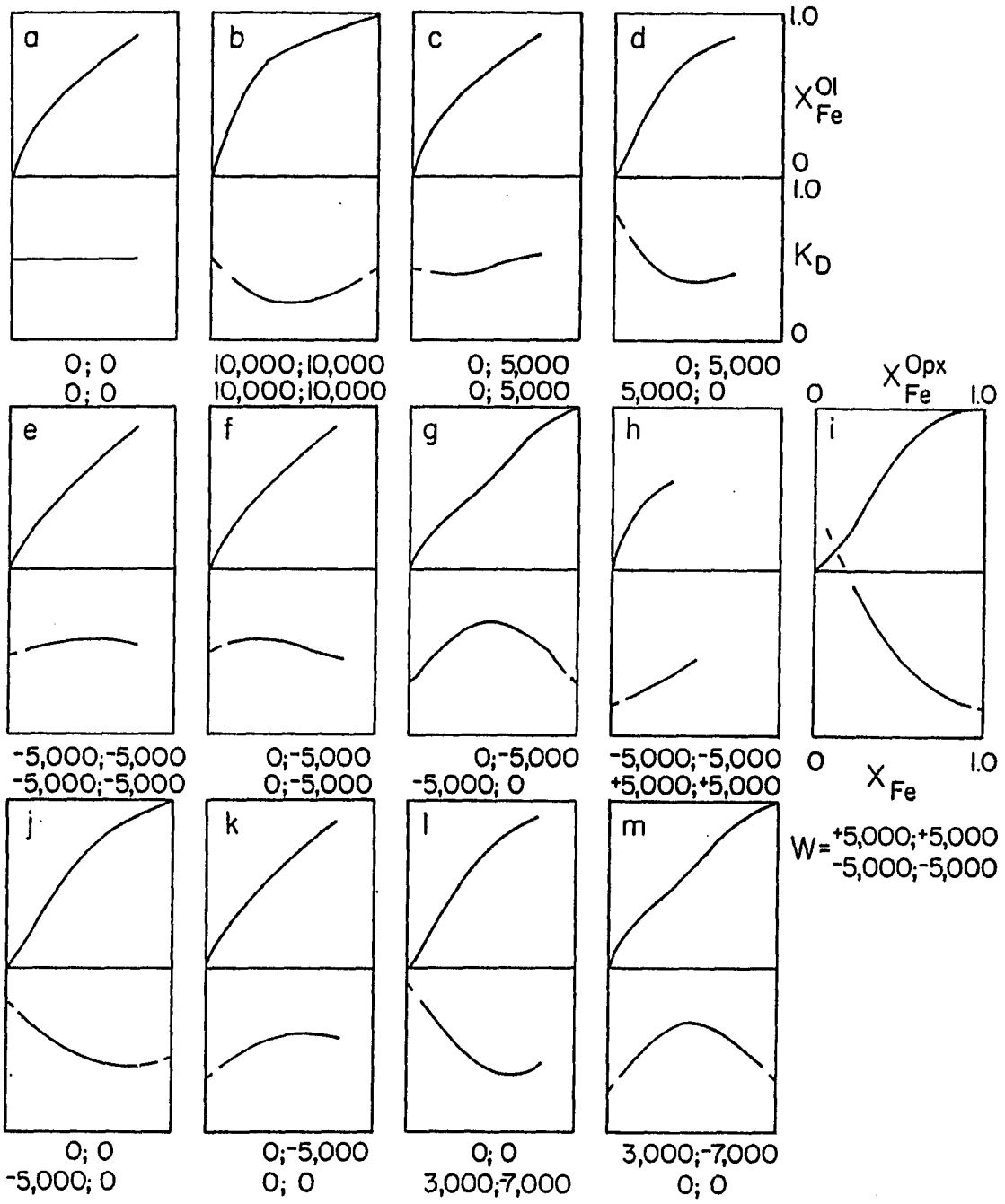

Figure 2.2 Effects of changing the simple mixture parameter W. The upper diagram for each case shows the mole fraction of Fe in orthopyroxene (X^{opx}), x-axis, against the mole fraction of Fe in olivine (X^{ol}), y-axis. The lower diagram shows K_D against X_{Fe} for the system. The numbers below each diagram are the W values used.

B. PYROXENE PHASE EQUILIBRIA

The method of Gibbs Free energy minimization has been used successfully here to model the pyroxene quadrilateral. The model produced in this thesis is entirely theoretical; no experiments were performed. Experimental work is both time consuming and expensive, and thus it is essential that a suitable theoretical model, which can predict the physical conditions for a wide variety of chemical compositions is developed. This model, once developed, can be used for compositions within the system where no experimental data are available. It can also be used to determine where future experimental work is necessary.

Since thermochemical data on most end-member components in the pyroxene quadrilateral are available, use of a suitable solution model permits us to completely characterize the system quantitatively. Compositions of coexisting pyroxenes are calculated using the method of total Gibbs Free Energy minimization as discussed earlier. The solution model we chose to apply to these data is from Kohler (1960) in which we use the binary interaction coefficients of the simple mixture (Guggenheim, 1952) model.

1. Available Data.

In order to compute a model to reproduce the phase diagram of the quadrilateral system we need the following data:

a. Enthalpy, entropy and heat capacity for all (four orthopyroxene and four clinopyroxene) end member components The components are numbered as enstatite (En) = 1, diopside (Di) = 2, ferrosilite (Fs) = 3 and hedenbergite (Hd) = 4.

b. Interaction coefficients (W_{ij}) for the binary solutions. There are

twelve binary solutions each for orthopyroxene and clinopyroxene (W_{12}, W_{21}, W_{13}, W_{31}, W_{14}, W_{41}, W_{23}, W_{32}, W_{24}, W_{42}, W_{34}, and W_{43}), shown on Figure 2.3.

c. Experimental data for coexisting pyroxenes over the total range of compositions and for a wide range of temperatures and pressures to test the derived model.

Thermochemical data are available at the temperatures and pressures of interest for orthoenstatite, orthoferrosilite, clinodiopside, and clinohedenbergite (see Figure 2.3). However, within the system we have four end members i.e. orthodiopside, orthohedenbergite, clinoenstatite, and clinoferrosilite that do not occur in nature at the temperature and pressure of interest. These end members are needed for the model. Clinoenstatite and orthodiopside have been estimated from the data of Lindsley et al., 1981. The remaining end members are, therefore, variables in the model.

Figure 2.4 shows very simply the free energy of such a binary system and why we need the fictive end member to completely model the solution. The figure shows that clinohedenbergite will always be the stable high Ca-phase, hence the possible thermochemical data on its fictive counterpart is limited by the binary solutions already known for the stable phase. These end members are, therefore, variables within the model.

The data on W_{12}, W_{21}, W_{34}, and W_{43}, for both pyroxenes, are available in Lindsley et al. (1981) and in Lindsley (1981) respectively or can be calculated from the solvus data. W_{13} and W_{31} (both pyroxenes), have been discussed amply in literature (Chatillon-Colinet et al.,

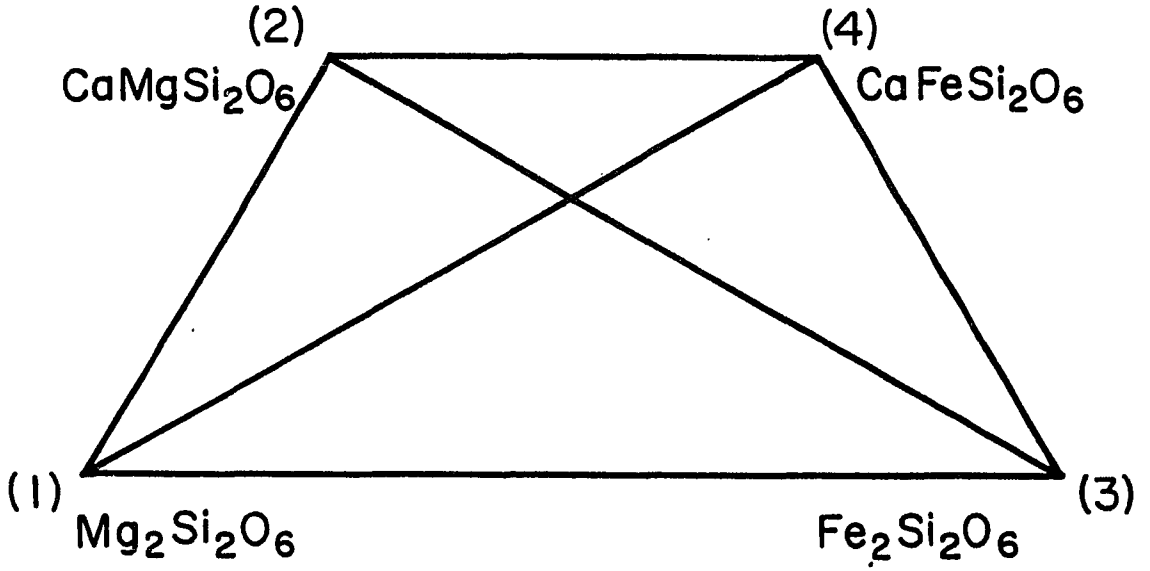

Figure 2.3. Diagram of the pyroxene quadrilateral indicating the compositions of the four endmembers and the binary solutions. End members are 1, enstatite; 2, diopside; 3, ferrosilite; and 4, hedenbergite. Thermochemical data for the endmembers are given in Table 2.2 and for the binary solutions in Table 2.3.

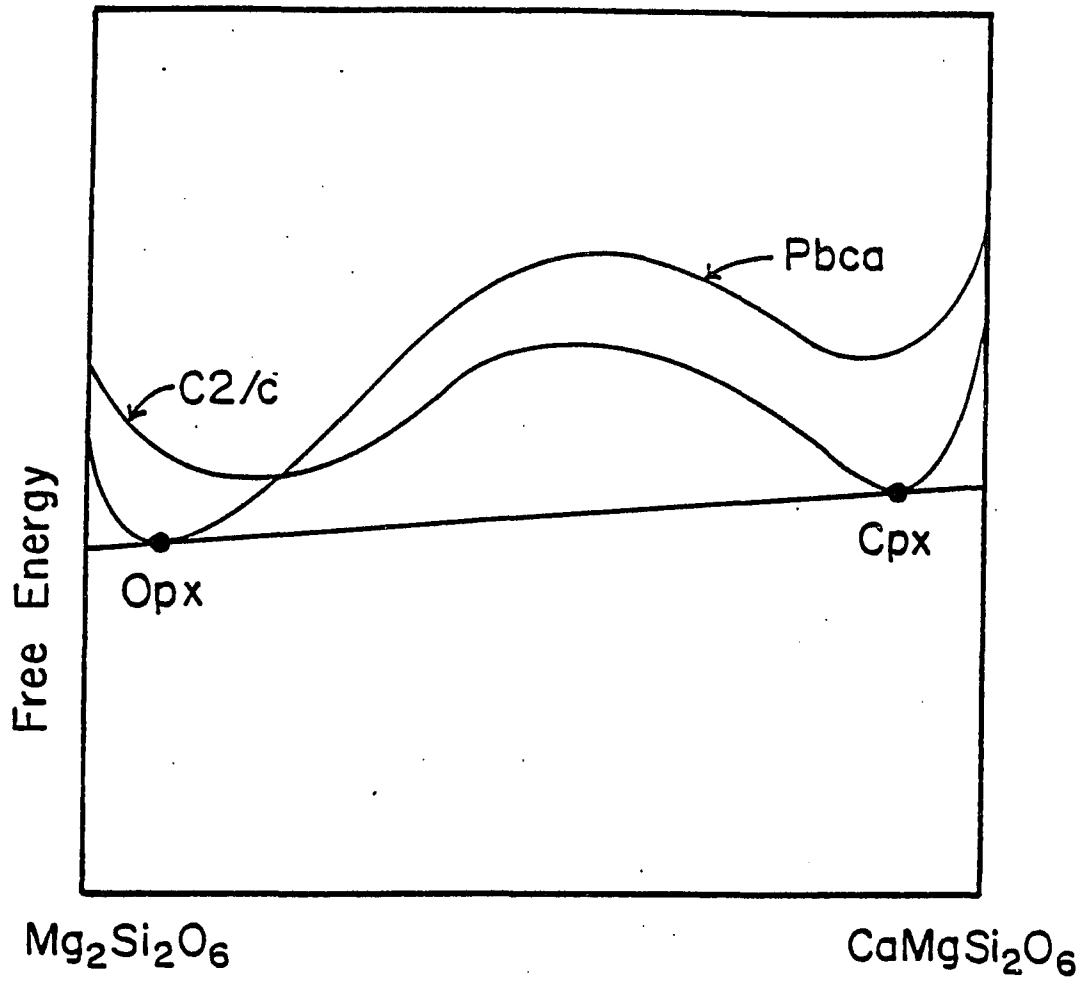

Figure 2.4. Gibbs Free Energy of the enstatite-diopside binary solution. The orthopyroxene structure, Pbca, is the stable phase (lowest Gibbs Free Energy) for the enstatite-rich composition (0-8 mol% diopside). The clinopyroxene structure, C2/c, is the stable phase for the diopside-rich composition (0-10 mol% enstatite). Between the two phases is a solvus where the Free Energy of a single phase can be lowered by the exsolution of two pyroxenes.

1983, Saxena, 1983a, and Sack, 1980), but are still considered variables in this model. The remaining six binary solutions for each pyroxene are also variables within the model. Values for these binaries are again restricted, i.e. whether exsolution will occur or not (see page 18).

The experimental data used to test the model are mainly from the work of Lindsley and coworkers. Lindsley (1983) presented a compilation of the experimental data (Lindsley, 1981; Lindsley & Dixon,1976; Lindsley et al, 1981; Lindsley et al., 1974; Turnock & Lindsley, 1981). Additional data from Davidson and Lindsley (1985), some previously unpublished, were also used. Because of a lack of data, pigeonite solid solutions have not been included in the present model.

2. Method of Calculation

Estimates of the possible thermochemical values for the fictive end members are made at the beginning of the modeling process. The remaining undefined binary solutions are arbitrarily set to ideality (W_{ij}=0). The calculations are performed using SOLGASMIX (initial composition and temperature and pressure of interest inputted) and the resulting (minimum Gibbs Free Energy) compositions for coexisting ortho- and clinopyroxene are noted. These compositions are then compared to the experimental data. The W_{ij} values and thermochemical data on orthohedenbergite and clinoferrosilite are adjusted, using an iteration procedure, until a close match between the calculated compositions and the experimentally determined compositions is found.

The W_{ij} should be considered as adjusted parameters necessary to reproduce the experimental data on compositions of coexisting pyroxenes

as closely as possible. The linear temperature dependance of W_{ij} is over a range temperatures at which the experimental data are available. Extrapolations to temperatures beyond these data may lead to unrealistic W_{ij} values.

Some of the work from previous studies has not been incorporated in this model. The experimental data of Fonarev and Graphchikov (1982) are rather high in Fe^{2+} for iron-rich samples. This cannot be reproduced by the present model. Chattillon-Colinet et al., (1983) and Sack (1980) both estimated a positive enthalpy of mixing for the W_{13} and W_{31} binaries. Use of such a non-ideal solution for this binary led to problems in reproducing the experimental data and, therefore, a positive enthalpy of mixing is not part of this model.

C. Results and Discussion

Tables 2.2 and 2.3 list the data on the end members and the W_{ij} parameters used and defined in this work. As stated previously, it must be emphasized that such results may be obtained by a somewhat different set of W_{ij} data and the set used here is not unique. These data are dependent on each other and should not be used in parts.

Figures 2.5-2.9 show a comparison of experimental (exp) and calculated (model) data on compositions of coexisting pyroxenes; the fit is very good. The results shown in this set of diagrams are all at 6 kbar, however, the model developed is equally valid over a wide range of temperatures (600-1000°C) and pressures (1-15 kbar).

Two problems are found with the model. The computed magnesium content of low magnesium orthopyroxenes is slightly lower than the experimentally determined value (Fig. 2.5.). This trend is also reflected in the high iron range in Figure 2.6. Secondly, the magnesium content of clinopyroxene is lower for the computed compositions in the low magnesium samples (Fig. 2.8), again reflected in the high-iron samples on Figure 2.9. These systematic differences in the two sets of data must be viewed as a failure of the adopted solution model and estimated W_{ij} parameters to represent the pyroxene compositions. (Any erratic difference is due to experimental and/or analytical errors.) Attempts to adjust the W_{ij} to improve this fit led to unacceptable changes at high temperatures.

In addition, with the data presented in Tables 2.2 and 2.3, we may calculate pyroxene compositions in the quadrilateral for any bulk compositions at specified pressure and temperature. Figure 2.10 shows calculated Fe^{2+}-Mg distribution in coexisting pyroxenes at 6kbar for a

Table 2.2 Thermochemical data on Pyroxenes*

Endmember Name	Composition	H°f (J/mol)	S° (J/mol.K)	a	bx10^2	cx10^{-7}	f
Orthoenstatite	$MgSiO_3$	-1546290	66.270	188.753	-0.53315	.4325 E-3	-1812.9
Clinoenstatite	$MgSiO_3$	-1544010	67.225	188.755	-0.53315	.4325 E-3	-1812.9
Diopside	$Ca_{.5}Mg_{.5}SiO_3$	-1600910	71.547	110.605	1.64	-.3293	0.0
Hedenbergite	$Ca_{.5}Fe_{.5}SiO_3$	-1419410	85.145	114.665	0.0171	-.3140	0.0
Ferrosilite	$FeSiO_3$	-1194510	94.560	133.000	0.00	-.4847	0.0
Clinoferrosilite	$FeSiO_3$	-1193590	95.398	133.000	0.00	-.4847	0.0
Orthodiopside	$Ca_{.5}Mg_{.5}SiO_3$	-1591040	71.540	110.605	1.64	-.3293	0.0
Orthohedenbergite	$Ca_{.5}Fe_{.5}SiO_3$	-1416780	84.879	114.665	0.0171	-.3140	0.0

*Source of data: Enstatite; S° and Cp from Haselton (1979) and H°f from Brousse et al (1984); Clinoenstatite and orthodiopside are estimated using data from Lindsley et al (1981) with Cp as in enstatite and diopside, respectively; Diopside, Robie et al (1078); Hedenbergite, adjusted within errors from Helgeson et al (1978); Ferrosilite; Bohlen and Boettcher (1982); Clinoferrosilite and orthohedenbergite were estimated using Lindsley (1981) data on phase equilibrium. H°f is the enthalpy of formation from the elements at standard state and S° is the entropy at standard state. The equation for the heat capacity is $Cp = a + bT + cT^{-2} + fT^{-½}$

Table 2.3 Pyroxene Solution Parameters (kJ/mol)

Orthopyroxene (En=1, Di=2, Fs=3, Hd=4)

$W_{12} = W_{21} = 25$
$W_{13} = 13.1 - 0.015T$
$W_{31} = 3.37 - 0.005T$
$W_{14} = 60.0$
$W_{41} = 30.0 - 0.00834T$
$W_{23} = 20.0$
$W_{32} = 16.0$
$W_{34} = W_{43} = 15$
$W_{24} = 5.0$
$W_{42} = 7.0$

Clinopyroxene

$W_{12} = 25.484 + 0.0812P$
$W_{21} = 31.216 - 0.0061P$
$W_{13} = W_{31} = 0$
$W_{14} = 93.3 - 0.045T$
$W_{41} = -20.0 + 0.028T$
$W_{23} = 24$
$W_{32} = 15$
$W_{24} = W_{42} = 12$
$W_{34} = 16.941 + 0.00592P$
$W_{43} = 20.697 - 0.00235P$

Data on W_{12}, W_{21}, W_{34} and W_{43} are from Lindsley et al (1981) and Lindsley (1981). All other W values were determined in this study.

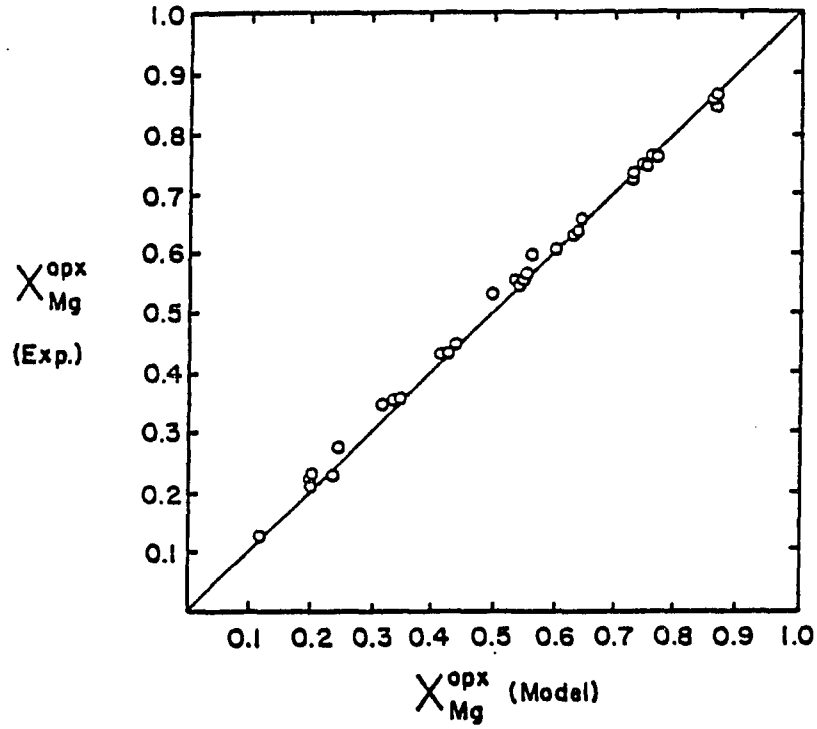

Figure 2.5. Comparison of experimental (exp) and calculated (model) data for the compositions of coexisting pyroxenes. Data are from Lindsley (1983), and Davidson and Lindsley (1985).

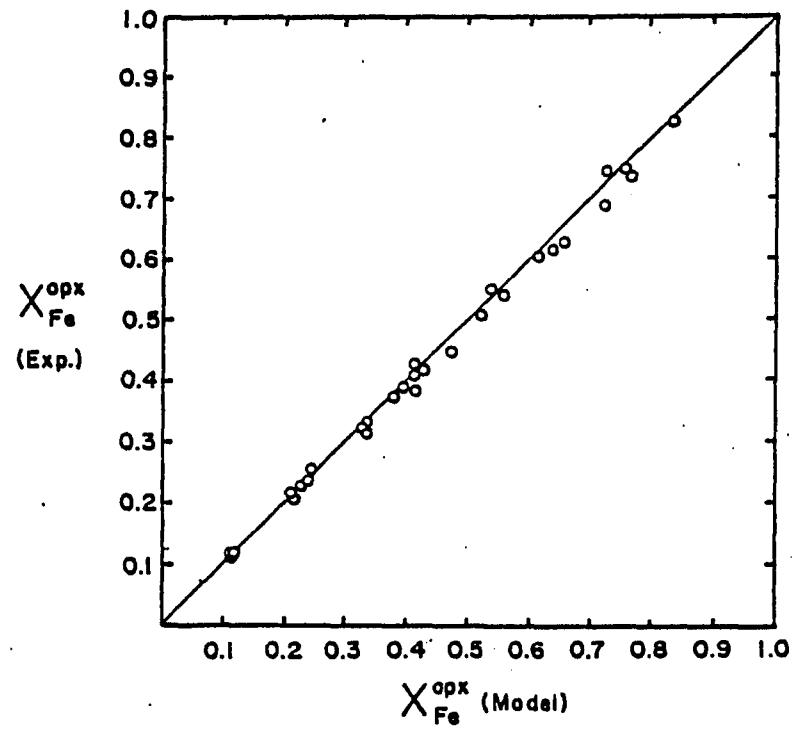

Figure 2.6. Caption as Figure 2.5

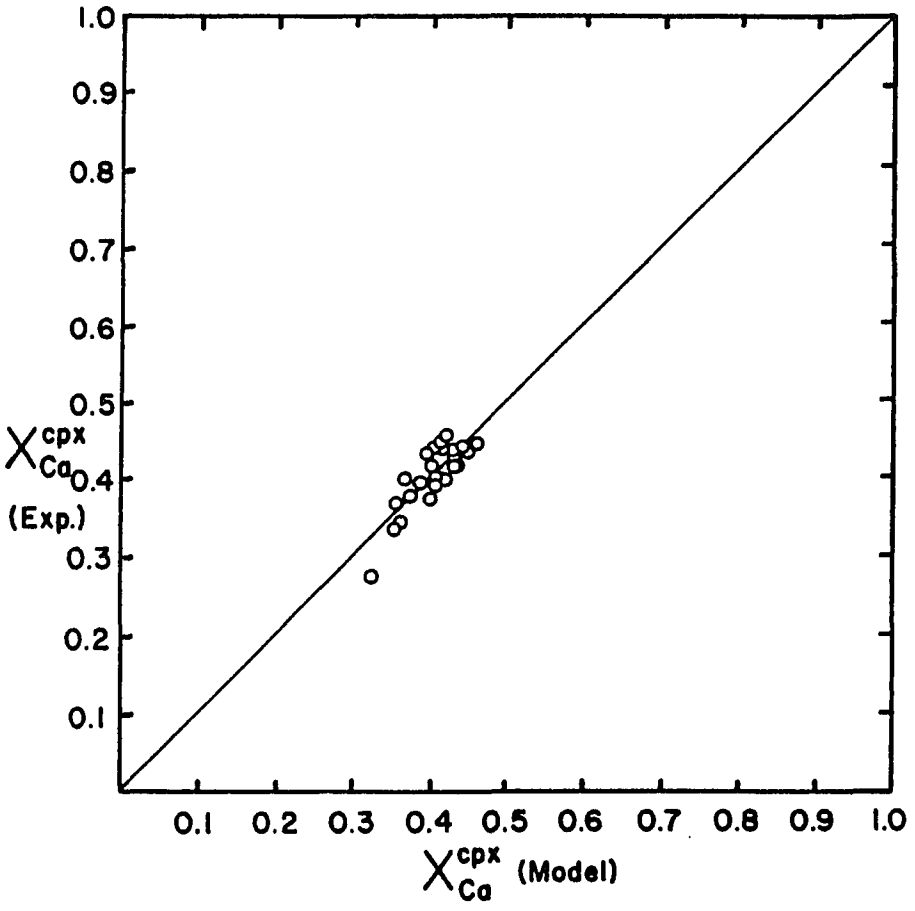

Figure 2.7. Caption as for Figure 2.5.

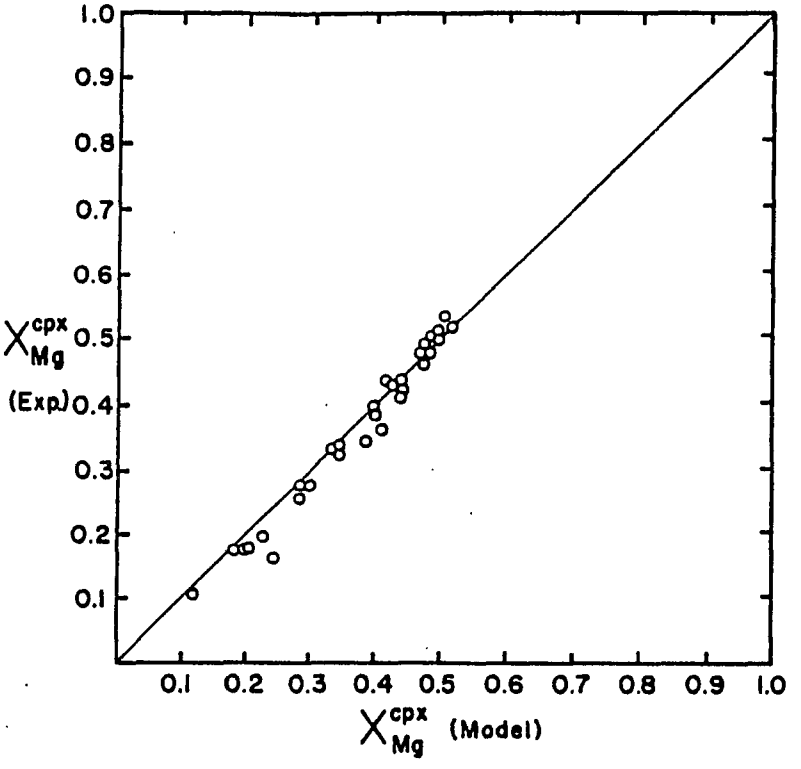

Figure 2.8. Caption as for Figure 2.5.

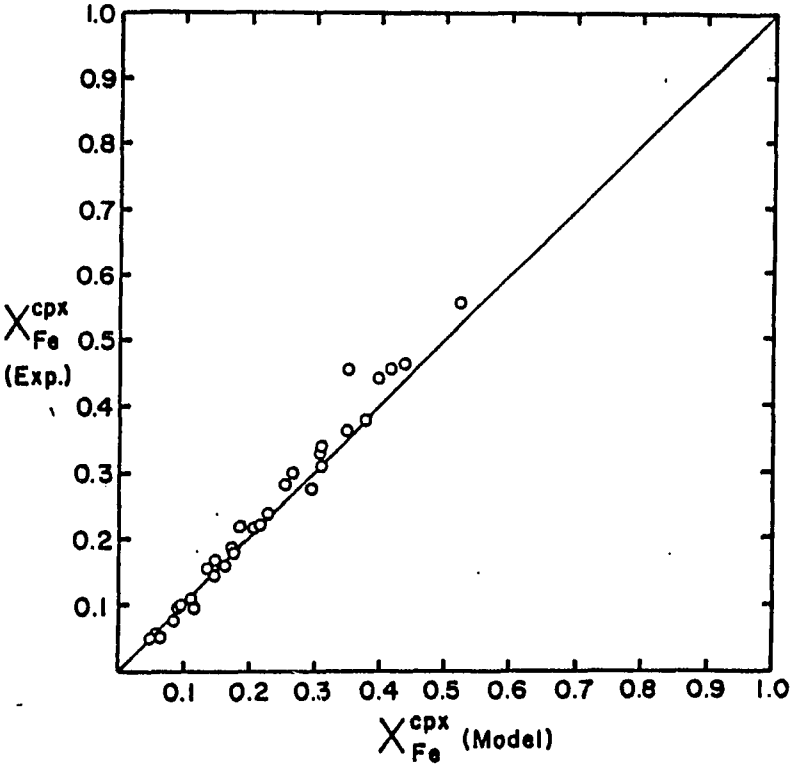

Figure 2.9. Caption as for Figure 2.5.

temperature range of 700-1400°C. In spite of the non-ideal solutions used in the thermodynamic model, the distribution curves for low (700-1000°C) temperatures, follow a trend that is very close to that expected for ideal solutions. This is due to the cancellation of the nonideal effects as considered by Kretz (1963) for distribution curves and demonstrated in Figure 2.2. At higher temperatures the cancellation effect does not occur and the distribution curves part from ideality and even cross at 1200-1400°C.

This effect is also shown in Figure 2.11, a plot of K_D against temperature. K_D is given by

$$K_D = (1-X_{Fe}/X_{Fe})^{Opx} * (X_{Fe}/(1-X_{Fe})^{Cpx}$$

where X_{Fe} is the binary mole fraction Fe/(Fe+Mg). If both pyroxenes were ideal binary solutions, K_D would only be a function of temperature and pressure and, therefore, on this plot of temperature against composition, K_D would plot as a vertical straight line. (The plot of K_D for an ideal solution can also be seen as Figure 2.2.a.) At low temperatures (700-900°C) on Figure 2.11, this is almost the case, again showing the cancellation of nonideal effects. However, at higher temperatures the K_D curves progressively become nonideal. The variation in K_D due to changing Fe/Mg ratio and the non-linear relationships are expressions of nonideal behaviour in the quadrilateral pyroxenes.

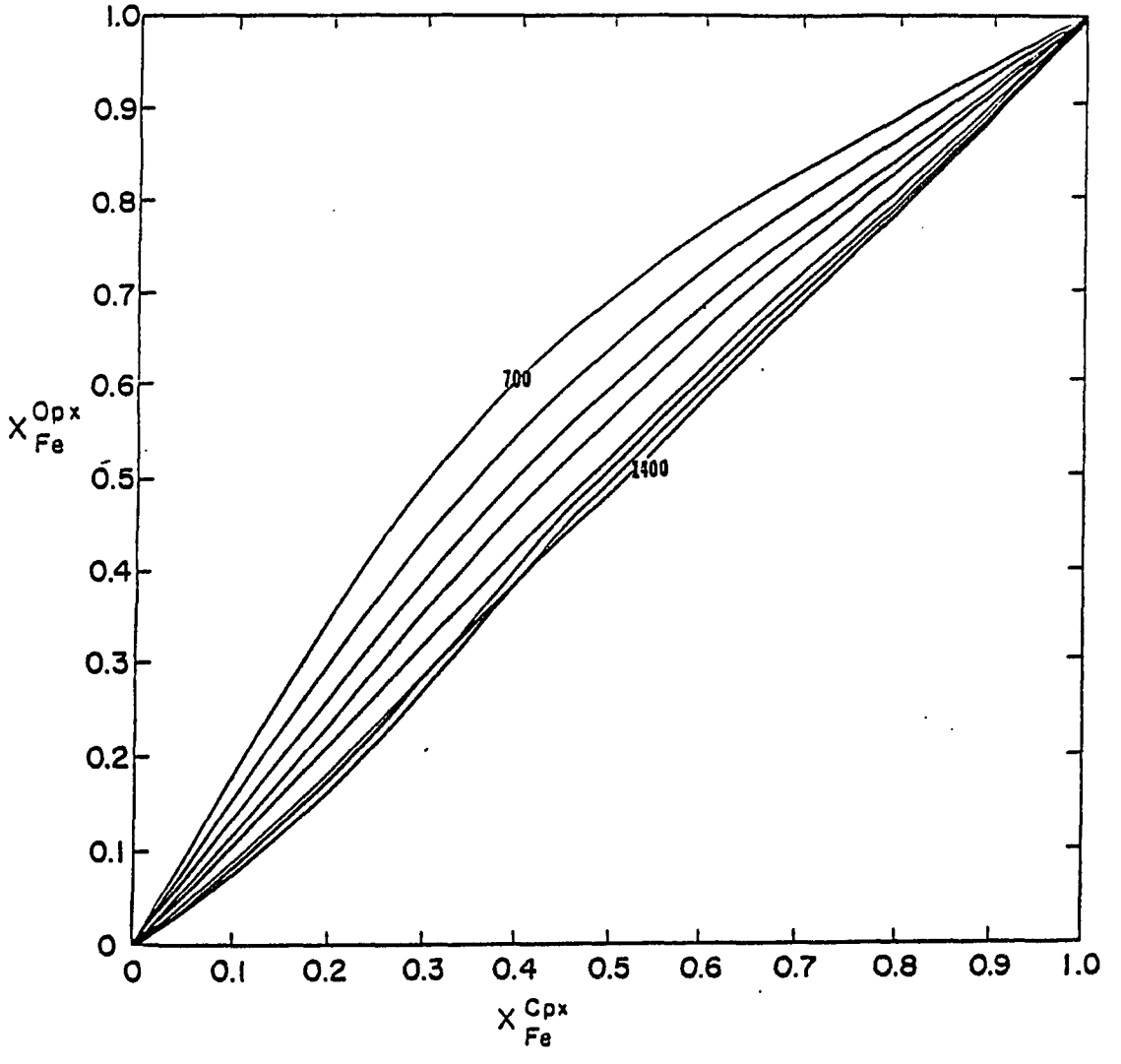

Figure 2.10. Calculated Fe^{2+}-Mg distribution between coexisting pyroxenes at 6 kbar and a temperature range of 700 1400°C. X_{Fe} is the binary mole fraction, Fe/(Fe+Mg) for each pyroxene. Ferrosilite is not stable at high temperatures (1300-1400°C).

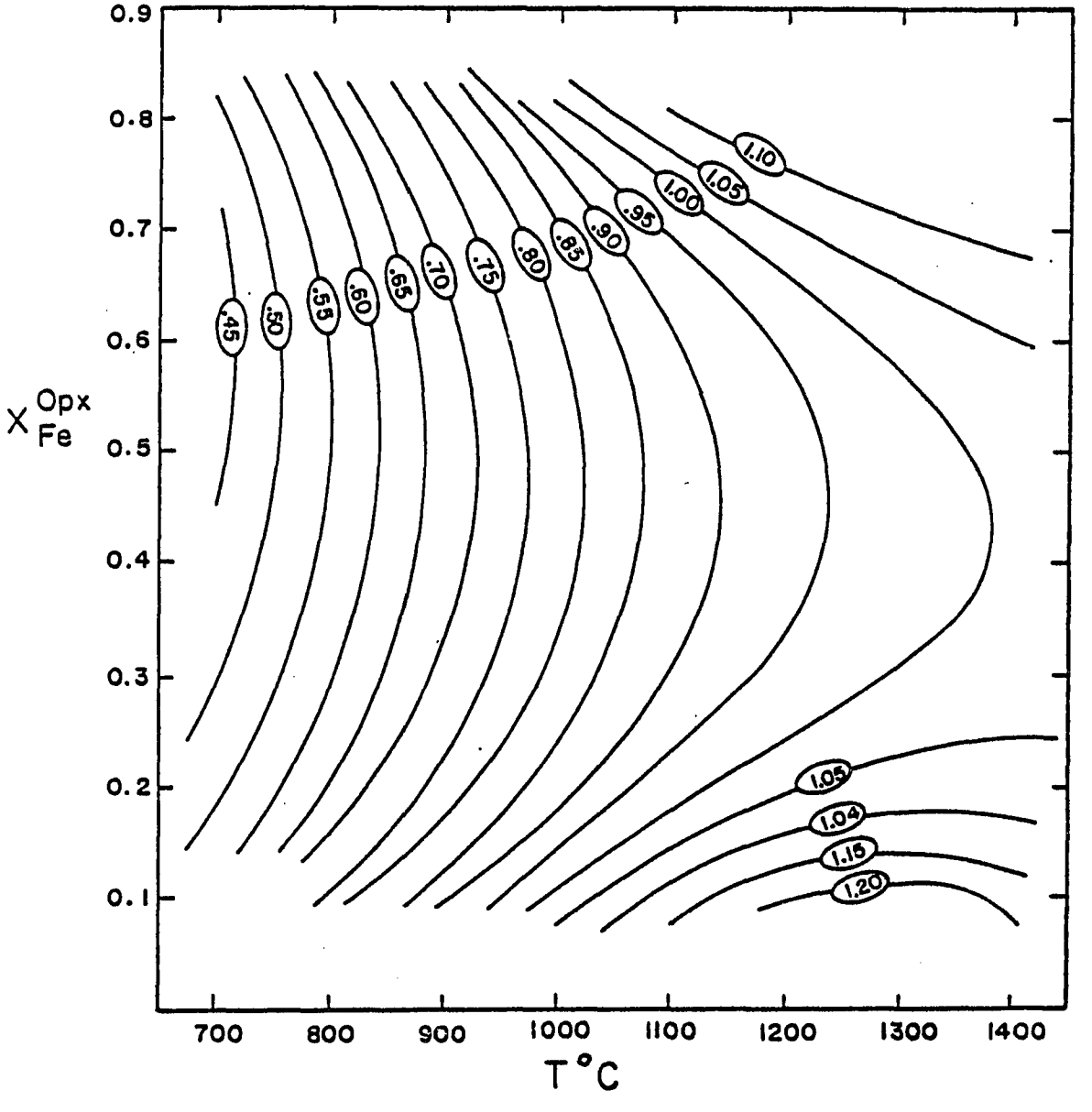

Figure 2.11. Plot showing the relationship of X_{Fe} in orthopyroxene with temperature and K_D. The pressure is 6 kbar. The relationships have only been shown for the compositions $0.10<X_{Fe}<0.80$, as the model calculations are not reliable outside this range.

D. APPLICATIONS

The thermodynamic model derived for the pyroxene quadrilateral is in good agreement with the experimental data over a wide range of composition, temperature and pressure. This justifies an attempt at using the model to create graphical geothermometers. These graphs have been designed to study the relative closure temperatures of the Ca-transfer reaction and the Fe^{2+}-Mg exchange reaction occuring in two-pyroxene bearing rocks. If the closure temperatures are different, this would indicate different rates for the two diffusion processes.

Differences in the closure temperatures for these two reactions, due to subsolidus processes, have been studied by two methods. Firstly, by detailed study of the changing compsitions of natural samples, and secondly, from a theoretical viewpoint.

If the Fe^{2+}-Mg exchange reaction is continuing to a lower temperature than the Ca-transfer reaction, this could possibly be seen in the changing compositions of finer and finer exsolution lamellae in the natural sample. Initially there would be movement of Ca, Fe^{2+}, and Mg between the two phases, followed by exchange of just Fe^{2+} and Mg with Ca-content constant. If this was plotted in the pyroxene quadrilateral we would see a rotation of the tie-lines (Figure 2.12) as the compositions of finer and finer exsolution lamellae were plotted. The Ca-rich phase would become increasingly Mg-rich, the Ca-poor phase more Fe^{2+}-rich.

Two electron microprobe studies on rocks from the Skaergaard intrusion appear to show this phenomenom. Nobugai et al. (1978), studied compositions of pyroxene hosts and lamellae from a ferrogabbro sample, in order to understand the subsolidus relations occurring. The

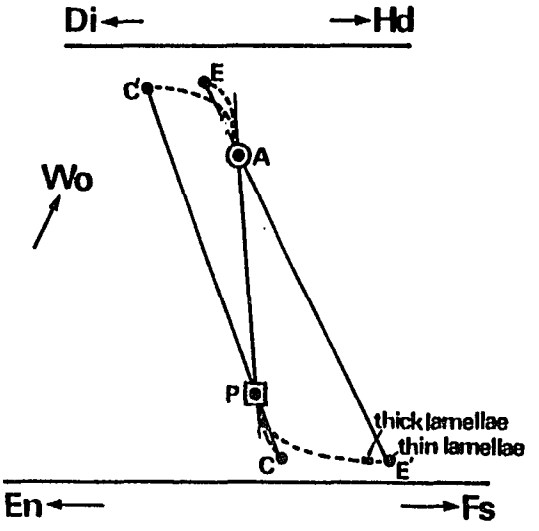

Figure 2.12. Schematic representation of the process of exsolution (shown as rotating tie-lines) within coexisting pyroxenes. Pigeonite (P)(also for low-Ca orthopyroxene), reacts to ahost (C) and lamellae (C'). Augite (A) reacts to a host (E) and lamellae (E'). From Nobugai et al. (1978).

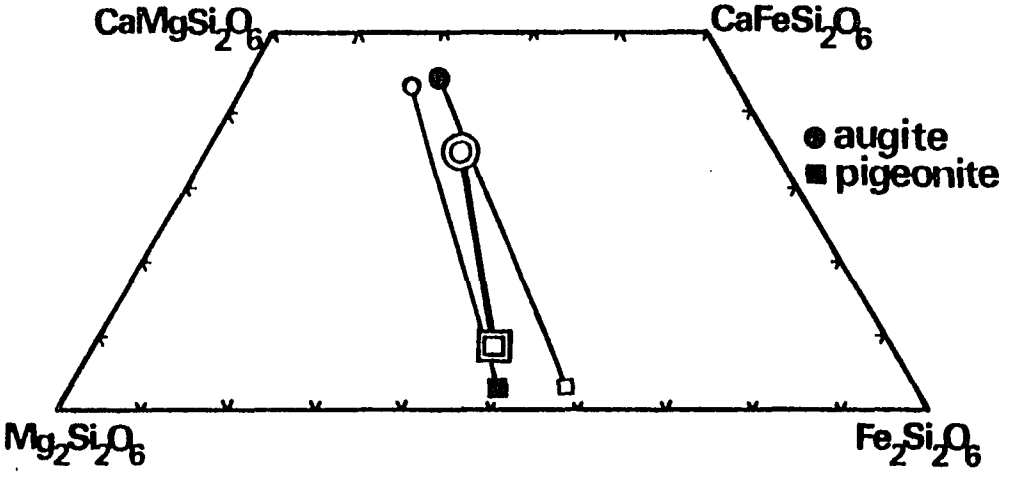

Figure 2.13 Actual chemical compositions for the two host-lamellae sets from the Skaergaard intrusion. The double circle is the bulk composition for augite, the double square is the bulk composition for pigeonite. From Nobugai et al. (1978).

compositions of the actual samples are indicated in Figure 2.13 and this has been interpreted in the schematic representation shown in Figure 2.12. Coleman (1978) also studied pyroxene hosts and lamellae from the Layered Series and found that the solidus and subsolidus tie-lines do not coincide. Again, Mg increased in the Ca-rich phase and decreased in the Ca-poor phase with cooling, resulting in a rotation of the tie-lines. A schematic diagram very similar to Figure 2.12 was used to indicate the probable trend. Although the actual compositions do change with the size of the lamellae, the diagrams showing the tie-line rotation are schematic.

Kretz (1982) studied the two different reactions theoretically and produced two geothermometers, based on equations, to indicate the possible differences in closure temperatures for the two reactions. Studies of samples from the Bushveld Complex resulted in different temperatures for the two reactions; an average temperature of 1020°C for the Ca-transfer reaction and of 980°C for the Fe^{2+}-Mg exchange reaction. Saxena, (1983a), also discussed the different closure temperatures of the two reactions. The temperature calculations were approached from a microscopic viewpoint i.e. the non-ideal ion interaction energies for the M1 and M2 sites in the crystal.

The possibility of different closure temperatures, therefore seems highly probable. The thermodynamic model developed here can easily be used to create two graphical geothermometers out of the same equilibrium composition data on coexisting pyroxenes. This theoretical model is based on a larger data set and more recent experiments than the earlier studies. The graphical geothermometers shown here are for 6 kbar, appropriate to granulite rocks. These are used for testing the model,

however, other graphs can be created for more detailed study of other geological areas with a different pressure regime.

Figure 2.11 (already discussed) shows the variation in K_D with XFe^{2+} in orthopyroxene and temperature at 6 kbar. This is drawn to indicate the changes in composition for the Fe^{2+}-Mg exchange reaction. Figure 2.14 shows temperature-compositional relations in clinopyroxene which coexists in equilibrium with orthopyroxene, indicating the Ca-transfer reaction. If coexisting pyroxenes represent complete frozen equilibrium, both figures should yield exactly the same temperature. If the two geothermometers yield significantly different temperatures we must consider that the two pyroxenes are not in complete chemical equilibrium with each other.

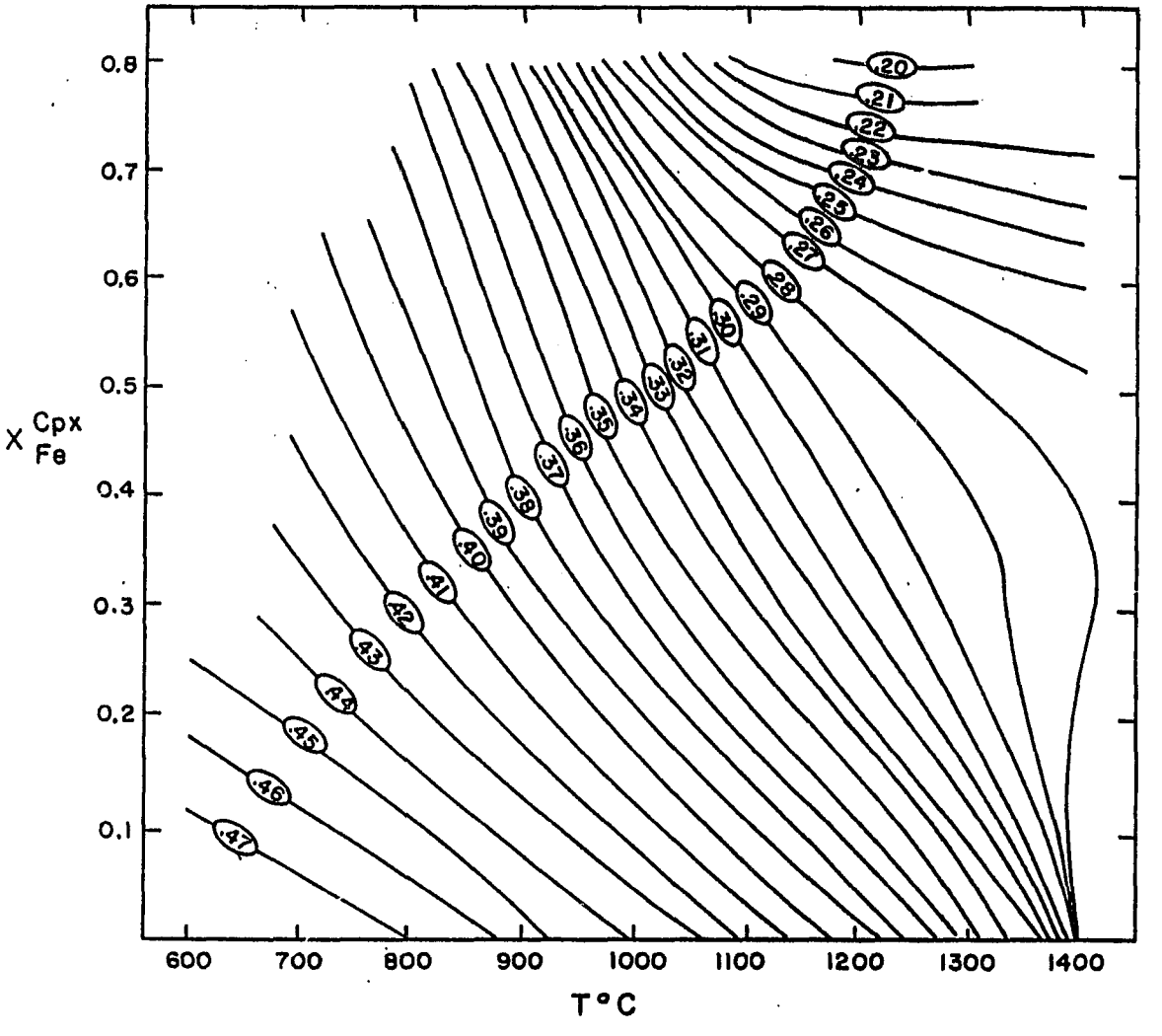

Figure 2.14. Plot showing the relationship of X_{Fe} in clinopyroxene with temperature and X_{Ca}. Pressure is 6 kbar. See text (p 48) for discussion of variation in X_{Ca}.

E. TESTING OF THE DERIVED PYROXENE GEOTHERMOMETERS

The best method of testing these two geothermometers is to ascertain the temperatures for several rock assemblages where equilibrium is believed to be attained and also where there are other, good controls on calculating the temperature. Firstly, however, there are several problems that need to be considered for these applications.

(1) The experimental data on which this study is based have some uncertainty (Lindsley, 1983, Turnock & Lindsley, 1981). A perfect match between the model and the experimental data has not been made for all compositions.

(2) Additional errors are introduced in estimated temperatures if K_D is used because it is not only a function of P, T and X_{Fe} but also of X_{Ca} in pyroxenes. Although in binary Ca-Mg pyroxenes, X_{Ca} is fixed at a given temperature, in quadrilateral pyroxenes a certain variation is possible in X_{Ca} and therefore in K_D.

(3) As stated earlier, calibration uses experimentally determined compositional data on equilibrated coexisting pyroxenes. Natural pyroxenes may not be in true equilibrium, therefore, the estimated temperatures do not strictly correspond to the temperatures of Fe-Mg exchange and Ca transfer reactions.

(4) The errors in temperature measurements from the two geothermometers are not evaluated in the absolute sense, but for relative temperatures, the errors would be those due to compositional measurements. To minimize the errors due to additional components such as Al^{3+}, Fe^{3+} and Mn, the method suggested by Lindsley and Anderson (1983) for calculating mole fractions should be followed.

Due to these difficulties an absolute geothermometer cannot really be proposed based on this work. This is true for all other geothermometers as problem (3) applies to most of the developed geothermometers and problem (4) to all of them.

1. Igneous Rocks

For quenched igneous rocks such as volcanics and some dikes, the temperatures calculated by the two geothermometers should be close to the actual quench temperature. There should be little difference between the temperatures obtained from either of the two graphical geothermometers. For plutonic rocks there is a broader range of possibilities, but, the temperature calculated for the Fe^{2+}-Mg exchange reaction (Fig 2.11) should be lower than that for the Ca-transfer reaction (Fig 2.14).

The rocks chosen for study are from four areas; dacite pumice from Mt. Shasta, California (Lawson et al., 1987); pyroxene andesite dikes and gabbros from the Klamath Mountains, California (Barnes, 1987); noritic rocks from the Stillwater complex, Montana (McCallum, 1968); gabbric rocks from the Bushveld Intrusion, South Africa (Atkins, 1969). All the temperatures have been estimated from figures 2.11 and 2.14 which are for a pressure of 6 kbar. This pressure value is incorrect for several of these samples. Pressure effects for these figures have been calculated and are found to be only a few degrees, therefore, the temperature estimates and relationships discussed are valid.

The dacite pumice with a fresh glass groundmass and a single pair of coexisting pyroxenes, is an ideal sample to test the derived

graphical geothermometers. The two geothermometers should yield the same quench temperature. The composition of the sample, ternary projection and temperatures obtained are indicated in Table 2.4. Both graphical geothermometers yield temperatures of approximately 935°C. This temperature agrees very well with the crystallization and cooling history proposed for this rock by Lawson et al. (1987).

Pyroxene andesite dikes from the roof zone of the Wooley Creek batholith are also shown in Table 2.4 (samples 704 and 584). Again, these samples should yield the same temperatures from both geothermometers. The porphyritic dikes were intruded into the wall rock of the batholith during intrusion. Barnes et al. (1986) showed that these dikes represent samples of the magma of the underlying Wooley Creek batholith and the lower level Slinkard Pluton. Due to rapid cooling and, therefore, lack of crystal accumulation, these dikes are likely to represent magmatic conditions. Temperatures obtained range from 920-1020°C.

Sample 584 again shows no difference in the temperatures obtained from either geothermometer, again indicating a rapid quench. The temperature of 1020°C is well within the range expected for crystallization of these dikes. Sample 704, however, yields slightly lower temperatures and the Ca-transfer reaction indicates the lowest temperature. This is opposite of the expected trend. With more detailed study, it is noted that the associated plagioclase minerals for sample 704 show both normal and reverse zoning, whereas, sample 584 shows no noticable zoning. Barnes (1987), indicates that the reverse and normal zoning are due to magma mixing and this process could explain the differences in temperatures obtained for this sample.

Gabbroic samples from the Wooley Creek Batholith have also been studied (samples 111 and 100) and are shown in Table 2.4. The samples show the expected lower temperature for the Fe^{2+}-Mg exchange reaction. This indicates that they have undergone further cooling and diffusion compared to the dike (sample 584) as the temperature decreased. These two samples will be discussed with the other plutonic samples.

The final sample shown in Table 2.4 is from the stratigraphically lower Slinkard Pluton. This is a sill-like body with an upper zone (including sample 645a) of foliated biotite-hornblende-quartz diorite. The temperatures are again lower than those obtained from the dikes, however, there is also a reversal of the expected trend between the two geothermometers. It is possible that there is some effect from the metamorphism but further speculation is not possible with the data available.

Tables 2.5 and 2.6 show the compositional data, ternary projections, distribution coefficients, and temperature estimates for the Stillwater Complex and Bushveld Intrusion respectively. In all cases, the temperatures estimated from the Fe^{2+}-Mg exchange reaction are significantly lower than the estimated temperatures involving Ca-transfer. This was also the case for the samples from the Wooley Creek batholith.

The samples from the Stillwater Complex yield a temperature of 1260-1140°C for the Ca-transfer reaction. The liquidus temperature for similar rocks from the Stillwater Complex has been calculated to be 1270°C (Raedeke,1982). The estimated temperatures for the Ca-transfer reaction are in good agreement with this temperature. The lower temperature range is 870-900°C. All the samples are in good Table 2.4

Table 2.4 Compositions, Distribution Coefficients of Volcanic Pyroxenes

	Mt. Shasta Dacite*		Klamath Mountain Intrusions#									
	3B685 Opx	3B685 Cpx	704 Opx	704 Cpx	584 Opx	584 Cpx	111 Opx	111 Cpx	100 Opx	100 Cpx	645a Opx	645a Cpx
SiO_2	53.61	52.94	53.64	52.04	53.97	52.30	50.97	51.83	54.54	52.41	51.49	51.09
TiO_2	0.24	0.32	0.22	0.47	0.23	0.48	0.25	0.58	0.17	0.29	0.07	0.25
Al_2O_3	1.36	1.89	0.88	1.70	0.94	1.95	1.15	1.98	2.12	2.42	1.21	2.26
MnO	0.47	0.23	0.54	0.31	0.48	0.30	0.58	0.30	0.22	0.15	0.58	0.30
FeO	18.58	8.20	20.12	9.97	18.87	9.61	25.01	10.97	13.75	6.71	26.40	12.02
MgO	25.00	14.79	23.52	14.94	24.94	15.08	20.43	14.25	27.95	15.66	18.84	12.81
CaO	1.13	20.44	1.44	20.23	1.49	18.94	1.50	20.05	1.70	20.75	1.44	20.84
Na_2O	0.06	0.41	0.02	0.34	0.04	0.31	0.06	0.36	0.09	0.32	0.03	0.38
Cr_2O_3	0.01	0.01	0.04	0.08	0.10	0.16	0.05	0.09	0.09	0.25	0.02	0.07
Total	100.46	99.23	100.35	100.07	101.05	99.12	99.98	100.43	99.96	98.96	100.11	100.11
Wo	2.3	39.9	2.9	39.8	2.9	36.9	3.0	38.9	3.4	39.5	3.0	40.7
En	69.0	45.9	65.6	43.8	68.1	46.4	57.5	42.7	75.3	48.8	54.3	38.9
Fs	28.8	14.3	31.5	16.4	28.9	16.6	39.5	18.4	21.3	11.7	42.7	20.5
$\frac{Fe}{Fe+Mg}$	.294	.238	.324	.272	.298	.263	.407	.301	.220	.193	.440	.345
K_D	.746		.780		.843		.627		.848		.670	
Fe^{2+}-Mg Exchange	940°C		980°C		1020°C		850°C		980°C		900°C	
Ca Transfer	930°C		920°C		1020°C		930°C		1010°C		810°C	

*Lawson et al (1987)
#Barnes (1987)

Table 2.5 Chemical Composition of Pyroxenes from the Stillwater Intrusion*

Wt% elem.	B25 Opx	B25 Cpx	B14 Opx	B14 Cpx	B2 Opx	B2 Cpx	B5 Opx	B5 Cpx	B10 Opx	B10 Cpx
Si	25.3	24.7	25.4	24.5	25.9	25.0	25.4	24.6	25.3	24.7
AL	0.46	0.96	0.59	1.10	0.58	1.13	0.50	1.05	0.51	0.98
Fe^{2+}	13.3	6.38	10.92	5.06	9.72	4.54	10.93	5.22	11.30	5.23
Fe^{3+}	0.70	1.04	0.61	0.99	0.55	0.97	0.61	1.00	0.62	1.00
Mg	14.8	9.84	16.4	10.3	16.8	10.5	16.7	10.6	16.0	10.2
Ca	1.34	13.1	1.28	13.6	1.02	13.2	1.61	13.4	1.30	13.5
Mn	0.31	0.19	0.25	0.15	0.22	0.14	0.24	0.15	0.26	0.15
Ni	0.03	0.02	0.04	0.03	0.05	0.04	0.06	0.04	0.05	0.03
Cr	0.02	0.03	0.04	0.08	0.14	0.24	0.12	0.23	0.05	0.09
Ti	0.14	0.21	0.12	0.21	0.13	0.17	0.13	0.21	0.13	0.27
Na		0.21		0.21		0.18		0.21		0.21
O	43.8	43.2	44.3	43.2	44.8	43.7	44.4	43.6	44.0	43.4
Total	100.2	99.9	99.8	99.3	99.9	99.8	100.2	100.4	99.5	99.8
Wo	3.8	35.1	3.6	36.3	2.8	34.3	03.0	35.3	3.6	36.3
En	68.4	50.6	74.7	52.5	77.6	55.3	75.4	53.3	73.7	52.0
Fs	27.8	14.3	21.7	11.3	19.6	10.4	21.6	11.4	22.6	11.7
$\frac{Fe}{Fe+Mg}$	.289	.220	.225	.177	.202	.158	.223	.176	.235	.184
K_D	.695		.741		.745		.747		.734	
Fe^{2+}-Mg Exchange	890°C		880°C		880°C		890°C		890°C	
Ca transfer	1140°C		1190°C		1260°C		1230°C		1190°C	

*From Table 9 of McCallum (1968)

Table 2.6 Chemical Compositions and Distribution Coefficients of Bushveld Pyroxenes (Atkins, 1969)

Sample	1 Opx	1 Cpx	3 Opx	3 Cpx	4 Opx	4 Cpx	6 Opx	6 Cpx
SiO_2	55.94	54.07	54.32	52.90	54.82	52.93	53.26	52.17
Al_2O_3	1.61	2.08	1.83	2.41	1.87	2.40	1.79	2.47
Fe_2O_3	0.97	0.56	1.28	1.03	1.22	1.07	1.35	1.10
FeO	7.15	2.53	13.44	5.10	11.49	4.61	15.25	6.15
MnO	0.19	0.09	0.29	0.16	0.28	0.15	0.36	0.20
MgO	32.12	17.39	27.56	16.18	28.71	16.55	26.30	16.04
CaO	1.48	22.12	1.18	21.46	1.44	21.55	1.10	21.14
Na_2O	0.01	0.41	0.07	0.36	0.09	0.35	0.09	0.27
TiO_2	0.11	0.21	0.25	0.37	0.21	0.26	0.20	0.29
Cr_2O_3	0.45	0.98	0.12	0.26	0.14	0.27	0.01	0.02
Total	100.18	100.58	100.35	100.25	100.29	100.17	99.73	99.88
Wo*	2.9	41.3	2.4	41.0	2.9	40.9	2.3	40.2
En	86.3	54.3	76.6	50.1	79.3	51.1	73.7	49.2
Fs	10.8	4.4	21.0	8.9	17.8	8.0	24.0	10.6
$\frac{Fe}{Fe+Mg}$	.111	.075	.215	.151	.183	.135	.246	.177
K_D	.648		.648		.697		.662	
Fe-Mg Exchange	720°C		810°C		820°C		830°C	
Ca Transfer	1050°C		980°C		1000°C		1000°C	

*Wo, En, Fs determined by projection of Lindsley and Anderson (1983)

agreement. Raedeke (1982) estimates the lower limit for subsolidus reactions on a macro-crystal scale to be approximately 950°C. The temperatures indicated by the Fe^{2+}-Mg exchange reaction are lower than this. Howevere, the exchange reaction is expected to occur over a smaller diffusion area and, therefore, a lower temperature would be expected.

The temperatures for the Bushveld Intrusion are lower for both reactions but the expected trend with the Ca-transfer reaction giving the higher temperature is again noted (Table 2.6). The samples are from three different units in the Bushveld Intrusion. Sample 1 is from the lowest unit, the Basal Series; samples 3 and 4 are from the Critical Series; sample 6 is from the overlying Main Zone. The higher temperatures are very similar with a range of 1040-980°C, the lower temperatures are also very similar (810-870°C) except for sample 1 with a temperature of 730°C. This may be due to the long slow cooling of the Basal Series.

The two geothermometers developed here indicate a much wider temperature interval for these Bushveld samples than those developed by Kretz (1982). The two differing reactions from Kretz (1982) yield average temperatures of 1020°C for the solvus equation (Ca-transfer) and 980°C for the exchange reaction. The higher temperatures are in good agreement. Our model gives a much lower temperature for the closure temperature of the Fe^{2+}-Mg exchange reaction. This would be expected from a slowly cooled plutonic rock and is in agreement with estimates of subsolidus reactions (Raedeke, 1982).

From the study of these four areas of igneous rocks, it appears that the theory of faster rates of reaction for the Fe^{2+}Mg exchange as

compared to the Ca-transfer reaction is substantiated. The geothermometers developed also tested well for samples from volcanic rocks and dikes, yielding the expected similar temperatures. The geothermometers can now be used to interpret the more complex relations of metamorphic rocks

2. Metamorphic Rocks

For metamorphic rock the cooling history is further complicated. In these rocks we are following a complex P-T-time path with changing textures and mineralogy. As the kinetics of the reactions are faster at higher temperature, and as the retrograde reactions are often subordinate due to the loss of fluids during the prograde stage, the temperature calculated is often near that of the maximum temperature attained. However, this can be extremely complex as the mineral-texture relationships and the effects of prior or later metamorphic events, and the original state of the unmetamorphosed rock are also important. In studying metamorphic rocks it is extremely important to ascertain whether equilibrium has been reached and to be wary of zoning. This is true even in rock showing no evidence of retrograde reactions. One must also be aware of re-equilibration during cooling. (see also Powell, 1985). It is probably easier to study an area of contact metamorphism (temperature decreasing away from the contact) first and then study the more complex relationships in regionally metamorphosed areas

a) Contact Metamorphism

Studies on the Kiglapait Aureole by Berg and Docka (1983) and Docka et al. (1985) have determined a well developed thermal profile. Their data have then been used for a study on comparative geothermometry, not only for the pyroxenes but also for clinopyroxene-ilmenite, orthopyroxene-ilmenite, olivine-ilmenite, olivine-orthopyroxene and Fe-Ti oxide geothermometers.

The ternary projections, mole fractions and distribution coefficients for these samples are in Table 2.7. A comparison of the derived temperatures from these and other two-pyroxene geothermometers is shown in Table 2.8. The general trend, as expected, for all of the geothermometers is for the temperature to decrease with increasing distance from the contact. In addition, the temperatures obtained from the two different geothermometers from this study, follow the established pattern with the Ca-transfer reaction yielding slightly higher temperatures overall than the Fe^{2+}-Mg exchange based geothermometer. This again suggests the Fe^{2+}-Mg ion-exchange continues to a lower temperature.

Several samples are clearly problematic for the Fe^{2+}-Mg exchange based geothermometer derived in this study, these are 74-18a, SN154, K13831, and 74-96 (*, Table 2.8). The first three samples all yield temperatures higher than would be expected for the Fe^{2+}-Mg exchange reaction; the Ca-transfer reaction does not appear to be affected. The Fe/(Fe+Mg) ratios for the orthopyroxene show that these three samples are the richest in iron (Fe/(Fe+Mg)>0.585). As pointed out in the previous section the match of the experimental data to the model for the iron-rich samples was a problematic area. The fourth sample has one of

Table 2.7 Compositions and Distribution Coefficients for Pyroxenes from the Kiglapait Contact Aureole (Docka et al., 1986)

Sample	Dist. (m)	Orthopyroxene Wo	En	Fs	Fe/Fe+Mg	Clinopyroxene Wo	En	Fs	Fe/Fe+Mg	K_D
K13849	7	3.6	48.2	48.2	0.501	36.7	37.1	26.2	0.414	0.705
K13850	15	2.7	56.8	40.5	0.416	38.1	43.3	18.7	0.302	0.606
74-75a	130	2.2	55.5	42.3	0.433	39.4	40.2	20.4	0.337	0.666
K13845	215	3.3	42.6	54.1	0.559	39.0	34.5	26.5	0.434	0.605
K13843	255	1.8	54.0	44.2	0.450	41.6	39.0	19.4	0.332	0.608
K13842	280	2.6	45.7	51.6	0.530	39.7	36.2	24.1	0.400	0.590
74-18a	300	3.4	24.4	72.2	0.747*	36.5	18.3	45.2	0.712	0.835
K13840	390	2.1	56.3	41.6	0.425	40.7	42.3	17.0	0.287	0.544
74-15j	410	1.7	65.6	32.7	0.333	41.8	46.1	12.1	0.208	0.527
K13839	445	2.3	48.9	48.8	0.499	40.2	36.5	23.3	0.390	0.640
74-96	510	1.2	79.0	19.8	0.200*	44.7	48.2	7.1	0.128	0.588
K13835	535	2.5	44.9	52.5	0.539	39.9	35.0	25.1	0.418	0.613
K13834	535	2.4	46.4	51.2	0.525	39.2	36.5	24.3	0.400	0.603
K13833	570	2.5	47.8	49.7	0.510	40.4	37.5	22.1	0.371	0.567
75-7x	605	2.3	48.2	49.5	0.507	39.9	37.8	22.2	0.370	0.572
74-134d	700	1.1	82.6	16.3	0.165	44.6	49.5	5.8	0.105	0.593
74-21	725	1.2	80.8	18.0	0.182	44.6	50.4	5.0	0.090	0.445
D80-60	835	1.6	67.6	30.8	0.313	43.2	46.3	10.5	0.185	0.498
K13831	850	2.4	40.5	57.2	0.585*	40.7	33.0	26.3	0.444	0.564
D80-152	1020	1.5	67.6	30.9	0.314	44.3	45.8	9.9	0.178	0.473
D80-164	1020	1.4	61.7	36.7	0.373	44.2	43.9	11.8	0.212	0.452
D80-169	1160	1.5	62.5	37.0	0.372	44.1	44.0	11.9	0.213	0.457
SN154	1920	2.3	36.4	61.2	0.627*	42.3	30.5	27.2	0.471	0.530

Table 2.8 Comparison of Cation Exchange Temperatures, Kiglapait Aureole

Sample	Dist. (m)	Est[1] T°C	Fe-Mg[2] Exchange	Ca[2] Transfer	Coexisting Pyroxenes Cpx[3]	Opx[3]	Cpx[4]	Cpx[3]
K13849	7	947°C	920°C	970°C	980°C	960°C	960°C	830°C
K13850	15	942	830	980	960	910	940	750
74-75a	130	885	890	890	893	790	950	780
K13845	215	842	850	850	857	835	910	730
K13843	255	818	840	800	810	833	825	600
K13842	280	810	830	850	855	783	885	690
74-18a	300	800	940*	820	835	785	830	690
K13840	390	765	780	850	835	758	880	680
74-15j	410	755	770	870	882	757	815	600
K13839	445	740	870	830	828	758	875	680
74-96	510	720	780*	820	790	780	880	720
K13835	535	712	850	830	818	768	870	680
K13834	535	712	840	860	860	758	880	680
K13833	570	708	810	840	810	758	880	650
75-7x	605	700	820	850	868	728	850	650
74-134d	700	675	770	840	815	785	760	580
74-21	725	668	700	860	825	757	660	520
D80-60	835	650	720	830	825	725	750	580
K13831	850	642	810*	780	768	719	820	620
D80-152	1020	615	690	770	725	715	700	510
D80-164	1020	615	690	730	715	690	700	500
D80-169	1160	600	710	730	730	700	730	530
SN154	1920	560	770*	670	670	683	730	560

[1]Berg and Docka (1983). [2]This Study. [3]Lindsley (1983), Lindsley and Anderson (1983). [4]Ross and Huebner (1975)

the lowest Fe/(Fe+Mg) values for orthopyroxene. In addition, this sample also gave irregular temperatures for two of the other geothermometers tested by Docka et al. (1985). It is suggested therefore, that this may be a problem with this particular sample.

Ignoring these four samples, a plot has been of the change in temperature with distance from the contact (Figure 2.15). Onto this the thermal profile suggested by Berg and Docka (1983) has been drawn. The temperatures obtained follow the thermal profile quite well for the higher temperatures but, at lower temperatures, the trend is higher than the thermal profile. This is the same for all the two pyroxene geothermometers (Table 2.8) and indicates that at lower temperatures the diffusion rates for the two reactions do not keep up with the cooling rate of the whole rock. Similar relationships, with the theoretical thermal profile indicating lower temperatures than calculated from geothermometers, have been noted in the Appalachian areas (personel communication, A. Ludman, 1988). In addition, none of these pyroxene geothermometers were calibrated below 700°C.

For defining temperatures in contact metamorphic rocks, the geothermometers designed in this study are as viable as the other two-pyroxene geothermometers. In addition, the Fe^{2+}-Mg geothermometer from this study does indicate a slightly lower temperature for the more distant samples than the other pyroxene geothermometers.

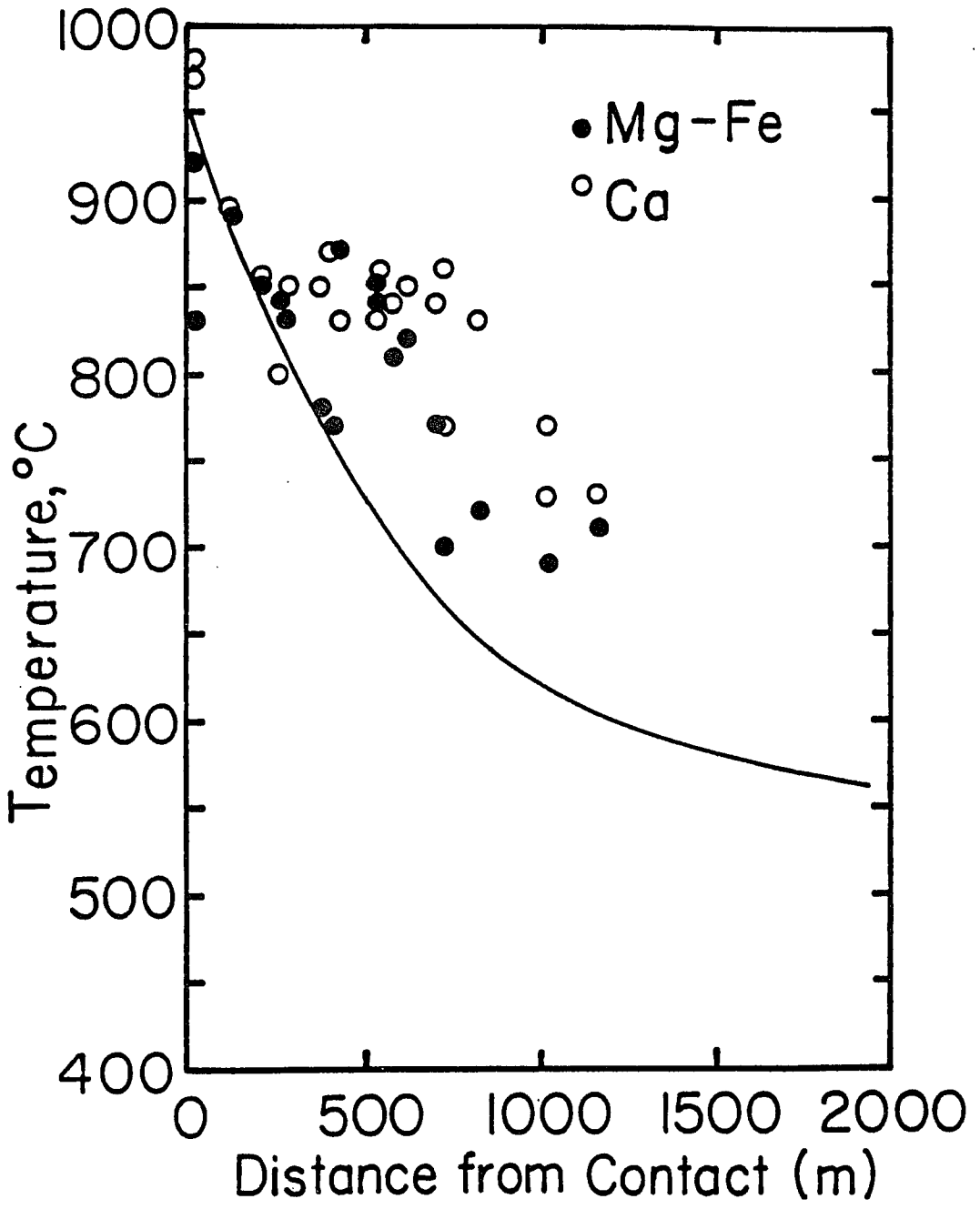

Figure 2.15 Pyroxene equilibrium temperature calculated by model as a function of distance from the contact aureole of the Kiglapait Intrusion. Temperatures from the Fe^{2+}-Mg exchange reaction are indicated as filled circles and temperatures from the Ca transfer reaction are indicated by open circles. There is a general tendency for the temperatures indicated by the Ca transfer reaction to be higher than those indicated by Fe^{2+}-Mg exchange.

b) Regional Metamorphism.

Three areas have been chosen for the study of regional metamorphic rocks. These are granulites, Cape-Riche, Australia (Stephenson, 1984); charnockites, Finland (Saxena, 1969); granulites, Sweden (Saxena, 1968). These rocks have all undergone complex metamorphic histories and, therefore, the simple associations found in both the igneous and contact metamorphic samples are not expected. In addition, the three regions chosen are quite diverse and will probably give three different relationships of the temperatures from the two geothermometers.

Stephenson, 1984, studied a series of coexisting pyroxene samples from a low-pressure, granulite-facies terrain at Cape-Riche in the Precambrian Albany-Fraser Province of Western Australia. The pyroxenes used are chemically homogeneous within the individual grains, suggesting a long period of equilibrium and all are relatively low in other, non-quadrilateral, components. The samples are from a restricted area and believed to be isothermal. Stephenson (1984) uses the samples to assess many of the different pyroxene geothermometers and to formulate a thermal history of the area. Stephenson (1984) also estimates the major episode of the metamorphism by independent methods, based on mafic assemblages and garnet-biotite thermometry, and suggests a temperature range of 700-800°C.

Compositional data for all the coexisting pairs of pyroxenes studied by Stephenson (1984) are shown in Table 2.9. Many of these samples, however, do not project on the ternary diagram according to the method of Lindsley and Anderson (1983) as the amounts of non-quadrilateral components are too great. Therefore, they are not suitable for use with the geothermometers derived in this study. The

ternary projections for the remaining samples are indicated in Table 2.10 along with the temperatures obtained from both graphical geothermometers. The range of temperatures is 730-850°C, well within the range for granulitic rocks. This is also in good agreement with the estimate of Stephenson (1984). Also of interest in this case is the fact that there are no real differences between the two geothermometers derived in this study. This indicates that, for this case of regional metamorphism, other factors may influence the kinetics of the two reactions.

The range of temperatures derived for these samples is compared to other geothermometers in Table 2.11 (from Stephenson,1984). Stephenson (1984) suggests that the Wells (1977), Powell (1978), Wood and Banno (1973), and Fonarev and Graphchikov (1982) are all too high with a average temperature of 900-820°C. In addition, Lindsley (1983) for the orthopyroxene version is probably too low at 680°C, but this graphical geothermometer is very difficult to interpret. The geothermometers developed here are well within the range and compare favorably with those of Kretz (1982; both methods), Lindsley (1983; cpx). and Ross and Huebner (1975).

Table 2.9 Compositions of Pyroxenes in Granulites from Cape Riche, Western Australia (Stephenson, 1984)

	Homogeneous Grains (Opx)										Exsolved Domains (Opx)				
	288	290	293	298	300	301	302	303	306	308	288	290	298	301	303
SiO_2	50.01	51.28	49.54	50.15	50.72	51.33	51.11	51.89	51.49	51.32	49.87	51.43	50.39	51.21	51.65
TiO_2	0.12	0.10	0.14	0.13	0.09	0.10	0.10	0.09	0.09	0.14	0.17	0.08	0.20	0.10	0.11
Al_2O_3	1.07	1.16	0.99	1.08	1.40	1.03	1.19	1.25	1.33	1.35	1.16	1.00	1.10	1.14	1.39
Fe_2O_3	1.44	1.25	0.81	1.43	1.60	1.41	1.66	1.64	1.42	1.70	1.48	1.21	0.91	1.59	1.84
FeO	30.09	25.88	33.44	29.72	26.49	25.24	25.26	22.81	24.40	24.06	29.91	25.86	29.43	24.62	22.53
MnO	1.05	0.87	0.93	0.76	1.18	1.23	1.24	1.00	0.88	0.99	0.96	0.87	0.77	1.22	0.98
MgO	15.62	18.98	13.43	16.13	18.03	19.10	19.07	21.06	19.92	19.98	15.34	19.05	16.18	19.22	20.95
CaO	0.79	0.67	0.83	0.79	0.72	0.75	0.63	0.61	0.67	0.65	1.27	0.71	1.10	1.13	0.79
Total	100.18	100.19	100.11	100.19	100.23	100.19	100.27	100.34	100.20	100.19	100.16	100.21	100.08	100.23	100.23

	Homogeneous Grains (Cpx)										Exsolved Domains (Cpx)				
SiO_2	51.10	51.91	50.61	51.04	51.16	51.65	51.55	51.66	51.82	51.56	50.75	51.78	50.81	51.02	51.06
TiO_2	0.12	0.13	0.15	0.15	0.20	0.14	0.17	0.18	0.15	0.17	0.18	0.05	0.14	0.19	0.25
Al_2O_3	1.81	1.76	1.80	1.81	2.18	1.92	2.04	2.29	2.22	2.24	2.14	1.83	2.25	2.63	2.52
Fe_2O_3	1.58	1.42	1.56	2.08	2.04	1.99	2.01	2.15	1.41	1.92	1.72	1.73	2.36	2.63	2.52
FeO	12.15	9.39	14.31	11.82	9.73	9.46	9.05	8.03	8.69	8.66	12.88	9.53	12.05	9.56	9.16
MnO	0.44	0.37	0.40	0.32	0.44	0.52	0.53	0.39	0.32	0.38	0.44	0.37	0.32	0.55	0.46
MgO	11.49	13.26	10.15	11.71	12.54	12.87	12.90	13.54	13.40	13.25	11.44	13.29	11.68	12.72	13.25
CaO	21.18	21.61	20.84	20.78	21.48	21.14	21.46	21.43	21.79	21.55	20.22	21.30	20.03	20.57	20.24
Na_2O	0.33	0.34	0.36	0.47	0.43	0.55	0.52	0.57	0.38	0.47	0.39	0.36	0.61	0.63	0.64
Total	100.20	100.19	100.18	100.18	100.20	100.24	100.23	100.24	100.18	100.20	100.16	100.24	100.25	100.28	100.27

Table 2.10 Composition of Regional Metamorphic Pyroxenes from Stephenson (1984)

Sample	288	288ex	290	290ex	293	298	306
Orthopyroxene							
Wo*	1.8	2.4	1.4	1.5	1.8	1.7	1.4
En	47.2	48.3	55.9	55.9	40.9	48.3	58.4
Fs	51.0	49.3	42.7	42.6	57.2	50.0	40.2
Fe/Fe+Mg	.519	.505	.433	.432	.583	.509	.408
Clinopyroxene							
Wo	41.9	40.0	42.5	41.5	41.8	41.6	42.2
En	36.5	36.8	41.1	41.7	32.5	37.3	42.2
Fs	21.6	23.2	16.3	16.8	25.7	21.1	15.4
Fe/Fe+Mg	.372	.387	.284	.287	.442	.361	.267
KD	.548	.576	.519	.529	.565	.546	.530
Fe^{2+}-Mg Exchange	780°C	830°C	750°C	760°C	790°C	800°C	780°C
Ca Transfer	750°C	850°C	780°C	830°C	730°C	770°C	810°C

*Wo, En, Fs determined by the projection method of Lindsley and Anderson (1983).

TABLE 2.11 Temperatures in °C derived from several two-pyroxene geothermometers from pyroxene pairs in granulites, Cape Riche, Western Australia, after Stephenson, 1984.

Field number		288	290	293	298	300	301	302	303	306	308	Range
Wood and Banno	a*	833	860	816	846	844	855	846	870	860	861	816-870
(1973)	b*	863	872		864		874		904			863-904
Ross and Huebner	a*	700	750	680	760	680	740	690	710	690	690	680-760
(1975)	b*	820	760		820		780		850			760-850
Wells	a*	889	905	874	906	887	896	881	899	896	896	874-906
(1977)	b*	935	923		933		920		949			920-949
Powell	a*	887	850	871	882	860	862	824	823	848	834	823-887
(1978)	b*	1020	861		989		952		870			861-1020
Kretz	a*	700	675	716	703	685	733	694	731	697	717	675-733
(1982: K_D)	b*	745	689		734		784		894			689-894
Kretz	a*	722	763	695	761	708	763	720	750	731	735	695-763
(1982: solvus)	b*	811	797		821		798		868			797-869
Lindsley	a*	740	810	700	(780)	(780)	(780)	(780)	(830)	830	(810)	700-830
(1983: cpx)	b*	830	840		(850)		(870)		(920)			830-920
Lindsley	a*	670	680	670	(670)	(690)	(700)	(680)	(690)	690	(690)	670-700
(1983: opx)	b*	800	690		(780)		(840)		(710)			690-840
This study	a*	780	750	790						780		750-790
(Fig. 2.11)	b*	830	760									760-830
This study	a*	750	780	730						810		730-810
(Fig. 2.14)	b*	850	830									830-850

a* - homogeneous grains; b* - exsolved domains. The bracketed data of Lindsley, 1983, have been estimated for samples outside the compositional range indicated by Lindsley (1983) for projection on the pyroxene quadrilateral. Data from Fonarev and Graphchikov (1982) have been excluded.

Two other areas of regional metamorphism were studied. The samples are from granulites, Varburg, Sweden (Saxena, 1968b) and charnockites from Uusima, Finland (Saxena, 1969). The thermal histories are not as well documented as the samples from the Cape Riche area. Compositions, ternary projections and temperatures for both samples are shown in Table 2.12 for Finland and Table 2.13 for Sweden.

These metamorphic pyroxenes show either similar temperatures from both geothermometers (Varberg, sample 1) or they show the Ca-transfer as the lower temperature reaction. It is possible that in regard to equilibrium in metamorphic rocks we should consider the prograde reactions. There is the possibility that Ca diffusion, being slower than the Fe-Mg exchange, (Loomis et al., 1985 and Brady & McCallister, 1983) lags behind, and that the time during which the temperatures remain at the maximum during metamorphism is insufficient for equilibration. In addition, the loss of water during the granulite facies metamorphism would also slow the calcium diffusion and reinforce this effect.

Table 2.12 Chemical Compositions and Distribution Coefficients of Charnockitic Pyroxenes from Finland (Saxena, 1969)

Wt% Oxide	1 Opx	1 Cpx	3 Opx	3 Cpx	4 Opx	4 Cpx	6 Opx	6 Cpx	7 Opx	7 Cpx
SiO_2	49.1	50.5	48.7	48.6	49.4	50.6	47.8	50.3	47.9	49.2
Al_2O_3	0.3	0.9	0.3	1.0	0.3	0.6	0.3	0.7	0.4	1.2
TiO_2	0.1	0.1	0.1	0.2	0.1	0.1	0.1	0.1	0.1	0.2
FeO#	27.4	11.11	32.2	13.9	32.2	13.0	34.6	15.7	33.9	15.8
MnO	0.23	0.11	0.33	0.15	0.35	0.17	0.40	0.20	0.34	0.15
MgO	18.3	12.8	14.1	10.6	14.5	11.1	11.8	9.8	13.3	9.0
CaO	0.8	22.5	0.9	21.6	1.0	23.5	0.9	21.4	1.0	21.3
Total	96.23	98.01	96.63	96.05	97.85	99.07	95.90	98.20	96.94	96.85
Wo*	1.7	45.7	2.0	45.4	2.2	48.1	2.0	44.3	2.2	44.4
En	53.4	36.5	43.0	31.4	43.6	31.3	37.0	29.3	40.3	28.0
Fs	44.9	17.8	55.1	23.1	54.3	20.6	60.9	26.3	57.6	27.6
$\frac{Fe}{Fe+Mg}$	.457	.328	.562	.424	.555	.397	.622	.473	.588	.496
K_D	.580		.574		.528		.545		.690	
Fe^{2+}-Mg Exchange	820°C		830°C		780°C		790°C		<600°C	
Ca Transfer	<600°C		<600°C		<600°C		<600°C		<600°C	

*Wo, En, Fs determined by projection method of Lindsley and Anderson (1983).
#Total Fe is given as FeO.

Table 2.13 Chemical Compositions and Distribution Coefficients of Granulitic Pyroxenes from Varberg, Sweden (Saxena, 1968)

Wt% Oxide	1 Opx	1 Cpx	4 Opx	4 Cpx	5 Opx	5 Cpx	6 Opx	6 Cpx
SiO_2	51.0	49.9	47.2	49.0	48.2	48.9	46.5	48.5
Al_2O_3	2.3	3.2	0.75	2.1	1.0	1.9	1.0	1.9
TiO_2	0.06	0.20	0.06	0.12	0.06	0.12	0.07	0.14
FeO#	21.1	7.3	33.5	16.1	34.9	16.1	40.0	20.2
MnO	0.09	0.05	0.99	0.42	1.10	0.49	0.77	0.34
MgO	23.9	14.3	11.4	9.2	11.6	8.8	7.3	6.1
CaO	0.48	22.1	0.84	19.9	0.60	19.9	0.90	19.6
Na_2O	0.00	0.6	0.05	0.7	0.00	0.6	0.08	0.6
K_2O	0.00	0.00	0.01	0.00	0.00	0.00	0.00	0.00
Total	98.93	97.65	94.80	98.54	97.46	97.31	96.62	97.38
Wo*	1.0	42.9	2.0	41.3	1.4	41.7	2.1	41.6
En	66.2	44.4	37.0	29.6	36.7	28.8	24.0	20.4
Fs	32.8	12.7	61.0	29.1	61.9	29.5	73.8	38.0
$\frac{Fe}{Fe+Mg}$	.331	.222	.622	.496	.628	.506	.755	.651
K_D Fe^{2+}-Mg Exchange	.577 800°C		.596 820°C		.607 830°C		.606 800°C	
Ca Transfer	800°C		700°C		690°C		640°C	

*Wo, En, Fs determined by projection method of Lindsley and Anderson (1983).
#Total Fe is given as FeO.

3. Summary

The two graphical geothermometers developed from the thermodynamic model have been tested for many rock types. For rapidly cooling igneous rocks (a dike and a pumice rock) the geothermometers predicted coinciding quench temperatures. The plutonic rocks showed a substantial range of temperature between the two geothermometers with the Fe^{2+}-Mg exchange reaction giving the lower temperature. This supports the theory that this exchange reaction proceeds to a lower temperature than the Ca-transfer reaction and indicates that the kinetics of these two reactions are different.

For contact metamorphic rocks and regionally metamorphosed rocks, the two graphical geothermometers compare favorably with two-pyroxene geothermometers derived in other studies. For contact metamorphism, the Fe^{2+}-Mg exchange geothermometer records lower temperatures. For regional metamorphism the two geothermometers record similar temperatures or the realtionships are mixed. These results may help unravel the complex history of such terranes. A further, highly favorable feature of these two geothermometers is the ease of their use.

III. SITE OCCUPANCY IN IRON-RICH ORTHOPYROXENES: EXPERIMENTS AND KINETICS

Pbca orthopyroxenes consist of alternating tetrahedral and octahedral layers parallel to *c* with the octahedral layers consisting of zig-zag chains of regular M1 octahedra and more distorted M2 polyhedra. The tetrahedra are non-equivalent, TA being smaller and more distorted than TB (Fig 3.1). Long-range order-disorder occurs between divalent magnesium and iron atoms in the two M-sites with iron preferring the larger M2 site (first shown experimentally by Ghose, 1965). Large cations such as Ca^{2+} prefer the larger M2 site and Al^{IV}/Si substitution only occurs in the tetrahedra B in orthopyroxenes (Domeneghetti et al., 1985). The distribution of Mg and Fe^{2+} varies as a function of temperature (becoming more ordered at lower temperatures) and chemical composition. A crystal of composition En_{50} would be "pefectly ordered" if all the Mg was in the M1 site and all Fe^{2+} (and Ca) in the M2 site.

The nature of the iron-magnesium order-disorder was discussed initially by Ghose (1961) and Mueller (1962), followed by work on the theory on intracrystalline ion-exchange by Matsui and Banno (1965) and Thompson (1970). Iron-magnesium order-disorder in natural and equilibrated orthopyroxenes has been investigated experimentally by Ghose (1965), Evans et al. (1967), Virgo and Hafner (1969, 1970), Saxena and Ghose (1971), Khristoforov et al. (1974), Besancon (1981a) Domeneghetti et al (1985), Sposato and Besancon (1987) Anovitz et al. (1988) and Saxena et al. (1988).

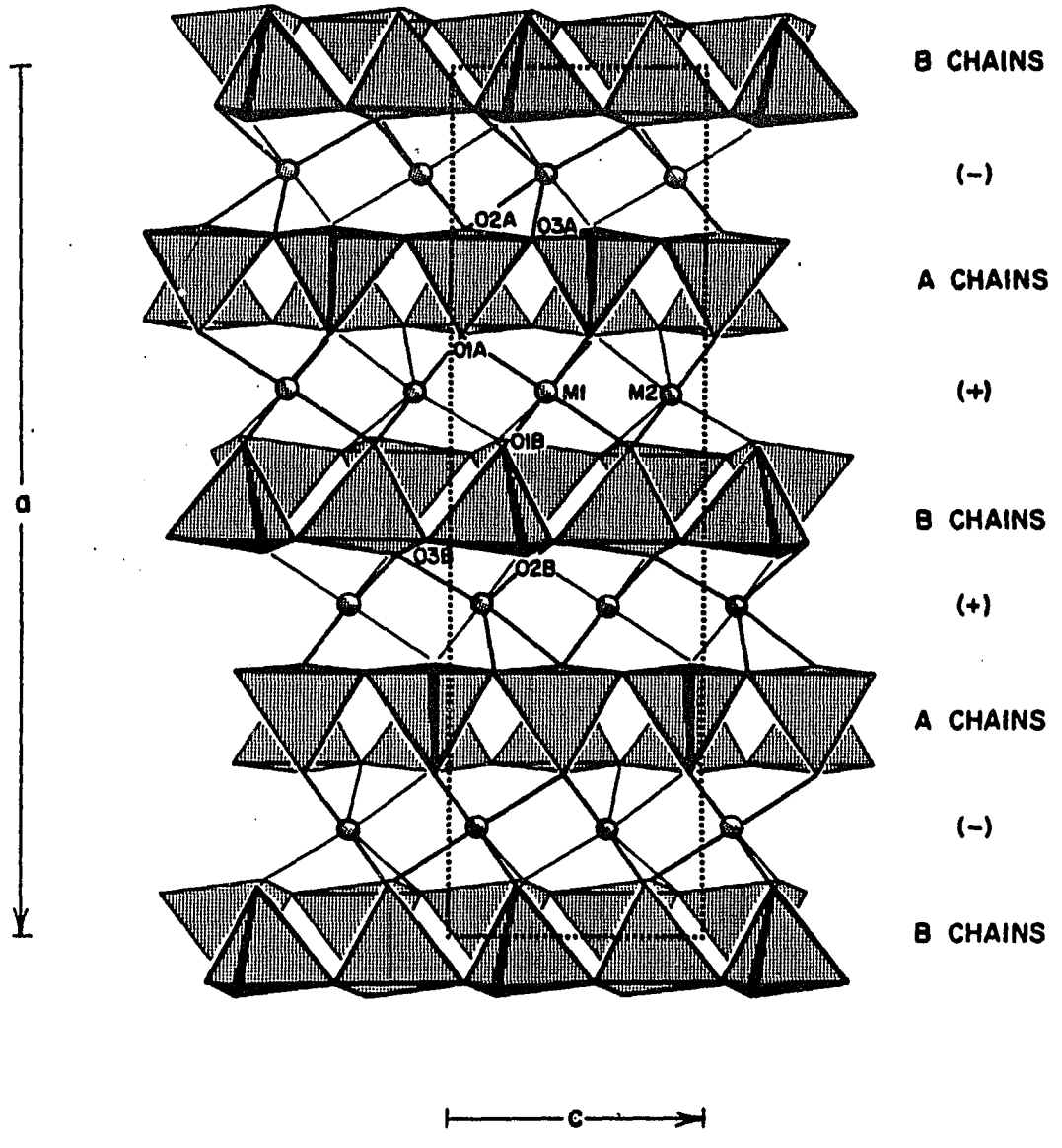

Figure 3.1 The crystal structure of *Pbca* orthopyroxene projected onto the (010) plane. From Cameron and Papike, 1980.

Kinetics of the intracrystalline distribution in orthopyroxenes have been studied by Virgo and Hafner (1969) on one sample, by Besancon (1981a) on two samples and by Anovitz et al., (1988) on two samples. These kinetic studies were all conducted using the Mössbauer technique. In addition, Saxena et al. (1988) studied the kinetics of three samples by X-ray methods. The results of these studies are essential to both the interpretation of the thermal histories of rocks containing orthopyroxene (Besancon, 1981b, Ganguly, 1982, Saxena and Dal Negro, 1983, Anovitz et al., 1988) and the theoretical calculation of two-pyroxene geothermometers (Lindsley, 1983, Saxena, 1983a; 1983b, Davidson, 1985, Davidson and Lindsley, 1985) and pyroxene-olivine phase equilibria (Davidson, 1987a; 1987b). This is further discussed in sections IV (p.146) and V (p.166) in this thesis.

The theory of intracrystalline exchange and the earlier works (using Mössbauer techniques) have been reviewed by Ganguly (1982). He indicated inconsistencies between the equilibrium site occupancies obtained from the three studies. A thermodynamic model was developed; however, the isothermal site distributions thus modeled yield a significantly higher value of Fe^{2+} in M2 for the iron-rich samples than the experimental results.

Ganguly (1982) also presented improvements in the algorithm for determining cooling rates of the pyroxene crystals from the kinetic data of the order-disorder process. He concluded that the methods of estimating cooling rates as first proposed by Mueller, (1962, and subsequently developed by him in 1967 and 1969) and followed by Seifert and Virgo (1975) for an anthophyllite sample, could only be successful if the Fe-Mg site occupancies and the rate constants could be determined

with great precision. This precision is necessary because the calculated cooling rates are very sensitive to uncertainties in the site occupancy determinations.

Domeneghetti et al., (1985) structurally refined orthopyroxenes of three differing compositions and systematically reviewed structural variations as a function of both chemical composition and degree of ordering. This work can now be used as an important framework to constrain future work on order-disorder in equilibrated orthopyroxenes.

In our study, experimental work has been undertaken to determine structural changes, kinetic rates and equilibrium site occupancy data on heated and natural iron-rich orthopyroxene crystals. Many measurements (with increasing heating periods following the intracrystalline exchange) have been made in order to tightly constrain the reaction. Single crystal X-ray refinement and X-ray energy dispersive analysis are used to determine the site occupancies rather than Mössbauer techniques. Using this method, one crystal is used for the natural site occupancy data and heatings with short durations are repeated on the same crystal until equilibrium is attained i.e. no change with further heating. The heating effects on the interaction of cation distribution and structural changes have been studied and compared to that of Domeneghetti et al. (1985), which provides an internal check on the distribution data.

A. Experimental Techniques

1. Samples

Two iron-rich samples have been chosen for this study, both from metamorphic rocks of granulite facies. Sample (4) Fe/(Fe+Mg) = 0.62 is from Uusima, Finland (Saxena, 1969); sample (5) Fe/(Fe+Mg) = 0.82 is from metamorphosed iron-formation in the Wind River Mountains in Wyoming (Sykes, 1984, unpublished Masters Thesis). The compositional data are summarized in Table 3.1. Note that they are dominantly Fe-Mg binary pyroxene in composition. The samples were chosen for three reasons: firstly they complement the data published on site distribution in orthopyroxenes (Domeneghetti et al., 1985); secondly, they are both very iron-rich and compositions like this are rarely studied; and lastly, they are part of an ongoing series of experiments in Padova, Italy to redetermine the set of isothermal curves based on equilibrium site occupancy.

2. Procedures

The following procedure was applied to every crystal:

(a) X-ray data collection and structural refinement of the natural (unheated) crystal;

(b) a series of heating experiments conducted on the same crystal at three temperatures (525, 575, 625 °C for sample 5; 625, 675, 725 °C for sample 4) until a close approximation to the exchange equilibrium was reached. X-ray data collection and structural refinements were carried out after every heating.

(c) X-ray energy dispersive analysis of the same crystal, after the last X-ray data collection.

Table 3.1. Chemical Composition of Samples

	Sample 4		Sample 5	
	Wt.% Oxides	Mol. prop.	Wt.% Oxides	Mol. prop.
SiO_2	50.3	2.01	47.9	1.99
TiO_2	0.1	0.0	0.0	0.0
Al_2O_3	0.0	0.0	0.4	0.04
Cr_2O_3	0.1	0.01	0.0	0.0
FeO*	34.6	1.16	47.4	1.65
MnO	0.6	0.02	0.2	0.1
MgO	12.3	0.73	4.5	0.28
CaO	1.2	0.05	1.2	0.05
Na_2O	0.0	0.0	0.0	0.0
Total	99.26	3.98	101.60	4.1

* all Fe as FeO

Mole proportions are cations per 6 oxygens

3. Sample Preparation

Crystals of orthopyroxene (100-200 μm) are selected using a binocular microscope with emphasis on choosing clear, inclusion-free, equidimensional crystals. These are then immersed in cedar oil and studied with the petrographic microscope to ensure there were no visible exsolution lamellae and the crystal showed perfect extinction parallel to c.

The crystal is completely cleaned and attached to a glass capillary tube (already mounted on a cylinder of brass used for fixing the sample in the diffractometer). The glass tube is of similar dimensions to the crystal. The adhesive used is "Peligom" diluted with amyly acetate, which is readily dissolved in acetone when the crystal is prepared for reheating. When mounting is completed, the crystal is measured in three mutually perpendicular directions, needed for the adsorption correction.

4. X-ray Data Collection and Structural Refinement

Single-crystal X-ray diffraction data are obtained using a computer controlled SIEMENS AED four-circle diffractometer located at the Istituto di Mineralogia e Petrologia at the Universita di Padova, Italy. MoKα radiation monochromatised by a flat graphite crystal is used. (A detailed description of the four-circle diffractometer can be found in X-Ray Structure Determination, Chp. 6, by Stout and Jensen, 1968.)

The crystal is attached to the diffractometer head and centered using the ω (horizontal) and χ (vertical) circles. The preliminary operation is to find the unit cell. This is done by first rotating the

crystal and recording the orientation of intense reflections; approximately five reflections are needed. Using the program MR (STOE) the orientation of the unit cell is calculated including the cell dimensions and angles, and a possible Bravis lattice is suggested. Once the cell has been determined, a more precise calculation is performed by centering 25 major reflections for the orthopyroxene crystal and recalculating the cell parameters. These crystallographic data are then used during the actual data collection. In addition, at this time, a series of measurements on 32 equivalent pairs hkl and $h\bar{k}l$ are collected to calculate the best unit cell (with all angles at 90°). This is done using the DL and LR (STOE) program with three minimization routines. These data are used during the refinement. The equivalent pairs hkl and $h\bar{k}l$ were measured up to $\theta \leq 30^{o}$ using the ω-scan mode. Data collection took approximately 22 hours. The final part of the data collection was at least two ψ scans for the absorption correction.

The third phase consists of the refinement of the collected intensity data using a series of computer programs. The first step is to calculate the observed structure factors (Fo) which are related to the experimentally derived diffraction intensities. These structure factors can also be calculated theoretically (Fc) and from a least squares comparison of the two, site occupancies can be determined.

To convert the intensities into structure factors the data reduction programs CDEDT, FOBS and NORMAL are used. The intensity of

the reflection, I_{hkl} is related to F_{hkl} by

$$I_{hkl} = k \times L \times p \times F^2_{hkl}$$

where

k is the scale factor (dependent on crystal size, beam intensity, etc.) and is normally a constant for a given set of measurements

L is the Lorentz factor, dependent on the technique used and is a function of θ.

p is the polarization factor, a function of 2θ.

The intensities were corrected for absorption following the semi-empirical method of North et al., (1968), (at least two ψ scans were used). The values of the equivalent pairs were averaged. The resulting discrepancy factors:

$$R_{sym} = \Sigma_{hkl}(I_{hkl} - \bar{I})/(\Sigma_{hkl}\bar{I}) \qquad (5)$$

$$\text{where } \bar{I} = (I_{hkl} + I_{\bar{h}\bar{k}\bar{l}})/2$$

ranged between 1.5 and 2.8%.

The refinements were carried out in space group *Pbca* without chemical constraints using the STRUCSY (copywrite STOE) program. The program allows assignment of every site involved in isomorphous replacements of two scattering curves (f1 and f2) and refinement of the occupancy factors (x(f)) with the constraint that x(f1) + x(f2) = 1. The choice of scattering factors was: Mg^{2+} and Fe^{2+} for M1; Mg^{2+} and

Fe^{2+} for M2; $Si^{2.5+}$ for TA and TB; $O^{1.5-}$ for the O-sites. A partial ionization model was adopted in view of the significant differences between Fo and Fc observed for $\sin(\theta/\lambda) = 0 - 0.30$. This choice assured the best fitting of the experimental data based on the International Tables for X-ray Crystallography (1974) and for O^{2-} (Tokonami, 1965).

All the structural sites were considered fully occupied. In the first stages of the refinements, isotropic temperature factors were used. The final cycles were performed allowing all parameters (atomic coordinates, anisotropic temperature factors, M1 and M2 site occupancies, scale factors and secondary extinction coefficient (Zachariasen, 1963) to vary until the shifts were less than the least-squares difference of the corresponding parameters. The reflections with $I \geq 3\sigma(I)$ were considered as observed, and were utilized for the refinements with equal weight. No value of R (the discrepancy factor) greater than 0.045 has been accepted for sample 5, or greater that 0.040 for sample 4 indicating a satisfactory fit of the observed to the calculated site occupancy data.

5. Heating experiments

The crystals were sealed in small silica tubes containing treated (heated and water vapor removed) argon at slightly above 1 atmosphere. The durations of the heating experiments were initially controlled by the temperature, the composition of the pyroxene and the consideration of previous work (Saxena and Ghose, 1971, Besancon, 1981a). The sample was heated in a vertical, temperature controlled furnace (±3°C, Pt/Pt-Rh thermocouple). Quenching of the crystal was almost instantaneous and

was done by dropping the tube into cold water. An estimate of the total quenching time for this method has been made by G.M. Molin (pers. comm. 1987), of 0.5 seconds, for a temperature change of 1150-500°C .

6. X-ray energy dispersive analysis

An energy dispersive spectrometer EDS EG&G connected to a SEM AUTOSCAN electron microscope operating at 15 kV was employed to analyze the single crystals. A MAGIC program (Colby, 1972) in the ORTEC MAGIC IV M. version is used to convert X-ray counts into oxide weight percent. The analyses were averaged over several spots. The results are considered accurate to within 2-3% for the major elements and to about 10% for the minor ones (Table 3.1).

B. Results and Discussions

1. Structural Variations

The structural data for both the natural and heated crystals of this study are consistent with previous data on natural and heated orthopyroxenes (Domeneghetti et al., 1985) and synthetic end members (Ganguly and Ghose, 1979 and Sueno et al., 1976). Most of the crystallographic diagrams used here are based on those of Domeneghetti et al. (1985) and the trends for Al-rich pyroxenes (0.91-4.02 wt% Al_2O_3) are from this paper. Structural data is compiled in Tables 3.2.a - 3.2.j.

The tetrahederal sites, TA and TB, show slight geometrical variations with heating (Fig. 3.2). The general trend, with increasing iron content, is for a lengthening of the <T-O> non-bridging distances and a shortening of the <T-O> bridging bond distances. The mean <T-O> distances for both A and B chains do not change significantly with increasing iron. Samples 5 (this study) and 10 (Domeneghetti et al., 1985), 0.4 and 0.66 wt% Al_2O_3 respectively, deviate slightly from this trend. The <TB-O> bond lengths are slightly longer than expected. Sample 5 also supports the theory (Domeneghetti et al., 1985) that Al^{IV} substitution occurs only in the TB site, resulting in an increase in the <TB-O> bond lengths, especially the <TB-O> non-bridging bonds.

The M1 octahedral site shows a wide variation in size with heating. The mean <M1-O> bond length with respect to Fe^{2+}-M1 occupancy is shown in Figure 3.3 (both natural and heated samples). The arrows indicate the trend with increasing periods of heating. The change in bond lengths is more pronounced for sample 4 as there is a much greater

Table 3.2a Composition and Cell Edges of Natural Sample #4 from Finland

T °C	Time(hr)	FeM1	FeM2	K_D	TOTAL e^-	a(Å)	b(Å)	c(Å)	Vol($Å^3$)
625	0.0	0.300	0.939	0.0278	41.346	18.359	8.967	5.236	861.940
625	0.3	0.352	0.892	0.0658	41.416	18.365	8.969	5.236	862.520
625	0.7	0.370	0.859	0.0964	41.206	18.366	8.971	5.237	862.870
625	1.0	0.391	0.850	0.1133	41.374	18.368	8.972	5.236	862.850
625	2.0	0.393	0.834	0.1289	41.178	18.369	8.969	5.235	862.560
625	5.0	0.403	0.824	0.1442	41.178	18.365	8.972	5.236	862.720
625	30.0	0.408	0.802	0.1701	40.940	18.368	8.972	5.234	862.660
625	100.0	0.411	0.746	0.2376	40.198	18.315	8.663	5.233	860.750
675	0.0	0.296	0.953	0.0207	41.486	18.362	8.964	5.234	861.560
675	0.3	0.362	0.860	0.0924	41.108	18.364	8.977	5.237	863.270
675	0.5	0.387	0.841	0.1194	41.192	18.368	8.977	5.236	863.400
675	0.7	0.392	0.839	0.1237	41.234	18.369	8.980	5.237	863.820
675	0.0	0.291	0.937	0.0276	41.192	18.354	8.974	5.236	862.420
675	0.2	0.352	0.879	0.0748	41.234	18.361	8.978	5.235	863.070
675	0.5	0.378	0.844	0.1123	41.108	18.369	8.977	5.237	863.440
675	2.0	0.392	0.832	0.1302	41.136	18.374	8.981	5.236	863.980
725	0.0	0.288	0.942	0.0249	41.220	18.356	8.968	5.234	861.603
725	0.1	0.425	0.804	0.1802	41.206	18.370	8.971	5.236	862.780
725	0.2	0.411	0.789	0.1866	40.800	18.369	8.973	5.233	862.520
725	0.3	0.422	0.784	0.2012	40.884	18.366	8.972	5.233	862.280
725	0.8	0.422	0.784	0.2012	40.884	18.367	8.972	5.234	862.420
725	3.0	0.426	0.740	0.2608	40.324	18.351	8.965	5.232	860.870

Table 3.2b Composition and Cell Edges of Natural Sample #5 from Wyoming

T °C	Time(hr)	FeM1	FeM2	K_D	Total e^-	a(Å)	b(Å)	c(Å)	Vol($Å^3$)
525	0.0	0.713	0.959	0.1062	47.408	18.412	9.026	5.244	871.440
525	0.1	0.720	0.965	0.0933	47.590	18.416	9.025	5.245	871.650
525	0.3	0.719	0.950	0.1347	47.366	18.410	9.027	5.244	871.550
525	0.5	0.731	0.962	0.1073	47.702	18.416	9.027	5.242	871.420
525	2.0	0.747	0.945	0.1718	47.688	18.415	9.025	5.244	871.520
525	576.0	0.741	0.893	0.3428	46.876	18.404	9.022	5.246	871.050
575	0.0	0.704	0.958	0.1043	47.268	18.410	9.031	5.246	871.640
575	0.1	0.717	0.948	0.1390	47.310	18.412	9.030	5.245	871.940
575	0.2	0.690	0.925	0.1805	46.610	18.415	9.030	5.242	871.610
575	0.3	0.718	0.935	0.1770	47.142	18.414	9.030	5.243	871.840
575	0.5	0.713	0.929	0.1899	46.988	18.414	9.030	5.244	871.950
575	2.0	0.718	0.933	0.1828	47.114	18.416	9.031	5.244	872.150
575	10.0	0.726	0.928	0.2056	47.156				
625	0.0	0.708	0.956	0.1116	47.296	18.416	9.028	5.244	871.970
625	0.2	0.732	0.920	0.2375	47.128	18.418	9.028	5.244	871.990
625	0.4	0.740	0.920	0.2475	47.240	18.416	9.033	5.245	872.600
625	0.5	0.744	0.918	0.2596	47.268	18.419	9.031	5.243	872.131
625	1.5	0.747	0.913	0.2814	47.240	18.414	9.029	5.243	871.720
625	4.5	0.749	0.918	0.2666	47.338	18.413	9.027	5.245	871.700
625	0.0	0.714	0.963	0.0959	47.478	18.417	9.028	5.245	872.010
625	0.1	0.740	0.917	0.2576	47.198	18.420	9.029	5.244	872.150

Table 3.2c Tetrahedral Bond Lengths in Sample #4 from Finland

T °C	Time(hr)	TA-01A	TA-02A	TA-03A	TA-03A	TA-O mean	TA-O bridging	TA-O non-bridging
625	0.0	1.610	1.601	1.631	1.659	1.626	1.645	1.606
625	0.3	1.612	1.599	1.637	1.657	1.626	1.647	1.605
625	0.7	1.612	1.602	1.637	1.659	1.628	1.648	1.610
625	1.0	1.610	1.599	1.638	1.655	1.626	1.647	1.605
625	2.0	1.610	1.601	1.632	1.647	1.626	1.647	1.605
625	5.0	1.614	1.599	1.638	1.657	1.627	1.647	1.606
625	30.0	1.617	1.602	1.635	1.658	1.628	1.647	1.609
625	100.0	1.613	1.600	1.628	1.658	1.625	1.643	1.606
675	0.0	1.611	1.599	1.637	1.655	1.625	1.646	1.605
675	0.3	1.613	1.604	1.635	1.658	1.627	1.647	1.608
675	0.5	1.615	1.603	1.638	1.655	1.628	1.646	1.609
675	0.7	1.606	1.601	1.642	1.654	1.626	1.648	1.603
675	0.0	1.608	1.602	1.636	1.657	1.626	1.647	1.605
675	0.2	1.611	1.597	1.634	1.662	1.626	1.648	1.604
675	0.5	1.613	1.599	1.643	1.655	1.627	1.649	1.606
675	2.0	1.616	1.591	1.640	1.656	1.626	1.648	1.603
725	0.0	1.613	1.600	1.630	1.657	1.625	1.644	1.607
725	0.1	1.610	1.595	1.642	1.649	1.624	1.645	1.602
725	0.2	1.616	1.593	1.637	1.653	1.625	1.645	1.604
725	0.3	1.612	1.594	1.636	1.662	1.626	1.649	1.603
725	0.8	1.614	1.599	1.644	1.647	1.626	1.646	1.607
725	3.0	1.609	1.599	1.635	1.659	1.625	1.647	1.604

Table 3.2d Tetrahedral Bond Lengths in Sample #5 from Wyoming

T°C	Time(hr)	TA-01A	TA-02A	TA-03A	TA-03A	TA-O Mean	TA-O Bridging	TA-O Non-Bridging
525	0.0	1.614	1.601	1.636	1.655	1.626	1.645	1.607
525	0.1	1.616	1.602	1.638	1.650	1.626	1.644	1.609
525	0.3	1.610	1.594	1.630	1.658	1.623	1.644	1.602
525	0.5	1.613	1.600	1.637	1.657	1.627	1.647	1.607
525	2.0	1.614	1.599	1.639	1.649	1.625	1.644	1.606
525	576.0	1.616	1.601	1.638	1.651	1.627	1.644	1.609
575	0.0	1.610	1.603	1.633	1.658	1.626	1.645	1.607
575	0.1	1.614	1.601	1.643	1.648	1.626	1.645	1.608
575	0.2	1.613	1.598	1.636	1.656	1.626	1.646	1.606
575	0.3	1.610	1.603	1.647	1.647	1.627	1.647	1.607
575	0.5	1.611	1.600	1.641	1.650	1.625	1.646	1.605
575	2.0	1.613	1.601	1.641	1.654	1.627	1.647	1.607
575	10.0	1.610	1.602	1.645	1.653	1.628	1.649	1.606
625	0.0	1.616	1.601	1.640	1.649	1.626	1.644	1.608
625	0.2	1.615	1.602	1.627	1.661	1.626	1.644	1.608
625	0.4	1.616	1.604	1.640	1.649	1.627	1.645	1.610
625	0.5	1.615	1.595	1.636	1.655	1.625	1.645	1.605
625	1.5	1.612	1.601	1.635	1.657	1.626	1.646	1.607
625	4.5							
625	0.0	1.616	1.601	1.635	1.653	1.626	1.644	1.608
625	0.1	1.616	1.597	1.636	1.649	1.624	1.643	1.606

Table 3.2e Tetrahedral Bond Lengths in (Å's) of Natural Sample #4 from Finland

T °C	Time(hr)	TB-01B	TB-02B	TB-03B	TB-03B	TB-O mean	TB-O bridging	TB-O non-bridging
625	0.0	1.623	1.598	1.661	1.672	1.639	1.667	1.610
625	0.3	1.624	1.604	1.665	1.669	1.641	1.667	1.614
625	0.7	1.621	1.599	1.669	1.670	1.640	1.670	1.610
625	1.0	1.622	1.595	1.665	1.671	1.638	1.668	1.608
625	2.0	1.625	1.600	1.668	1.670	1.641	1.669	1.613
625	5.0	1.624	1.601	1.666	1.669	1.640	1.668	1.612
625	30.0	1.623	1.600	1.664	1.669	1.639	1.666	1.612
625	100.0	1.621	1.600	1.663	1.665	1.637	1.664	1.610
675	0.0	1.623	1.598	1.667	1.666	1.638	1.667	1.610
675	0.3	1.624	1.597	1.674	1.662	1.639	1.668	1.610
675	0.5	1.621	1.598	1.673	1.666	1.640	1.670	1.609
675	0.7	1.625	1.597	1.670	1.667	1.640	1.669	1.611
675	0.0	1.623	1.598	1.670	1.668	1.640	1.669	1.611
675	0.2	1.619	1.600	1.672	1.669	1.640	1.671	1.610
675	0.5	1.623	1.601	1.671	1.667	1.640	1.669	1.619
675	2.0	1.620	1.601	1.672	1.669	1.641	1.671	1.611
725	0.0	1.619	1.599	1.667	1.668	1.638	1.667	1.609
725	0.1	1.624	1.593	1.664	1.674	1.639	1.669	1.608
725	0.2	1.623	1.602	1.665	1.671	1.640	1.668	1.612
725	0.3	1.623	1.606	1.661	1.672	1.641	1.667	1.614
725	0.8	1.618	1.588	1.665	1.669	1.635	1.667	1.603
725	3.0	1.625	1.595	1.665	1.666	1.638	1.665	1.610

Table 3.2f Tetrahedral Bond Lengths in (Å) of Natural Sample #5 from Wyoming

T °C	Time(hr)	TB-01B	TB-02B	TB-03B	TB-03B	TB-O mean	TB-O bridging	TB-O non-bridging
525	0.0	1.628	1.599	1.668	1.670	1.641	1.669	1.614
525	0.1	1.632	1.603	1.666	1.666	1.642	1.666	1.618
525	0.3	1.626	1.599	1.666	1.666	1.639	1.666	1.613
525	0.5	1.629	1.599	1.668	1.668	1.641	1.668	1.614
525	2.0	1.630	1.602	1.664	1.673	1.642	1.668	1.616
525	576.0	1.633	1.598	1.662	1.670	1.641	1.666	1.615
575	0.0	1.628	1.601	1.666	1.668	1.641	1.667	1.615
575	0.1	1.635	1.601	1.668	1.667	1.643	1.668	1.618
575	0.2	1.620	1.606	1.667	1.665	1.639	1.666	1.613
575	0.3	1.627	1.607	1.669	1.668	1.645	1.668	1.617
575	0.5	1.628	1.601	1.665	1.675	1.642	1.670	1.614
575	2.0	1.627	1.600	1.667	1.672	1.642	1.669	1.614
575	10.0	1.633	1.605	1.669	1.668	1.644	1.669	1.619
625	0.0	1.632	1.602	1.667	1.667	1.642	1.667	1.617
625	0.2	1.624	1.601	1.662	1.679	1.641	1.670	1.612
625	0.4	1.626	1.590	1.664	1.676	1.639	1.670	1.608
625	0.5	1.628	1.599	1.665	1.671	1.641	1.668	1.613
625	1.5	1.631	1.598	1.666	1.667	1.640	1.666	1.615
625	4.5							
625	0.0	1.627	1.598	1.666	1.671	1.640	1.668	1.613
625	0.1	1.630	1.604	1.668	1.669	1.643	1.668	1.617

Table 3.2g M1-O Bond Lengths in Sample #4 from Finland

T °C	Time(hr)	M1-O1A	M1-O1A	M1-O1B	M1-O1B	M1-O2A	M1-O2B	M1-O mean	Vol(Å^3) M1
625	0.0	2.055	2.159	2.178	2.079	2.058	2.088	2.103	12.260
625	0.3	2.053	2.162	2.181	2.081	2.058	2.084	2.103	12.266
625	0.7	2.053	2.164	2.181	2.088	2.055	2.087	2.105	12.291
625	1.0	2.054	2.164	2.179	2.088	2.057	2.086	2.105	12.300
625	2.0	2.055	2.165	2.181	2.084	2.056	2.085	2.104	12.280
625	5.0	2.055	2.166	2.179	2.083	2.060	2.087	2.105	12.290
625	30.0	2.053	2.161	2.183	2.083	2.054	2.087	2.103	12.270
625	100.0	2.052	2.166	2.178	2.078	2.059	2.086	2.101	12.230
675	0.0	2.047	2.160	2.177	2.080	2.059	2.087	2.102	12.241
675	0.3	2.053	2.166	2.181	2.082	2.056	2.090	2.105	12.290
675	0.5	2.056	2.165	2.183	2.089	2.055	2.089	2.106	12.320
675	0.7	2.057	2.173	2.183	2.085	2.058	2.090	2.108	12.348
675	0.0	2.050	2.162	2.179	2.076	2.058	2.089	2.103	12.255
675	0.2	2.050	2.166	2.185	2.083	2.064	2.089	2.106	12.314
675	0.5	2.048	2.168	2.180	2.084	2.061	2.088	2.105	12.290
675	2.0	2.059	2.162	2.184	2.084	2.066	2.088	2.108	12.351
725	0.0	2.048	2.161	2.174	2.081	2.059	2.086	2.101	12.240
725	0.1	2.063	2.166	2.181	2.078	2.063	2.089	2.106	12.320
725	0.2	2.052	2.166	2.177	2.092	2.061	2.085	2.106	12.306
725	0.3	2.055	2.161	2.181	2.085	2.062	2.084	2.105	12.295
725	0.8	2.052	2.168	2.178	2.086	2.052	2.094	2.105	12.302
725	3.0	2.056	2.165	2.178	2.080	2.048	2.087	2.102	12.250

Table 3.2h M1-O Bond Lengths in Sample #5 from Wyoming

T °C	Time(hr)	M1-O1A	M1-O1A	M1-O1B	M1-O1B	M1-O2A	M1-O2B	M1-O Mean	Vol(Å^3) M1
525	0.0	2.072	2.176	2.187	2.100	2.076	2.106	2.119	12.545
525	0.1	2.073	2.178	2.183	2.105	2.075	2.104	2.120	12.550
525	0.3	2.079	2.182	2.186	2.104	2.076	2.104	2.120	12.588
525	0.5	2.074	2.179	2.186	2.104	2.072	2.106	2.120	12.553
525	2.0	2.073	2.180	2.183	2.108	2.077	2.100	2.120	12.560
525	576.0	2.074	2.174	2.187	2.097	2.069	2.104	2.117	12.510
575	0.0	2.075	2.179	2.184	2.101	2.071	2.106	2.119	12.550
575	0.1	2.071	2.181	2.177	2.101	2.072	2.105	2.118	12.515
575	0.2	2.066	2.184	2.190	2.104	2.077	2.099	2.120	12.560
575	0.3	2.070	2.181	2.184	2.104	2.073	2.103	2.119	12.540
575	0.5	2.076	2.181	2.185	2.103	2.075	2.107	2.121	12.580
575	2.0	2.076	2.179	2.189	2.105	2.072	2.105	2.121	12.570
575	10.0	2.075	2.177	2.185	2.102	2.070	2.107	2.119	12.540
625	0.0	2.071	2.178	2.179	2.105	2.071	2.101	2.118	12.520
625	0.2	2.079	2.178	2.185	2.114	2.070	2.098	2.121	12.564
625	0.4	2.078	2.177	2.189	2.102	2.073	2.113	2.122	12.591
625	0.5	2.077	2.179	2.185	2.107	2.077	2.105	2.122	12.583
625	1.5	2.075	2.177	2.182	2.103	2.070	2.104	2.119	12.530
625	4.5								
625	0.0	2.071	2.179	2.181	2.101	2.075	2.105	2.118	12.530
625	0.1	2.075	2.179	2.184	2.105	2.076	2.103	2.120	12.560

Table 3.2i M2-O Bond Lengths in Sample #4 from Finland

T °C	Time(hr)	M2-O1A	M2-O1B	M2-O2A	M2-O2B	M2-O3A	M2-O3B	M2-O mean	Vol(Å^3) M2
625	0.0	2.168	2.129	2.052	2.007	2.414	2.560	2.222	13.413
625	0.3	2.168	2.127	2.055	2.002	2.408	2.556	2.219	13.378
625	0.7	2.163	2.128	2.050	2.005	2.405	2.553	2.217	13.364
625	1.0	2.170	2.124	2.052	2.012	2.406	2.554	2.220	13.404
625	2.0	2.167	2.123	2.053	2.002	2.407	2.551	2.217	13.360
625	5.0	2.163	2.127	2.051	2.002	2.406	2.557	2.218	13.350
625	30.0	2.168	2.124	2.053	2.001	2.407	2.561	2.219	13.380
625	100.0	2.164	2.129	2.056	2.003	2.408	2.565	2.221	13.420
675	0.0	2.169	2.128	2.049	2.007	2.414	2.561	2.221	13.400
675	0.3	2.163	2.128	2.050	2.006	2.411	2.557	2.219	13.390
675	0.5	2.162	2.125	2.049	2.003	2.410	2.556	2.218	13.360
675	0.7	2.167	2.121	2.045	2.009	2.409	2.555	2.218	13.360
675	0.0	2.171	2.131	2.046	2.006	2.415	2.558	2.221	13.403
675	0.2	2.168	2.127	2.047	2.004	2.412	2.554	2.219	13.366
675	0.5	2.167	2.129	2.049	2.004	2.404	2.556	2.218	13.370
675	2.0	2.161	2.126	2.053	2.004	2.410	2.554	2.218	13.358
725	0.0	2.169	2.136	2.047	2.010	2.416	2.555	2.222	13.429
725	0.1	2.161	2.128	2.047	2.006	2.406	2.553	2.217	13.350
725	0.2	2.164	2.121	2.046	2.006	2.407	2.552	2.216	13.331
725	0.3	2.162	2.121	2.050	2.001	2.404	2.556	2.217	13.343
725	0.8	2.164	2.131	2.052	2.012	2.406	2.562	2.221	13.420
725	3.0	2.164	2.123	2.057	2.007	2.404	2.561	2.219	13.400

Table 3.2j M2-O Bond Lengths in Sample #5 from Wyoming

T °C	Time(hr)	M2-O1A	M2-O1B	M2-O2A	M2-O2B	M2-O3A	M2-O3B	M2-O Mean	Vol(Å^3) M2
525	0.0	2.172	2.126	2.040	2.110	2.441	2.563	2.224	13.442
525	0.1	2.166	2.126	2.041	1.996	2.445	2.567	2.223	13.426
525	0.3	2.169	2.129	2.044	2.004	2.446	2.569	2.227	13.506
525	0.5	2.168	2.125	2.041	1.996	2.438	2.563	2.220	13.420
525	2.0	2.171	2.125	2.038	2.003	2.441	2.563	2.223	13.420
525	576.0	2.170	2.125	2.053	2.003	2.440	2.572	2.227	13.490
575	0.0	2.173	2.132	2.045	1.999	2.445	2.566	2.227	13.500
575	0.1	2.172	2.130	2.047	2.001	2.441	2.563	2.226	13.480
575	0.2	2.174	2.137	2.044	2.002	2.442	2.572	2.228	13.520
575	0.3	2.177	2.130	2.041	1.999	2.438	2.563	2.225	13.440
575	0.5	2.170	2.129	2.041	1.998	2.441	2.561	2.223	13.430
575	2.0	2.171	2.127	2.047	2.001	2.438	2.563	2.224	13.460
575	10.0	2.182	2.127	2.041	1.997	2.439	2.563	2.225	13.450
625	0.0	2.170	2.127	2.041	2.001	2.444	2.562	2.226	13.460
625	0.2	2.165	2.126	2.050	2.006	2.443	2.562	2.226	13.490
625	0.4	2.169	2.130	2.048	2.006	2.443	2.567	2.227	13.505
625	0.5	2.169	2.129	2.044	2.005	2.441	2.568	2.226	13.482
625	1.5	2.172	2.129	2.049	2.004	2.444	2.574	2.229	13.527
625	4.5								
625	0.0	2.175	2.136	2.042	2.002	2.444	2.570	2.228	13.514
625	0.1	2.172	2.126	2.043	1.996	2.446	2.568	2.225	13.457

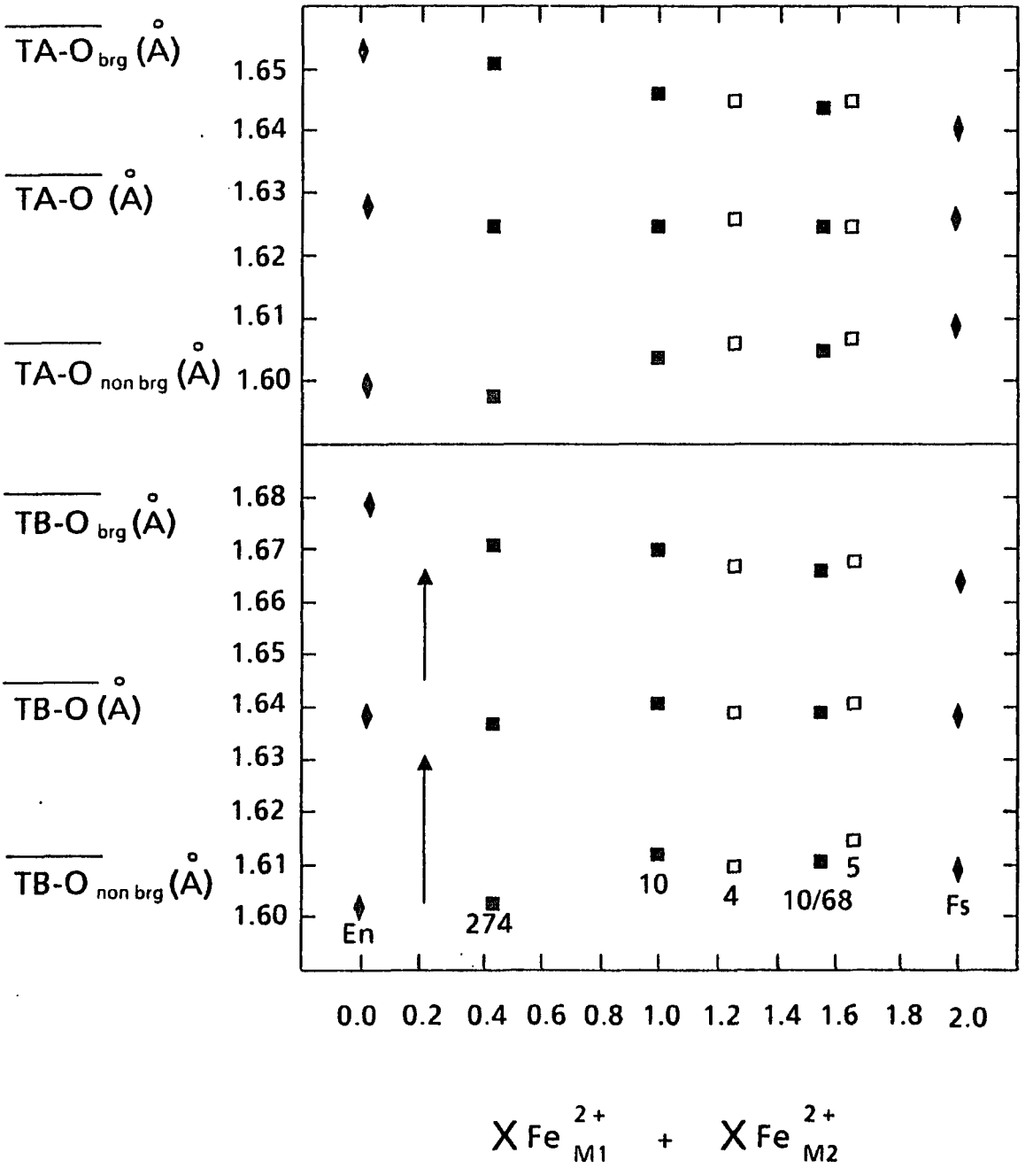

Figure 3.2 Mean tetrahedral bond lengths plotted against total iron content. Open squares are natural samples from this study; filled squares are natural samples from Domeneghetti et al., 1985; filled diamonds represent synthetic enstatite (En) from Ganguly and Ghose, 1979, and synthetic ferrosilite (Fs) from Sueno et al., 1976. Arrows indicate the trend with increasing Al^{IV} from Domeneghetti et al., 1985.

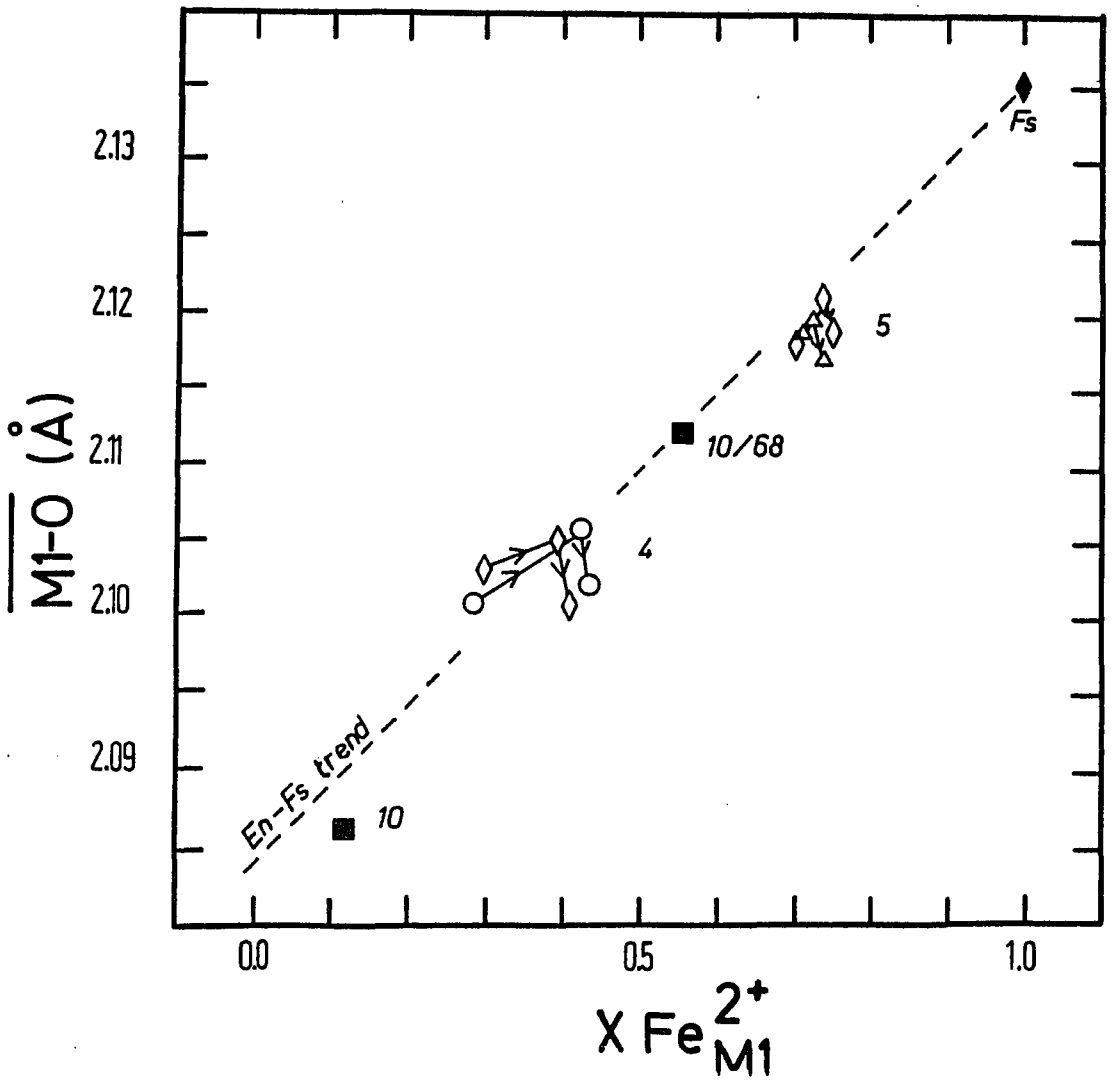

Figure 3.3 Variation in mean M1-O bond lengths with Fe^{2+} in the M1 site. Open circles are for heating at 725°C (sample 4), open diamonds are for 625°C (samples 4 and 5) and open triangles are for 525°C (sample 5). Other symbols as in Figure 3.2. The En-Fs trend is from Domeneghetti et al., 1985. The arrows indicate bond length changes with increasing heating.

disorder possibility due to the smaller amount of iron. Initially, the <M1-O> bond lengths increase parallel to the En-Fs trend. This is as expected with increasing Fe^{2+} entering the M1 site. However, with further heating the <M1-O> bond length drops significantly with almost constant Fe^{2+} in M1. This effect, not related to the disorder degree, will be discussed later in this chapter.

The M2 site has an irregular coordination with the six oxygens. Figure 3.4 shows the variation in the M2-O3A bond length with respect to total iron for the natural samples. The dotted line shows the general trend and the increase in size is very regular. Samples 4 and 5 lie slightly off the expected trend with the bond lengths being slightly longer. As these are all natural samples, this effect could occur due to a higher amount of Fe^{2+} in the M2 site, i.e. a more ordered natural sample than the others indicating a longer cooling history.

The regular increase in the M2-O3B bond length with composition is shown in Figure 3.5, with the dotted line indicating the trend. Samples 10 and 5 have slightly shorter M2-O3B bond lengths. This feature compares well with the decrease in size of the <TB-O> bond lengths due to a small amount of Al^{IV} in the TB site.

Variations in the volume of the unit cell are also linear compared to the total iron content. Much more data is available on the unit cell volume; the method is not time consuming compared to obtaining a complete refinement of the orthopyroxene structure to obtain data on the site occupancy. The samples are from Ross and Huebner (1979). With heating the unit cell increases in volume due to iron entering and enlarging the smaller M1 site. The M2 site does not decrease in size with the addition of the smaller Mg atom. The volume change on heating,

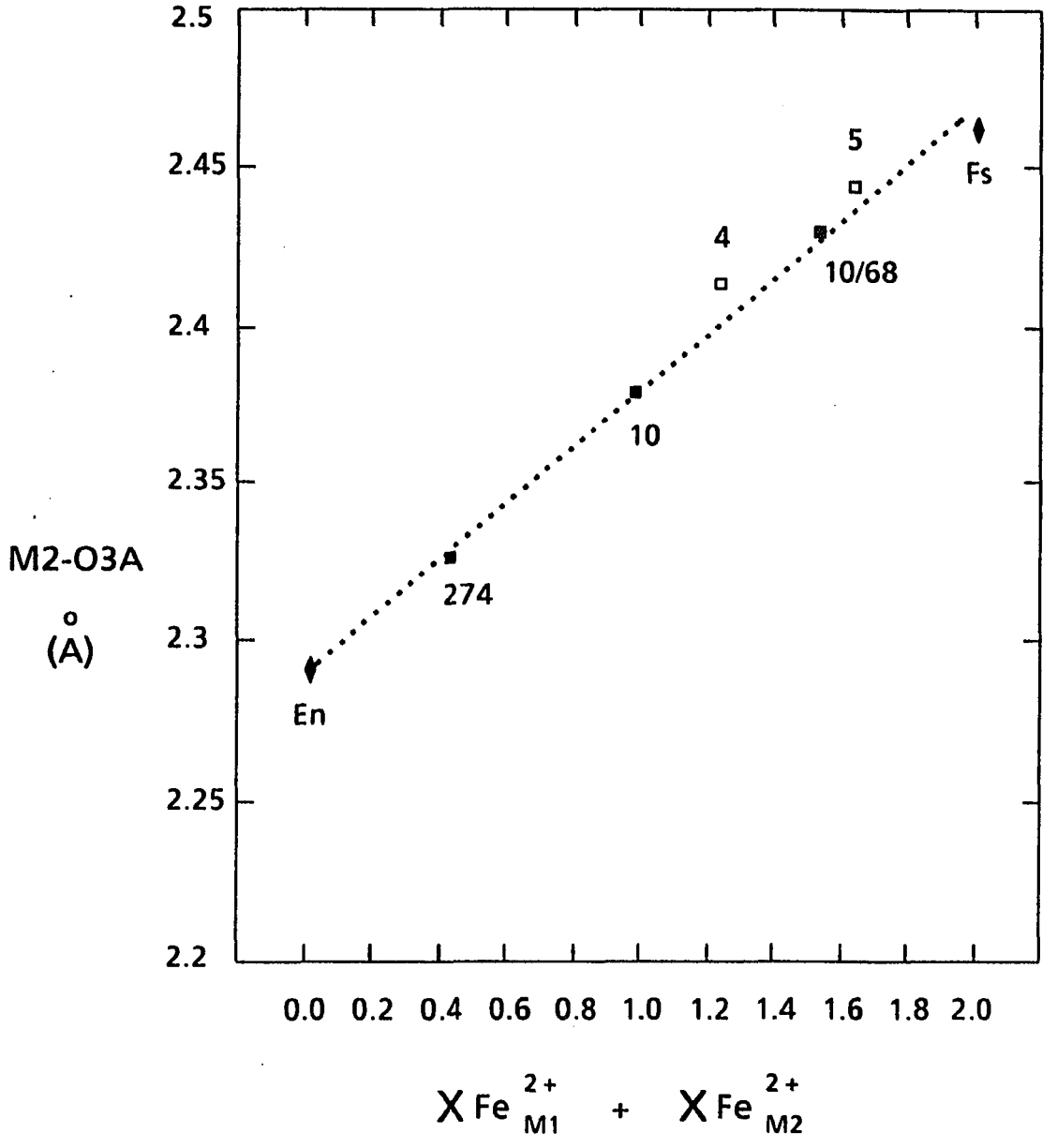

Figure 3.4 Variation of M2-O3A bond lengths with total iron content. Same symbols as for Figure 3.2.

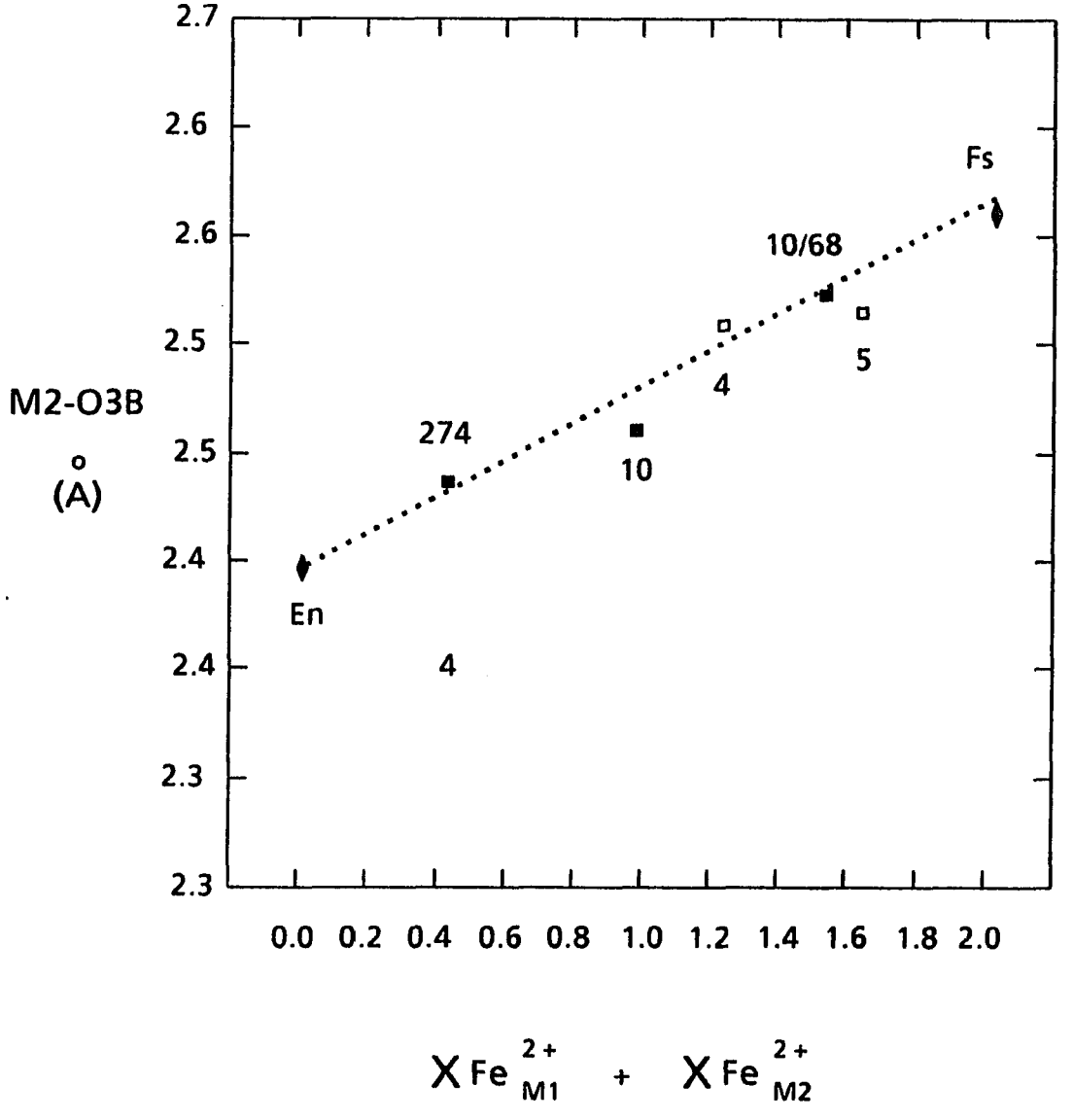

Figure 3.5 Variation of M2-O3B bond lengths with total iron content. Symbols as for Figure 3.2.

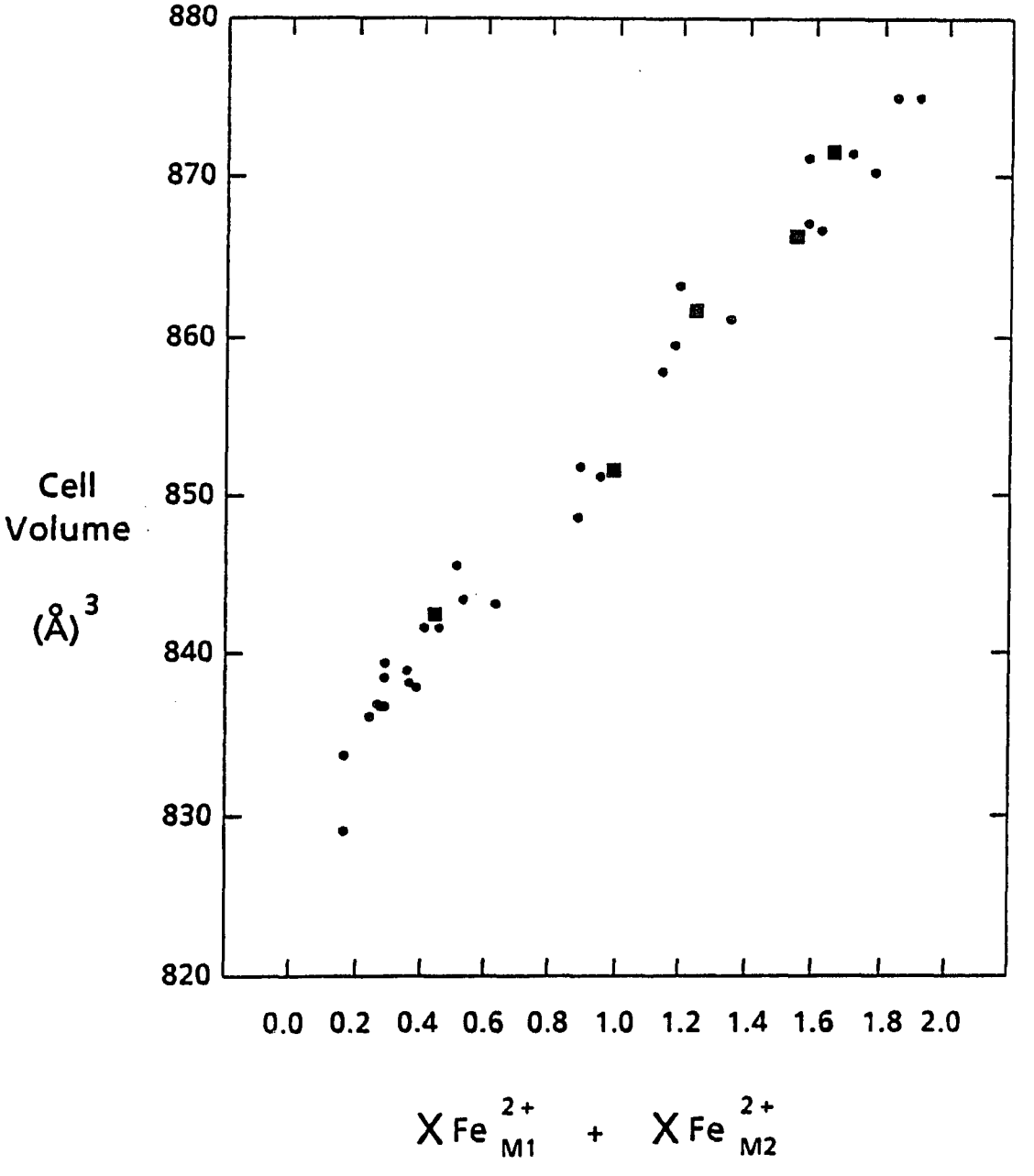

Figure 3.6 Variation of unit cell volume with total iron content. Filled circles are for samples from Ross and Huebner (1979). Filled squares are for samples 4 and 5 of this study and 274, 10 and 10/68 are from Domeneghetti et al. (1985).

although noted for each individual crystal, is within the scatter of Figure 3.6.

Although all the bond lengths and the cell volume increase quite linearly with composition, the distribution of Fe^{2+} between the two sites is not equal. Figure 3.7 indicates how the sites are infilled. Initially the Fe^{2+} enters into the M2 site rapidly, then between 50-66% Fe^{2+}, the rates change and the M1 site is filled preferentially. A change in the kinetic rates of the site-exchange reaction and the energy interactions of the sites may occur around this compsition.

Fig. 3.8 shows the results of the heating experiments at three different temperatures for each composition. The heating experiments proceed as expected with Fe^{2+}M2 decreasing, Fe^{2+}M1 increasing, total electrons (the sum of Fe^{2+} in M1 and M2 multiplied by 26 and of Mg in M1 and M2 multiplied by 12) remaining constant and the M1-O bond length increasing as Fe^{2+} enters the M1 site (see also fig. 3.2) until the crystals reach equilibrium. These data can be used to derive kinetic rates as discussed later.

After the equilibrium state was attained some of the samples (#4 at 625°C and 725°C, #5 at 525°C) were heated for an additional period of time. We noted a decrease in total electrons shown as a further decrease of Fe^{2+} in M2 indicating instability in the crystal structure (iron in M1 remained constant). For sample 4 the structural instability occurs between 5 and 30 hours at 625°C and after only 45 mins at 725°C. For sample 5 at 525°C, a loss in electrons is noted after 31 days. This phenomenon will be discussed before continuing with the kinetics.

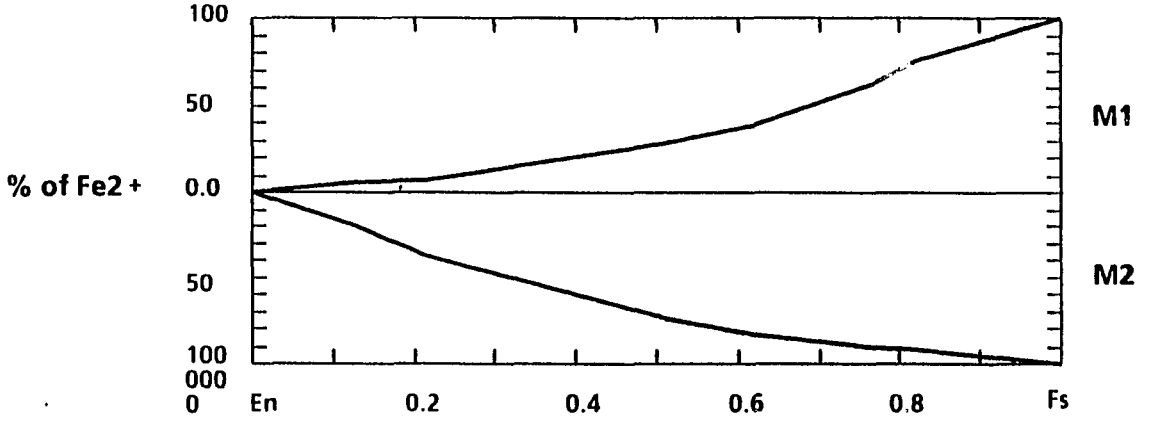

Figures 3.7 Infilling of both the M1 and M2 sites with respect to total iron content of the sample. Enstatite-ferrosilite join at 700°C.

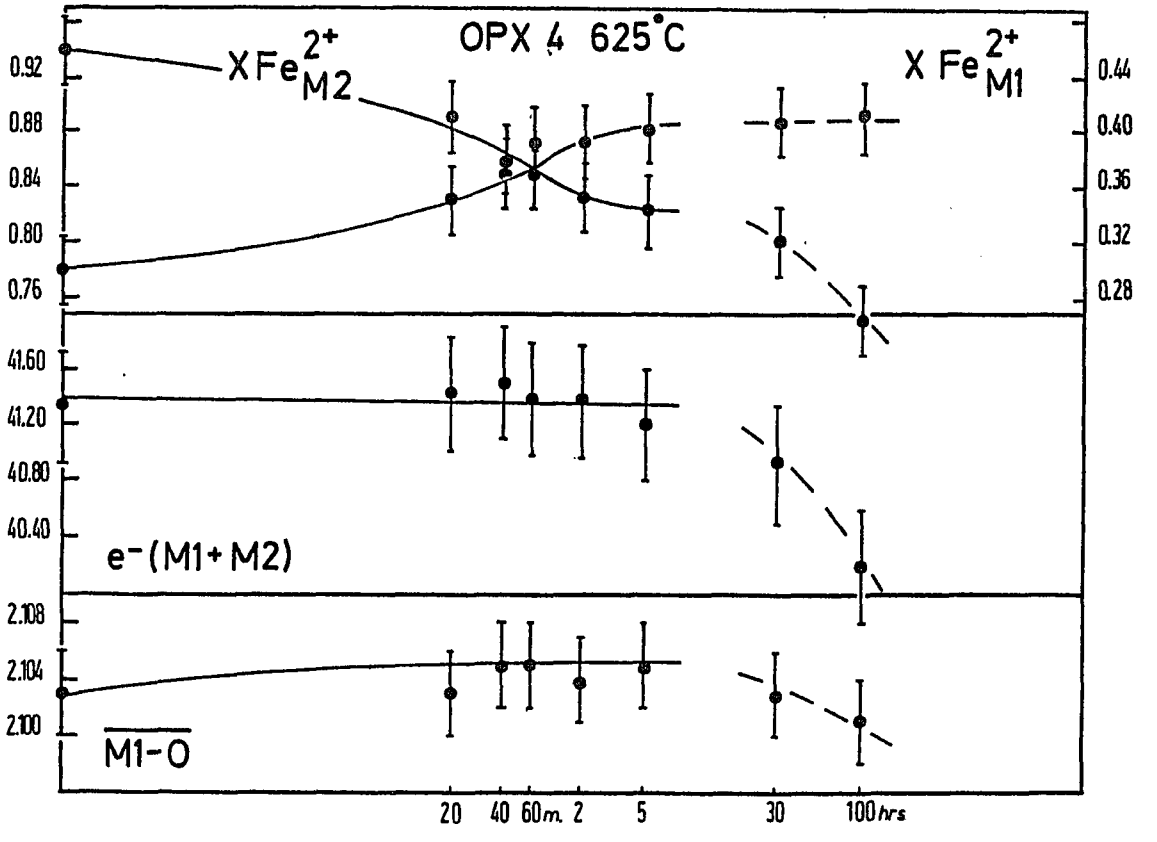

Figure 3.8.a. Summary of the heating experiments for sample #4 at 625°C. The upper section shows the changes in Fe^{2+} in M1 and M2 sites with progressive heating. The central section shows the changes in the total electrons. The lowest section shows the changes in the mean <M1-O> bond lengths. (Error bars in all sections are three standard deviations.) The general trend is for an increase in Fe^{2+} in M1 with a corresponding decrease in M2. The total electrons remain constant. An increase in the volume of the M1 site accompanies the increase in the amount of Fe^{2+} in this site.

The dotted region on the far right of this and Figures 3.3.c and 3.3.d show instability in the crystal. This is discussed further in the text.

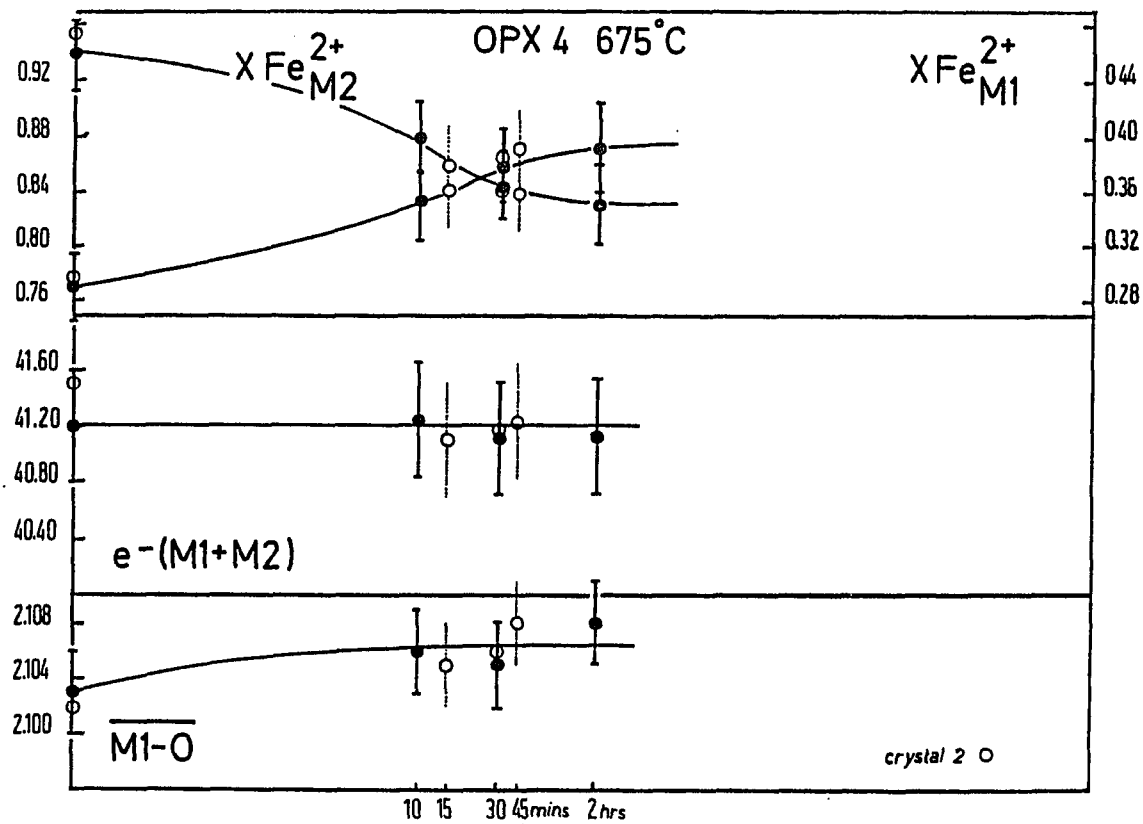

Figure 3.8b. Summary of heating experiments for sample 4 at 675°C. See caption for Figure 3.8a for other details.

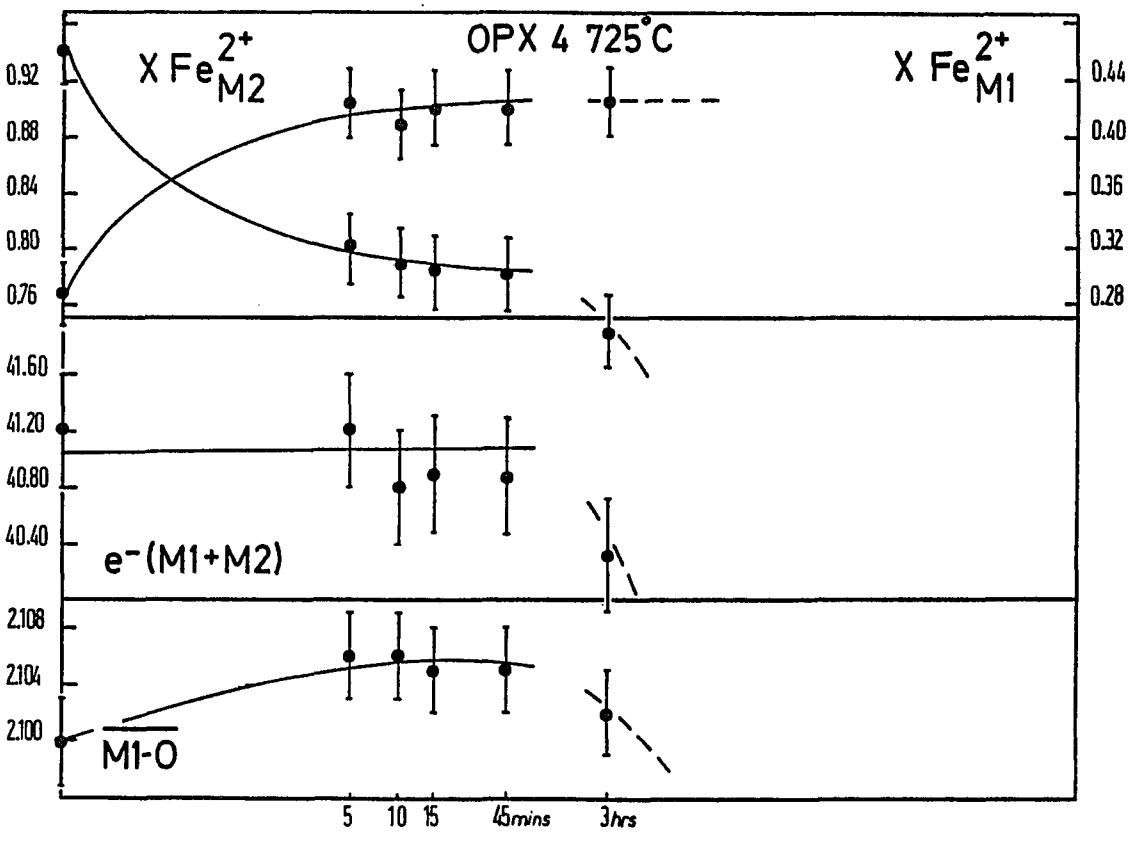

Figure 3.8c. Summary of heating experiments for sample 4 at 725°C. See caption for Figure 3.8a for other details.

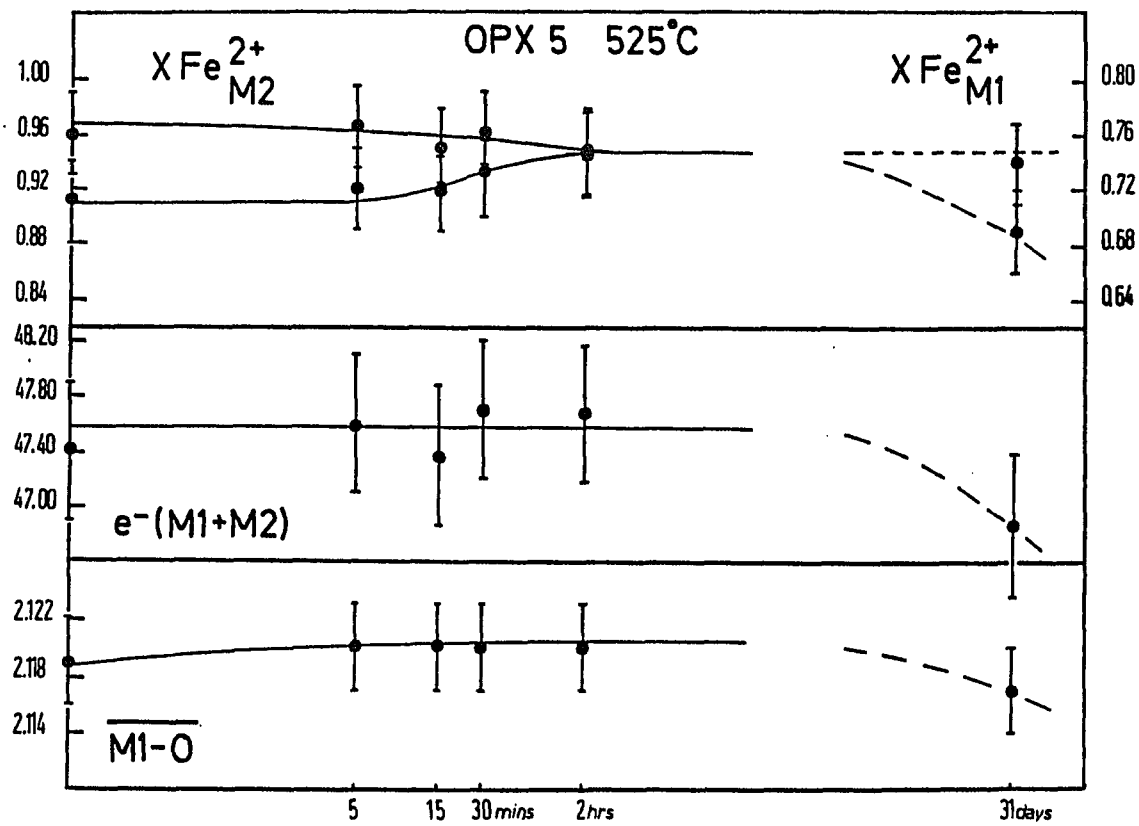

Figure 3.8d. Summary of heating experiments for sample 5 at 525°C. See caption for Figure 3.8a for other details.

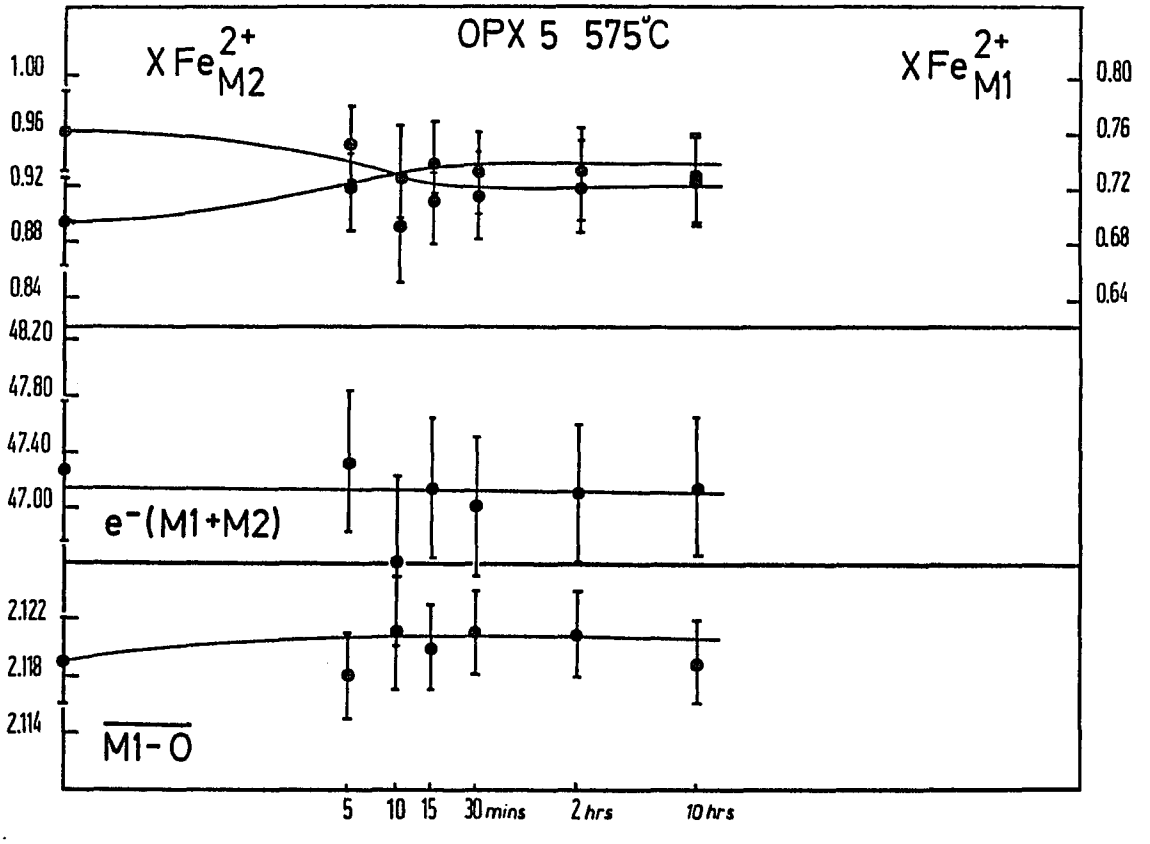

Figure 3.8e. Summary of heating experiments for sample 5 at 575°C. See caption for Figure 3.8a for other details.

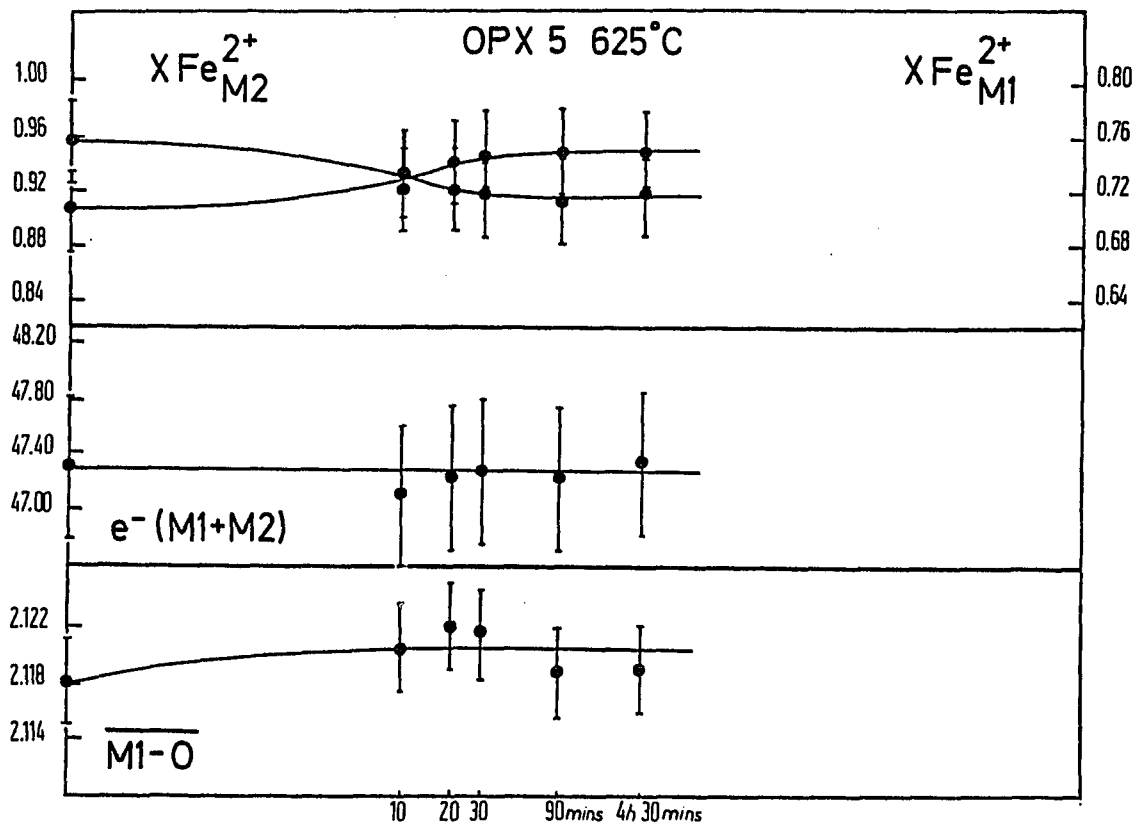

Figure 3.8f. Summary of heating experiments for sample 5 at 625°C. See caption for Figure 3.8a for other details.

2. Stability of Iron-rich Orthopyroxene

Both samples 4 and 5 showed signs of structural instabilty with heating of the crystals. This decrease in the total number of electrons with time could be attributed to a loss of iron (or other high electron density ions) from the orthopyroxene crystal structure. This may be caused by several different methods, the main ones being 1) oxidation of the sample by oxygen entering the system (which could form iron oxides on the surface), 2) a secondary iron-rich phase forming within the crystal or 3) internal oxidation in the crystal with Fe^{2+} oxidizing to Fe^{3+} which would necessitate the introduction of a vacancy into the lattice.

It should also be noted that Anovitz et al. (1988) had anomalous results for their most iron-rich sample (PX4,TM2 Fs=0.81) for long periods of heating. This sample is also out of the orthopyroxene stability field at the temperatures and pressures of their experiments. Anovitz et al. (1988), X-rayed the samples but no other phases were distinguished.

Iron-rich orthopyroxenes are stable at relatively high temperatures and pressures, normally associated with granulite facies metamorphism. The equilibrium conditions for orthopyroxene, relative to olivine and quartz, are dependent not only on pressure and temperature but also on oxygen fugacity. However, the actual value of the f_{O_2} during annealing for samples 4 and 5 is not known. The samples were heated in treated argon and the atmosphere is believed to be reducing. (The difficulty to determine the value of the fugacity also occurs for samples heated in a gas-mixing furnace as, although the gases are controlled, adequate mixing does not occur at the temperatures of these experiments (J.S.

Huebner, G.L. Nord Jr., pers. comm. 1987).) Therefore, for this section, the stability of the crystal is evaluated by observation rather than by calculation.

Initially, the stability of orthopyroxene can be studied by a phase diagram (Fig 3.9). The thermochemical data used for this diagram is from Chatterjee (1987) using an ideal solution model for the enstatite-ferrosilite binary and W12 = W21 = 4500 J/mol for the fosterite-fayalite binary. The oxygen fugacity for the experiments constraining this model (Bohlen and Boettcher, 1982) is below the QFM buffer. The phase diagram is contoured by the composition of the iron-rich pyroxene. Crystals of sample 5 are outside the stability field at one atmosphere. However, sample 4, if a pure binary phase, should be stable up to approximately 950°C. Small amounts of non-quadrilateral components may cause it to become unstable at lower temperatures.

To investigate this problem, natural and heated samples of #5 (700°C, 15 hours in air, 15 hours in argon) were studied first by SEM and then by TEM. Three crystals (100-200 μm) were first affixed to a metal stand with a carbon paste and studied under the SEM up to a magnification of 10,000X. The natural sample, figures 3.10a, b and c, shows a relatively clean surficial texture at a 200X magnification becoming, as expected, much rougher as the magnification increases to 3,700X and then 5,000X. X-ray energy dispersive spectra were collected but no unexpected concentration of elements was seen. These photographs and spectra could then be used for comparison to the heated crystals.

Figure 3.11a shows the sample heated in argon, at 10,000X. Flakes of orthopyroxene, confirmed by X-ray energy dispersive spectra,

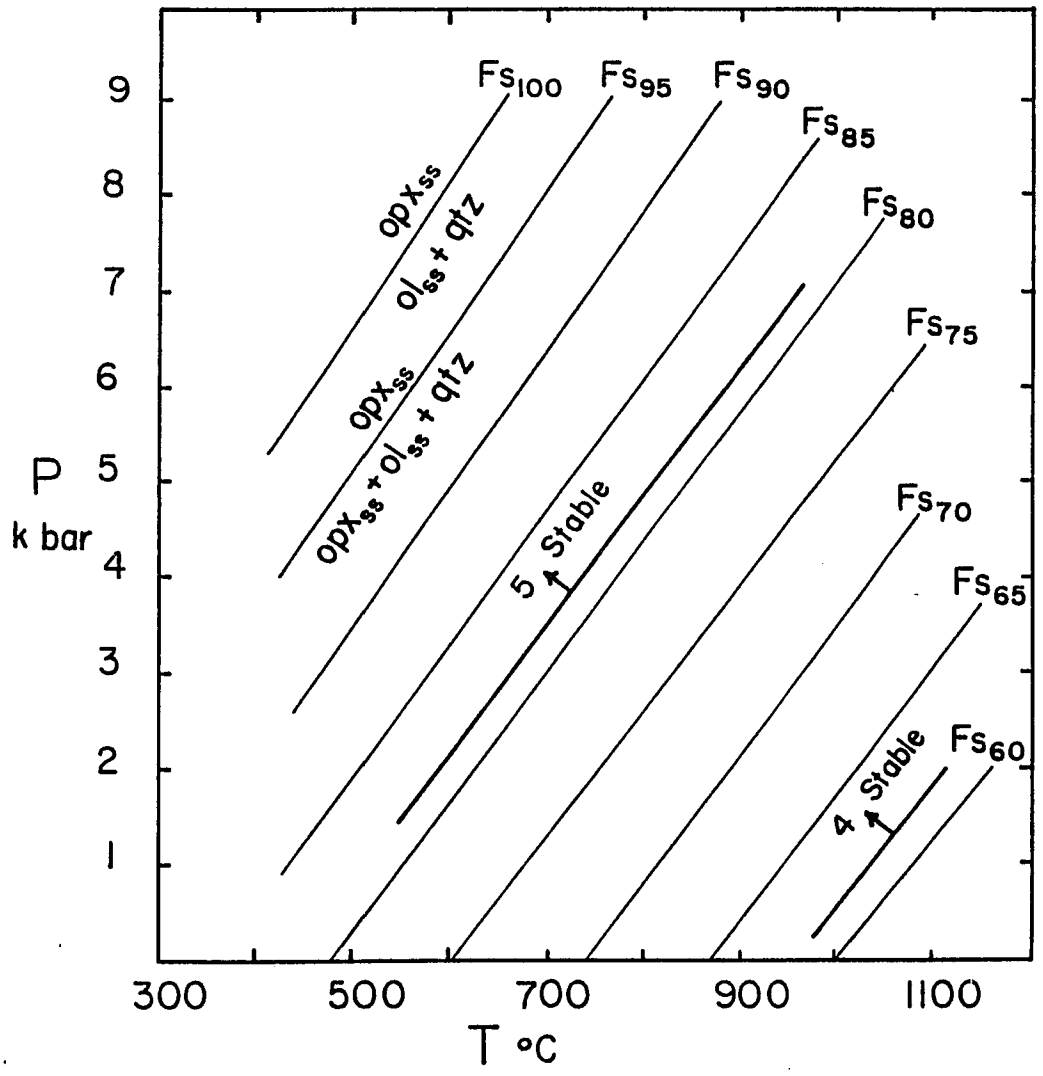

Figure 3.9. Pressure-temperature phase equilibria for olivine, orthopyroxene, and quartz, contoured in mole % ferrosilite (Fs) component Thermochemical data used and oxygen fugacity are stated in the text.

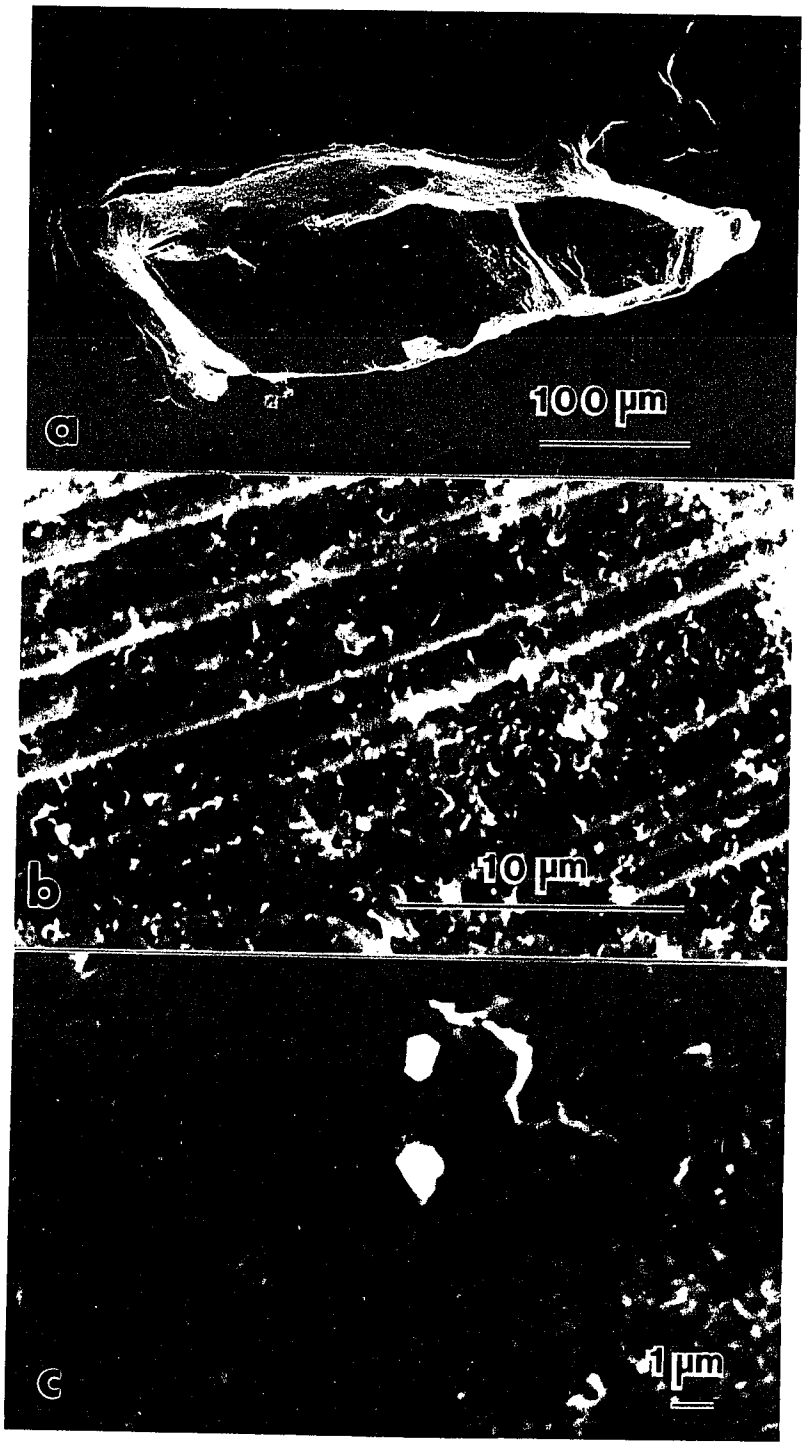

Figure 3.10. Natural (unheated) crystal of sample 5. Magnifications are (a) 200X; (b) 3,700X; (c), 5,000X.

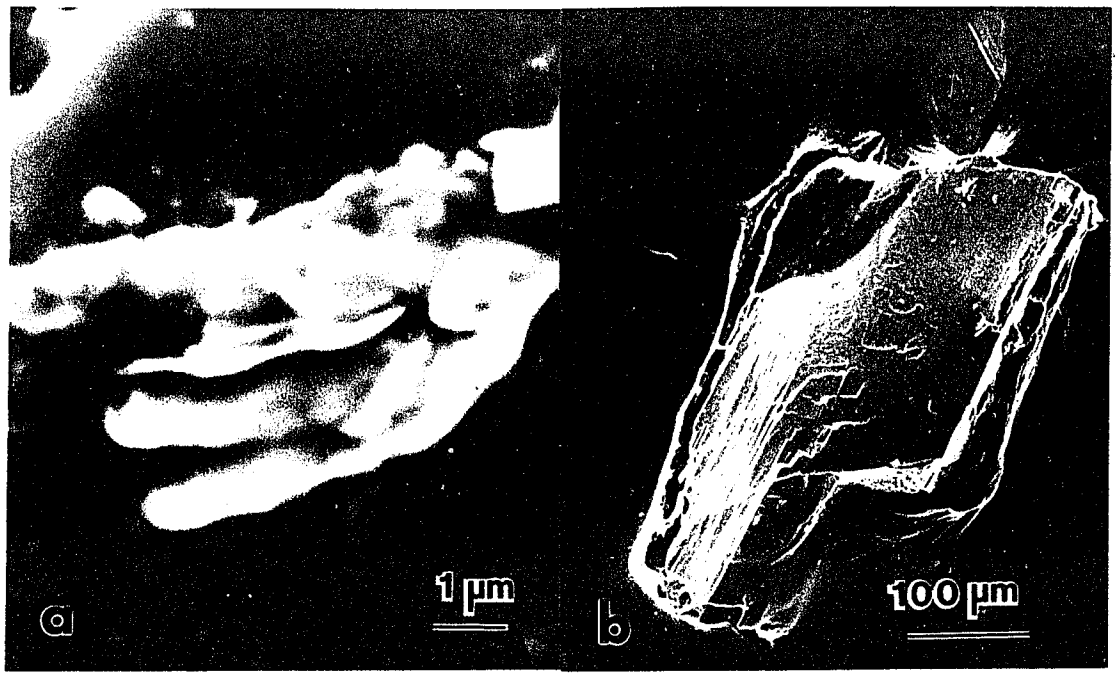

Figure 3.11. Crystal of sample 5 heated in argon (a) and in air (b). Magnifications are 10,000X for (a); 200X for (b).

could be seen. The surface was carefully checked and many spectra run on the different textural areas seen under high magnification. No secondary phase or precipitates were noted. The third sample was heated in air. The sample is shown in figure 3.10b at 200X magnification. Again no secondary phases or precipitates were seen. Therefore, oxidation of the surface due to oxygen entering the system seems unlikely.

Two crystals of sample 5, one a natural crystal and the second heated in argon, were then prepared for study with the TEM according to the preparation method of Wandless and Nord (1986). The crystal is first mounted in an epoxy "button" on a glass slide, trying to obtain an orientation perpendicular to (100). The sample is exposed by grinding and then polished with finer grits of Al_2O_3 and diamond paste. The epoxy and sample are then removed from the glass slide and reaffixed, polished side down with Crystalbond (a soluble adhesive). Again the crystal is exposed using fine grits and then slowly thinned using 9 μm and finally 1 μm diamond spray. The sample is polished to first order white or grey interference colors. The Crystalbond is then dissolved with acetone. The sample was then mounted on a copper grid using superglue and placed in an argon ion thinner and bombarded from both sides by an argon gas plasma source until a thickness of approximately 0.5 micrometers is reached. Finally the sample is coated with a thin (few tens of Angstroms) layer of carbon.

An attempt was made to thin the samples with a* and c* in the plane of the sample (*b* parallel to the beam) which is the best orientation to see features parallel to (100) in orthopyroxene. A coherent clinopyroxene lamellae is seen in figure 3.12a in an orthopyroxene

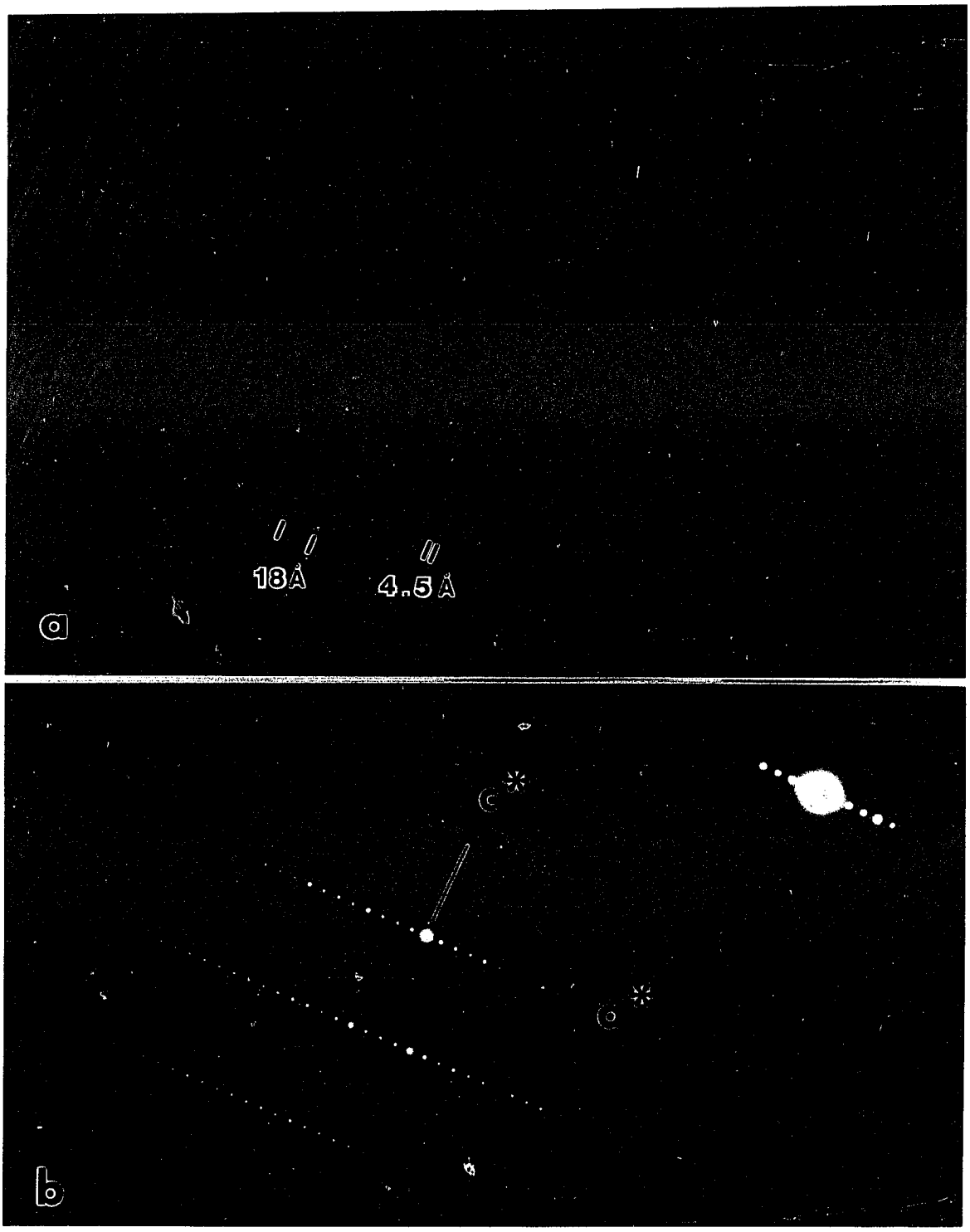

Figure 3.12a. A direct lattice image of a coherent clinopyroxene lamellae parallel to (100) in a orthopyroxene host. The diffraction pattern chosen to form this image is shown in figure 3.12b.

host. The 18 Å (100) d-spacing of the orthorhombic host can be seen, as can the 4.5 Å (200) d-spacing of a monoclinic phase, *C2/c*, clinopyroxene. Figure 3.12b shows the a* c* diffraction pattern. A small part of this diffraction pattern was chosen (inset Fig. 3.12b) to form the direct lattice image in figure 3.12a.

Figure 3.13 shows a series of photomicrographs taken across the crystal. Several fine lamellae of clinopyroxene can be seen (expected in metamorphic rocks) varying in size from 50-100 Å. The total volume of these lamellae, in this plane, is 2.7% of the crystal (direct measurement). This crystal, although checked by the microscope and considered a possible sample for the heating experiments was not studied on the diffractometer and I do not know if it would have been selected for the heating experiments. (Two out of every three were rejected after the diffraction peaks were viewed for sample #5, rejection was much higher for sample #4.) Therefore, this volume of clinopyroxene lamellae can only be considered a rough maximum for the samples used in the heating experiments.

Figure 3.14 shows the sample heated in argon. This time, unfortunately, the electron diffraction pattern indicates that b* and c* are in the plane of the sample, hence any lamellae parallel to (100) cannot be seen as they are lying in the plane of the sample. However, lamellae or precipitates other than the fine coherent *C2/c* lamellae already noted would still be seen as they would introduce strain into the crystal.

A view of this crystal can be seen in figure 3.14a. The sample is very uniform (contrast differences due to thickness changes) and no noteworthy features can be seen. Therefore, no indication of any other

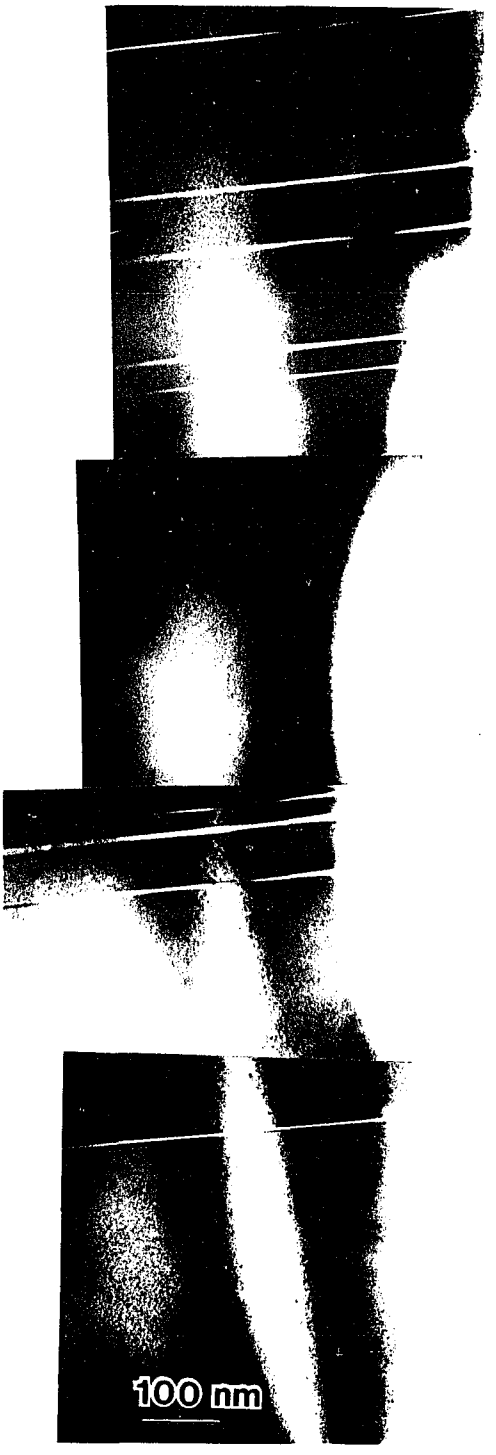

Figure 3.13. A series of photomicrographs taken across a unheated crystal of sample 5. Several fine clinopyroxene lamellae can be seen.

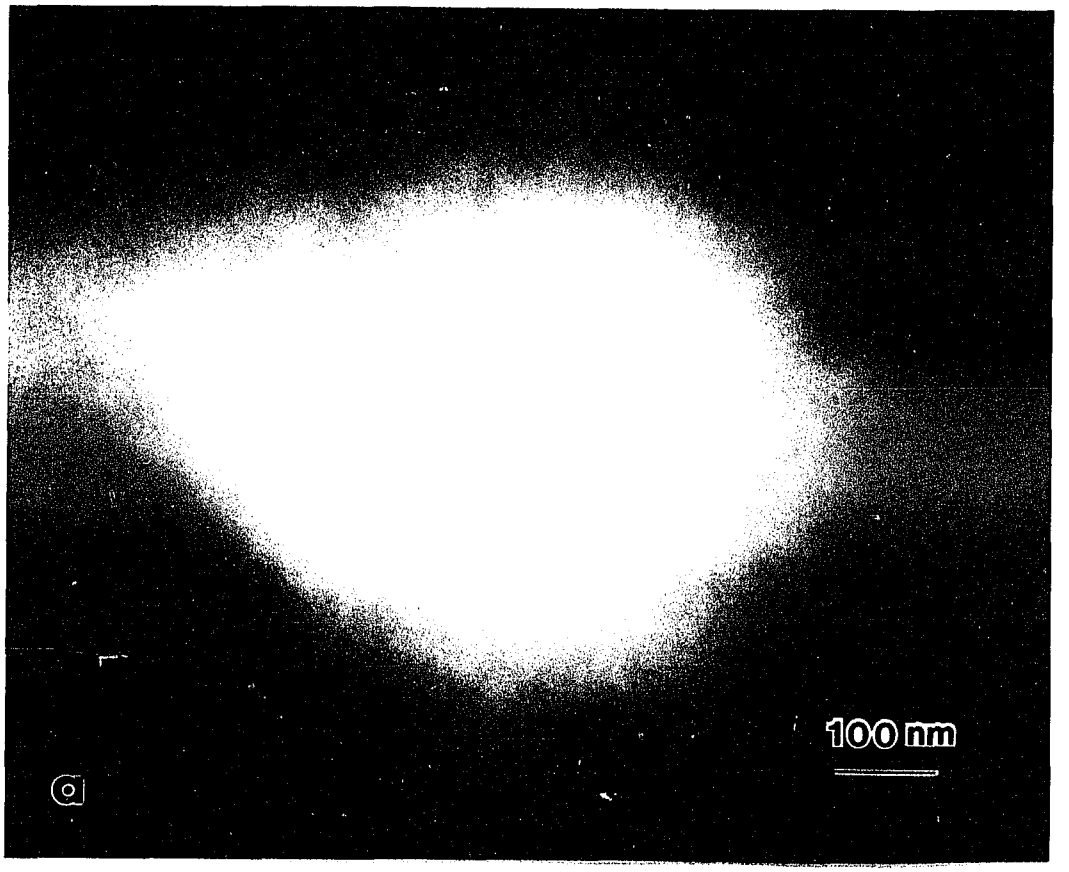

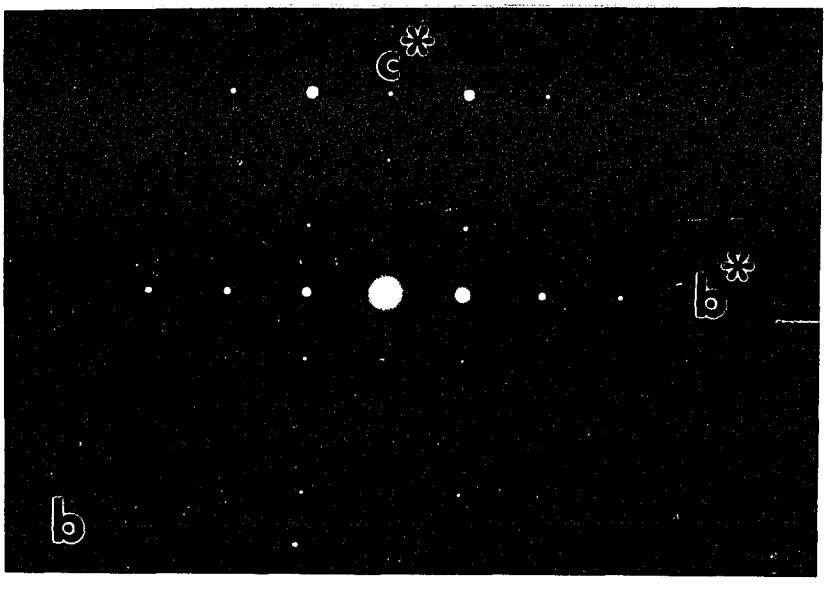

Figure 3.14a Crystal of sample 5 heated in argon showing a strain-free featureless direct lattice image. The diffraction pattern used to form the image is shown in figure 3.14b.

secondary phase could be seen and no structural distortions were noted.

From these observations, it seems that either surficial oxidation or the formation of a secondary phase are unlikely. Therefore, internal oxidation seems most probable with the introduction of a vacancy in the M2 site and the oxidation of iron in the M1 site. This would account for the decrease in electron density in M2 (seen as a loss of iron) and be consistent with a reduction in <M1-O> bond lengths whilst retaining a constant density electron in this site.

With the data available from these experiments, the exact nature of this electron loss cannot be determined. However, it is important to be aware of these problems both for future experimentation and when using previously published data in this compositional range.

3) Kinetics

a. Site Occupancy Values

The site occupancy data obtained have been used to analyze the kinetics of the disordering exchange reaction in orthopyroxene, dominated by

$$Mg^{2+}(M1) + Fe^{2+}(M2) \rightarrow Fe^{2+}(M1) + Mg^{2+}(M2) \qquad (3.b)$$

Other components in the crystal (Ca^{2+}, Cr^{3+}, Ti^{4+}, Al^{3+}) will also affect the exchange reaction. The site occupancies used for the kinetics are calculated by the program MINUIT (James and Ross, 1975). This program assigns Ca^{2+} and Mn^{2+} to M2 and Al^{VI}, Fe^{3+}, Cr^{2+} and Ti^{4+} to M1, and the cation distributions are then obtained by the minimization of the squares of the errors of the following constraints:

1) balance between atomic fractions and site electron density of both M1 and M2

2) complete site occupancy of TA, TB, M1 and M2

3) charge balance between Al^{IV} and R^{3+}

4) bulk valence balance.

It is to be noted that this method is also a good indicator of the stability of the sample as the residuals become extremely high after the electron loss begins. Cation distribution is reported in Tables 3.3.a and 3.3.b.

Table 3.3a Recalculated Site Occupancies Based on Cation Distribution, Sample 4

T°C	Time (mins)	M1						M2					FeM1	MgM1	FeM2	MgM2	K_D
		Mg^{2+}	Fe^{2+}	Fe^{3+}	Cr^{3+}	Ti^{4+}	Al^{3+}	Mg^{2+}	Fe^{2+}	Mn^{2+}	Ca^{2+}	Na^{1+}					
625	NAT	0.700	0.293	0.000	0.004	0.003	0.000	0.037	0.888	0.020	0.055	0.000	0.295	0.705	0.960	0.040	0.017
625	20	0.649	0.343	0.002	0.004	0.003	0.000	0.088	0.837	0.020	0.055	0.000	0.346	0.654	0.905	0.095	0.055
625	40	0.614	0.379	0.000	0.004	0.003	0.000	0.123	0.802	0.020	0.055	0.000	0.382	0.618	0.867	0.133	0.094
625	60	0.609	0.383	0.001	0.004	0.003	0.000	0.128	0.797	0.020	0.055	0.000	0.386	0.614	0.862	0.138	0.101
625	120	0.603	0.390	0.000	0.004	0.003	0.000	0.135	0.789	0.020	0.055	0.000	0.393	0.607	0.854	0.146	0.111
675	NAT	0.702	0.289	0.002	0.004	0.003	0.000	0.023	0.904	0.020	0.053	0.000	0.292	0.708	0.975	0.025	0.010
675	NAT	0.708	0.284	0.002	0.004	0.003	0.000	0.039	0.888	0.020	0.053	0.000	0.286	0.714	0.958	0.042	0.018
675	10	0.646	0.345	0.002	0.004	0.003	0.000	0.097	0.830	0.020	0.053	0.000	0.348	0.652	0.895	0.105	0.062
675	15	0.636	0.355	0.002	0.004	0.003	0.000	0.116	0.811	0.020	0.053	0.000	0.358	0.642	0.875	0.125	0.080
675	30	0.611	0.380	0.002	0.004	0.003	0.000	0.135	0.792	0.020	0.053	0.000	0.383	0.617	0.854	0.146	0.106
675	30	0.621	0.371	0.002	0.004	0.003	0.000	0.132	0.795	0.020	0.053	0.000	0.374	0.626	0.858	0.142	0.099
675	45	0.606	0.385	0.002	0.004	0.003	0.000	0.155	0.772	0.020	0.053	0.000	0.388	0.612	0.833	0.167	0.128
675	120	0.606	0.385	0.002	0.004	0.003	0.000	0.144	0.783	0.020	0.053	0.000	0.388	0.612	0.845	0.155	0.117
725	NAT	0.710	0.282	0.002	0.003	0.003	0.000	0.033	0.894	0.021	0.051	0.000	0.284	0.716	0.964	0.036	0.015
725	5	0.571	0.418	0.002	0.003	0.003	0.000	0.172	0.755	0.021	0.051	0.000	0.423	0.577	0.814	0.186	0.167
725	10	0.576	0.415	0.001	0.003	0.003	0.001	0.169	0.759	0.021	0.051	0.000	0.419	0.581	0.818	0.182	0.160
725	15	0.567	0.424	0.002	0.003	0.003	0.000	0.178	0.750	0.021	0.051	0.000	0.428	0.572	0.809	0.191	0.177
725	45	0.567	0.424	0.002	0.003	0.003	0.000	0.178	0.750	0.021	0.051	0.000	0.428	0.572	0.809	0.191	0.177

Table 3.3b Recalculated Site Occupancies Based on Cation Distribution, Sample 5

T°C	Time (mins)	M1						M2					FeM1	MgM1	FeM2	MgM2	K_D
		Mg^{2+}	Fe^{2+}	Fe^{3+}	Cr^{3+}	Ti^{4+}	Al^{3+}	Mg^{2+}	Fe^{2+}	Mn^{2+}	Ca^{2+}	Na^{1+}					
525	NAT	0.272	0.717	0.003	0.000	0.000	0.008	0.006	0.933	0.007	0.054	0.000	0.725	0.275	0.994	0.006	0.017
525	5	0.271	0.718	0.004	0.000	0.000	0.007	0.007	0.932	0.007	0.054	0.000	0.726	0.274	0.992	0.008	0.021
525	15	0.265	0.722	0.006	0.000	0.000	0.006	0.013	0.926	0.007	0.054	0.000	0.732	0.268	0.986	0.014	0.038
525	30	0.262	0.729	0.000	0.000	0.000	0.009	0.016	0.923	0.007	0.054	0.000	0.736	0.264	0.983	0.017	0.047
525	120	0.246	0.744	0.003	0.000	0.000	0.008	0.032	0.907	0.007	0.054	0.000	0.751	0.249	0.966	0.034	0.106
575	NAT	0.288	0.699	0.005	0.000	0.000	0.008	0.018	0.921	0.007	0.054	0.000	0.708	0.292	0.981	0.019	0.047
575	5	0.275	0.712	0.005	0.000	0.000	0.008	0.028	0.911	0.007	0.054	0.000	0.721	0.279	0.970	0.030	0.080
575	10	0.303	0.648	0.005	0.000	0.000	0.008	0.051	0.888	0.007	0.054	0.000	0.681	0.319	0.946	0.054	0.123
575	15	0.275	0.712	0.005	0.000	0.000	0.008	0.041	0.898	0.007	0.054	0.000	0.721	0.279	0.956	0.044	0.118
575	30	0.280	0.707	0.005	0.000	0.000	0.008	0.047	0.892	0.007	0.054	0.000	0.716	0.284	0.950	0.050	0.133
575	120	0.275	0.712	0.005	0.000	0.000	0.008	0.043	0.896	0.007	0.054	0.000	0.721	0.279	0.954	0.046	0.124
575	600	0.267	0.720	0.005	0.000	0.000	0.008	0.048	0.891	0.007	0.054	0.000	0.729	0.271	0.949	0.051	0.145
625	NAT	0.274	0.716	0.002	0.000	0.000	0.008	0.004	0.935	0.007	0.054	0.000	0.723	0.277	0.995	0.005	0.012
625	5	0.237	0.753	0.001	0.000	0.000	0.009	0.041	0.898	0.007	0.054	0.000	0.760	0.240	0.956	0.044	0.145
625	10	0.243	0.747	0.001	0.000	0.000	0.009	0.035	0.904	0.007	0.054	0.000	0.754	0.246	0.963	0.037	0.119
625	20	0.240	0.748	0.006	0.000	0.000	0.006	0.038	0.900	0.007	0.054	0.000	0.757	0.243	0.959	0.041	0.133
625	30	0.235	0.756	0.000	0.000	0.000	0.009	0.043	0.896	0.007	0.054	0.000	0.763	0.237	0.954	0.046	0.155
625	90	0.231	0.759	0.001	0.000	0.000	0.009	0.047	0.892	0.007	0.054	0.000	0.766	0.234	0.950	0.050	0.172
625	270	0.235	0.751	0.010	0.000	0.000	0.004	0.044	0.895	0.007	0.054	0.000	0.762	0.238	0.954	0.046	0.156

b. Theory

Mueller (1962, 1967, 1969) developed a general kinetic and thermodynamic model for site-exchange reactions, especially for quasi-binary minerals. In this summary only the binary case for pyroxene, following Mueller (1967, 1969,) will be discussed.

Following the ion-exchange reaction (3.b) for the disordering case, we can consider two atoms Fe and Mg and two non-equivalent sites M1 and M2. The change in concentration of Fe in the M2 site with time may be written as:

$$\frac{-dC^{Fe}_{M2}}{dt} = \vec{K}\phi_{M2M1} C^{Fe}_{M2} C^{Mg}_{M1} - \overleftarrow{K}\phi_{M1M2} C^{Mg}_{M2} C^{Fe}_{M1} \qquad (3.1)$$

where the C's are the molar or ionic concentrations (per cm^3), the K's are the specific rate constants in concentration units for the forward, or disordering ($\vec{K}$) and backward or ordering ($\overleftarrow{K}$) reactions (dependent especially on temperature but also pressure) and the ϕ's are analogous to activity coefficients in macroscopic systems and allow for deviations from ideal mixing on the site. Mueller, 1967 suggests that due to the consistency in environment of both species on the two sites, ϕ can be regarded as 1.

Equation (3.1) can be developed by transforming the concentrations into atomic fractions of the species (X_{Fe}) on the individual sites. This also necessitates the introduction of stoichiometric coefficients which relate the concentrations on the individual sites to the total concentration (C_o). Firstly, we can define C_{M1} and C_{M2} as the number of M1 and M2 sites in the crystal where $C_{M1} + C_{M2} = C_o$. Hence, in pyroxenes where the two sites occur in equal numbers, $C_{M1} = \frac{1}{2} C_o$ and $C_{M2} = \frac{1}{2} C_o$

and C_o can be considered as 1. As:

$$C^{Fe}_{M2} = C_{M2} X^{Fe}_{M2} \quad \text{then} \quad C^{Fe}_{M2} = \tfrac{1}{2} C_o X^{Fe}_{M2}$$

and likewise for C^{Mg}_{M1}, C^{Fe}_{M1} and C^{Mg}_{M2}

These equations can be substituted in equation 1 giving:-

$$\frac{-dX^{Fe}_{M2}}{dt} = \frac{1}{2} \left[\vec{K} \left(X^{Fe}_{M2} X^{Mg}_{M1}\right) - \overleftarrow{K} \left(X^{Fe}_{M1} X^{Mg}_{M2}\right)\right] \qquad (3.2)$$

At equilibrium, $dX^{Fe}_{M2}/dt = 0$ and so,

$$\frac{\vec{K}}{\overleftarrow{K}} = \frac{X^{Fe}_{M1} X^{Mg}_{M2}}{X^{Fe}_{M2} X^{Mg}_{M1}} = K_D \qquad (3.3)$$

Where K_D is defined by the disordering reaction (3.b)

Knowing that

$$X_{Fe} = \tfrac{1}{2} X^{Fe}_{M2} + \tfrac{1}{2} X^{Fe}_{M1} \quad \text{and} \quad X^{Mg}_{M1} = 1 - X^{Fe}_{M1} \; ; \; X^{Mg}_{M2} = 1 - X^{Fe}_{M2}$$

and substituting $\overleftarrow{K} = \vec{K} / K_D$ back into equation (3.1) we can get a quadratic in terms of X^{Fe}_{M2} and the disordering rate constant.

$$\frac{-dX^{Fe}_{M2}}{dt} = \frac{1}{2} \vec{K} \left[(1 - K_D^{-1})(X^{Fe}_{M2})^2 + (2K_D^{-1} X_{Fe} - 2X_{Fe} + K_D^{-1} + 1) X^{Fe}_{M2} - 2K_D^{-1} X_{Fe}\right] \qquad (3.4)$$

Equation 3.4 may be integrated directly for disordering under isothermal and isobaric conditions. Under these conditions $\vec{K}$, and K_D^{-1} remain constant. We can first substitute

$$a = \tfrac{1}{2}(1-K_D^{-1})$$
$$b = \tfrac{1}{2} - X_{Fe} + K_D^{-1}(X_{Fe}+\tfrac{1}{2})$$
$$c = -K_D^{-1}X_{Fe}$$

and equation (4) can be rewritten as:

$$\frac{-dX_{M2}^{Fe}}{dt} = \vec{K}\,[a(X_{M2}^{Fe})^2 + b(X_{M2}^{Fe}) + c] \qquad (3.5)$$

Integrating equation (3.5) we get

$$-\vec{K}\Delta t = \frac{1}{(b^2-4ac)^{\frac{1}{2}}} \ln \left| \frac{-(2aX_{M2}^{Fe}+ b) + (b^2- 4ac)^{\frac{1}{2}}}{(2aX_{M2}^{Fe}+ b) + (b^2- 4ac)^{\frac{1}{2}}} \right|_{X_{M2}^{Fe}(t_o)}^{X_{M2}^{Fe}(t_1)} \qquad (3.6.a)$$

for disordering and

$$-\vec{K}\Delta t = \frac{1}{(b^2-4ac)^{\frac{1}{2}}} \ln \left| \frac{+(2aX_{M2}^{Fe}+ b) - (b^2- 4ac)^{\frac{1}{2}}}{(2aX_{M2}^{Fe}+ b) + (b^2- 4ac)^{\frac{1}{2}}} \right|_{X_{M2}^{Fe}(t_o)}^{X_{M2}^{Fe}(t_1)} \qquad (3.6.b)$$

for ordering.

As Ganguly (1982) stated, the ordered state has a lower Gibbs Free

Energy than the disordered state. Therefore the specific rate constants for the disordering and ordering reactions will be different. This important fact is an integral part of equation (3.6).

These equations are valid for the disordering rate constant $\vec{K}$ obtained from experiments in this study. A different set of equations are defined below for the ordering reaction where

$$Fe^{2+}(M1) + Mg^{2+}(M2) \rightarrow Mg^{2+}(M1) + Fe^{2+}(M2) \qquad (3.c)$$

The K_D for the ordering reaction is

$$K_D = \frac{X^{Fe}_{M2} X^{Mg}_{M1}}{X^{Fe}_{M1} X^{Mg}_{M2}} \qquad (3.7)$$

The substitution, therefore, into equation 3.2 is

$$\frac{\vec{K}}{\overleftarrow{K}} = \frac{1}{K_D} \quad \text{or} \quad \overleftarrow{K} = \vec{K} \times K_D$$

Using the same conventions as for disordering, equation 3.4 can be rewritten as for the ordering rate constant as:-

$$\frac{-dX^{Fe}_{M2}}{dt} = \overleftarrow{K} [a'(X^{Fe}_{M2})^2 + b'(X^{Fe}_{M2}) + c'] \qquad (3.8)$$

but this time the constants are defined as

$$a' = \tfrac{1}{2}(K_D^{-1} - 1)$$

$$b' = \tfrac{1}{2} + X_{Fe} + K_D^{-1}(\tfrac{1}{2} - X_{Fe})$$

$$c' = - X_{Fe}$$

The equations 3.6.a and 3.6.b can then be used for the ordering case but the values of the constants are a', b', and c'.

c. Rate constants.

The rate constants defined above depend on temperature, the rate increasing at higher temperature. However, it is also true that the rate constants may be dependent on the initial composition of the sample chosen. If the starting material has a distribution of ions between the two sites that is very different to the equilibrium values, the driving force, and hence the rate of the reaction, may be very high. A sample with a starting distribution close to the equilibrium values, may have a much lower rate of change. This has been found true in alloys (Dienes, 1955) and technically, entropy, must be added to these equations.

To test this experimentally, samples of the same bulk composition, but different initial site occupancies, should be studied. This is beyond the scope of this thesis but should be considered when comparing rate constants between samples. However, the rate constants calculated are completely valid for the sample for which they were derived.

To calculate the rate constant for the site-exchange reaction, Ganguly (1982) stressed that many disequilibrium measurements must be made at a constant temperature. This study has done just that and, therefore, the calculated value of $\vec{K}$ for each sample is highly constrained.

To account for the known errors in the site occupancy data, values of $\vec{K}$ have been calculated varying both $Fe^{2+}M2$ at t_o and $Fe^{2+}M2$ at $t_{(equilb)}$ within the known error. The mean and the standard deviation are then calculated. The results are shown in Figure 3.15a for sample 4 and 3.15b for sample 5 and are listed in Table 3.4. The fit to the experimental data is good. Sample 4 did not attain equilibrium at 675°C after two hours and further runs are needed. The value of $\vec{K}$ calculated

is expected to be close to the final value as the shorter heating runs are the most important for determining $\vec{K}$ (see Fig 3.15).

Also of interest is the effect of the number of measurements at short run times. When constraining the kinetic curves, both methods are found to be extremely sensitive to the shorter runs. For sample 5, the first 5-15 minutes are critical, the first 5-60 minutes for sample 4. The value of $\vec{K}$ calculated with and without the 5 minute data point for sample 5 at 625°C are 0.29 and 0.14 respectively. Heating times less than 5 minutes have not been done as the actual heating of the crystal and the quench times become significant. This introduces other errors. Therefore, the rate calculated for these samples can only be considered as a minimum rate and the actual rate may be faster.

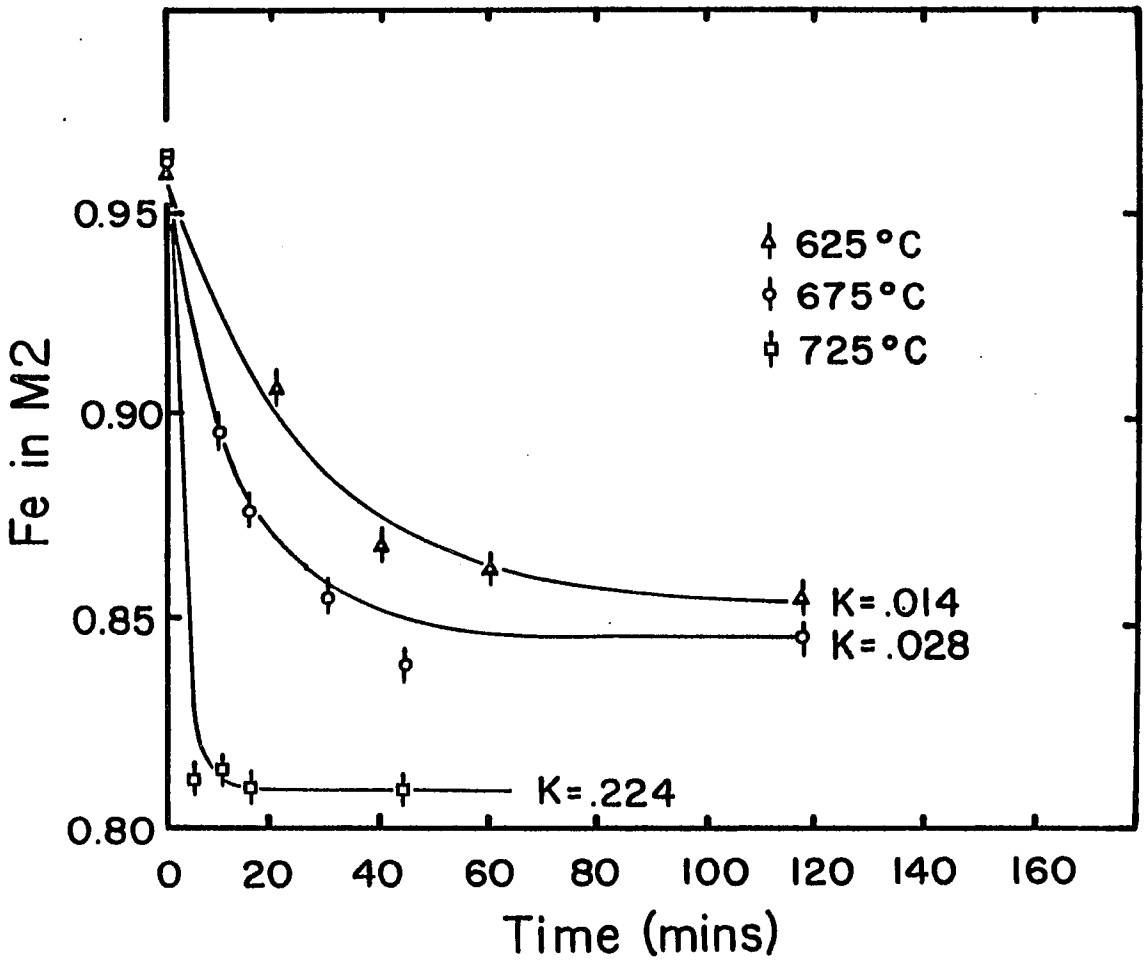

Figure 3.15a. Fitting of the rate constant, $\vec{K}$, to the recalculated site occupancy data for sample 4 (Table 3.3a). Error bars shown are one standard deviation.

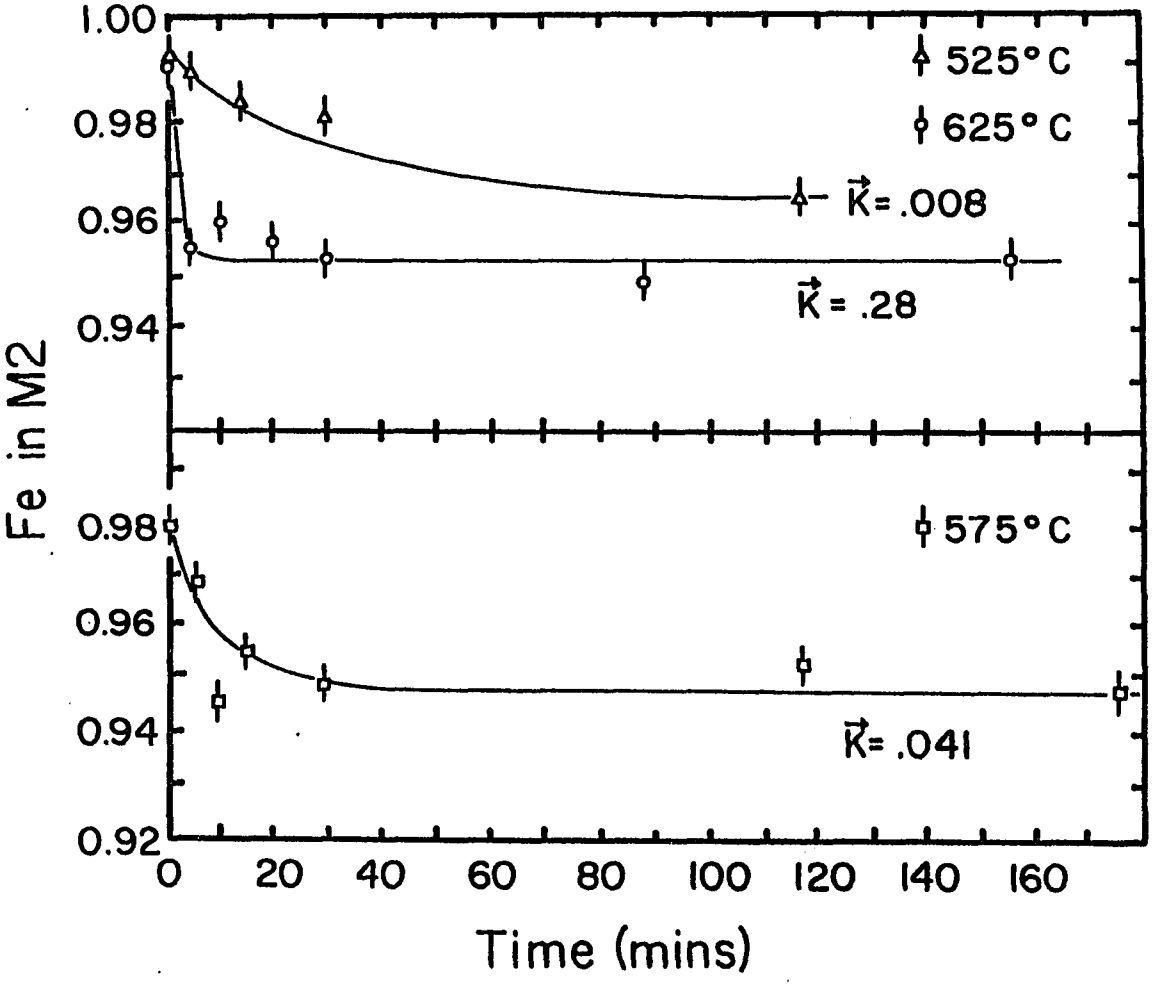

Figure 3.15b. Fitting of the rate constant, $\vec{K}$, to the recalculated site occupancy data for sample 5 (Table 3.3b). Error bars shown are one standard deviation.

TABLE 3.4 Kinetic Constants

SAMPLE	TEMP °C	$\vec{K}$ (Av)	
4	625	0.014	± .002
4	675	0.028	± .004
4	725	0.224	± .068
5	525	0.008	± .002
5	575	0.041	± .018
5	625	0.28	± .058

Average values for $\vec{K}$ per minute.
± 2 standard deviations except
sample 5 at 525 °C which is
± 1 standard deviation.

d. Activation Energies

The data on the rate constants can be used to obtain the activation energy and frequency factors for the disordering reaction. The rate ($\vec{K}$) of the reaction is related to the activation energy (Q) by the rate equation

$$\vec{K} = K^* \exp(-Q/RT) \qquad (3.c)$$

where Q = activation energy

K^* = frequency/ preexponential factor

T = absolute temperature, K

$\vec{K}$ = rate constant of reaction

R = natural gas constant

This equation can be rewritten as

$$\ln\vec{K} = \ln K^* - Q/(RT)$$

The results can then be plotted on a $\ln\vec{K}$ vs 1/T plot (an Arrhenius plot) and a straight line relationship is expected if the same reaction mechanism is operable for each determination of $\vec{K}$. The slope of the line gives the activation energy of the process (divided by RT) and the intercept gives the frequency factor.

The order-disorder reaction is thought to be the main process occurring in heated orthopyroxene crystals at low temperatures. No work has been done yet on the detailed mechanisms of diffusion processes with respect to Fe^{2+}-Mg in orthopyroxenes. However, if the exchange reaction proceeded by the same mechanism in all studies and for all compositions one would expect similar activation energies.

Experimental work on other similar mineral binaries, such as

olivine, may be applicable to orthopyroxene. Buening and Buseck (1973) studied the effects of composition, temperature, oxygen fugacity and crystallographic direction on both the Fe^{2+}-Mg interdiffusion coefficients (related to $\vec{K}$)and the activation energies for interdiffusion in olivine. They found that the interdiffusion coefficients showed a positive correlation with temperature, iron-content and oxygen fugacity. An inverse correlation is noted between Q and iron-content; increasing iron leads to a lower activation energy for the diffusion process. By analogy with olivine, a reduction of Q with increasing iron-content, and an increase in $\vec{K}$ with both increasing iron-content and temperature may be expected from the exchange of iron and magnesium for orthopyroxene.

The values for Q and K* have been calculated by the linear least-squares method (program in Appendix A). Due to the nature of the Arrhenius plot, especially when the temperatures of the experiments are constricted to a narrow range, calculated standard errors do not represent the true error because of a high correlation between Q and K* (Clifford 1973). Therefore, conditional errors have been calculated (Fig. 3.16). The conditional error of Q is calculated by keeping K* constant and varying Q within the error bars and vice-versa for the conditional errors of K*. Activation energies are 49 and 51 kcal/mole for samples 4 and 5 respectively with associated frequency factors of $8.49\ 10^{9}$ and $5.18\ 10^{11}$ (Table 3.6. p.138).

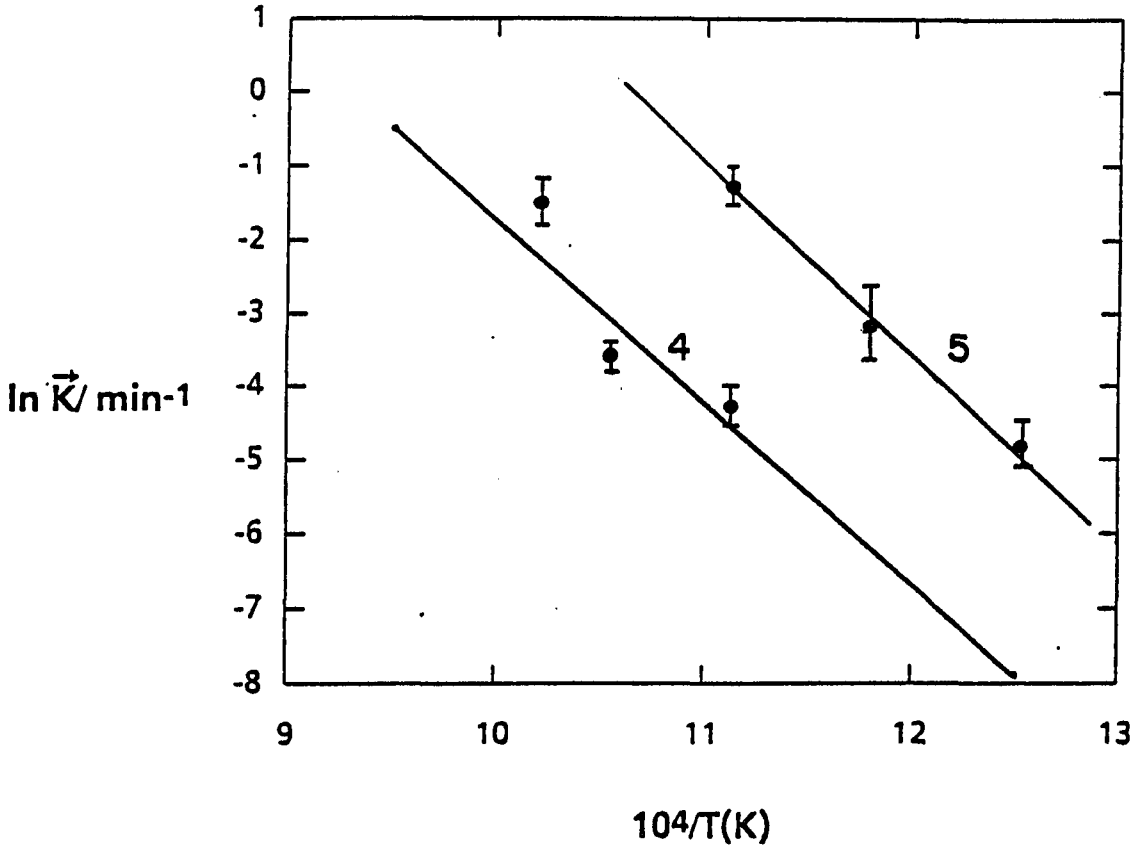

Figure 3.16. Ln$\vec{K}$ per minute plotted against $10^4/T(K)$. Solid lines indicate the least squares fit to the data points. The values of Q and K* are given in Table 3.6.

E. Comparison with other studies

This study can be compared to previous studies of the kinetic rates and the activation energy of the Fe^{2+}-Mg exchange in orthopyroxenes. The first study performed was by Virgo and Hafner (1969) on one sample (3209; Fs_{57}) using Mössbauer techniques. Besancon (1981a) studied two samples (HC; Fs_{13} and TZ; Fs_{49}) again using Mössbauer techniques. Anovitz et al. (1988) also used Mössbauer techniques to study two other samples, (M32b; Fs_{39} and Px4; Fs_{81}) and this is the only study based on ordering experiments. The other two studies (including this one) used single crystal X-ray techniques. Saxena et al. (1988) studied three samples, (274; Fs_{18}, 10; Fs_{49}, and 10/68; Fs_{77}), which complements this study of two samples 4; (Fs_{62}), and 5; (Fs_{83}).

As stated earlier, differences in the rate constants, and hence in the activation energy, may be due to the differences between the initial and equilibrium site occupancies. However, all these samples are from regionally metamorphosed areas and are expected to have initial site occupancies quite different to the equilibrium values at the experimental temperatures. It is believed that significant differences in rate constants between the samples must be due to other reasons.

Firstly, we can compare the rate constant determined in these studies. Table 3.5 shows the rate constants arranged by temperature and composition. As expected the general trends are for the rates to increase with both increasing temperature and increasing iron content. These rate constants are also shown diagramatically on Figure 3.17 (all recalculated to 650°C). A linear trend is expected when plotted on this $\ln\vec{K}$ versus composition plot if the same kinetic process is operating for all samples.

Table 3.5 Summary of All Rate Constants for Disordering $\vec{K}$ and Ordering $\overleftarrow{K}$ in Exchanges / Minute.

SAMPLE	HC[1]	274[2]	M32B*[3]	10[2]	TZ[1]	3209[5]	4[4]	10/68[2]	PX4*[3]	5[4]
Fs	0.13	0.18	0.39	0.49	0.51	0.57	0.62	0.77	0.81	0.84
	$\vec{K}$	$\vec{K}$	$\overleftarrow{K}$	$\vec{K}$	$\vec{K}$	$\vec{K}$	$\vec{K}$	$\vec{K}$	$\overleftarrow{K}$	$\vec{K}$
Temp °C										
500			7.41E-5			6E-5			3.34	
525										8.0E-3
550								2.6 E-3		
575										4.1E-2
600		1.0E-4	7.36E-3	3.0E-3	7.41E-4			1.2E-2	103.2	
625							1.4E-2			2.8E-1
650										
675							2.8E-2			
700	2.81E-3	5.0E-3	2.84E-1	4.7E-2	1.47E-2				1571	
725							2.3E-1			
750	1.18E-2				1.77E-1					
800	5.66E-2	6.0E-2	5.56		4.06E-1				14415	
1000						1E-2				

Rates calculated from Q and K values. [1]Besancon, 1981. [2]Saxena et al., 1988.
[3]Anovitz et al., 1988. [4]This study. [5]Virgo and Hafner, 1969.

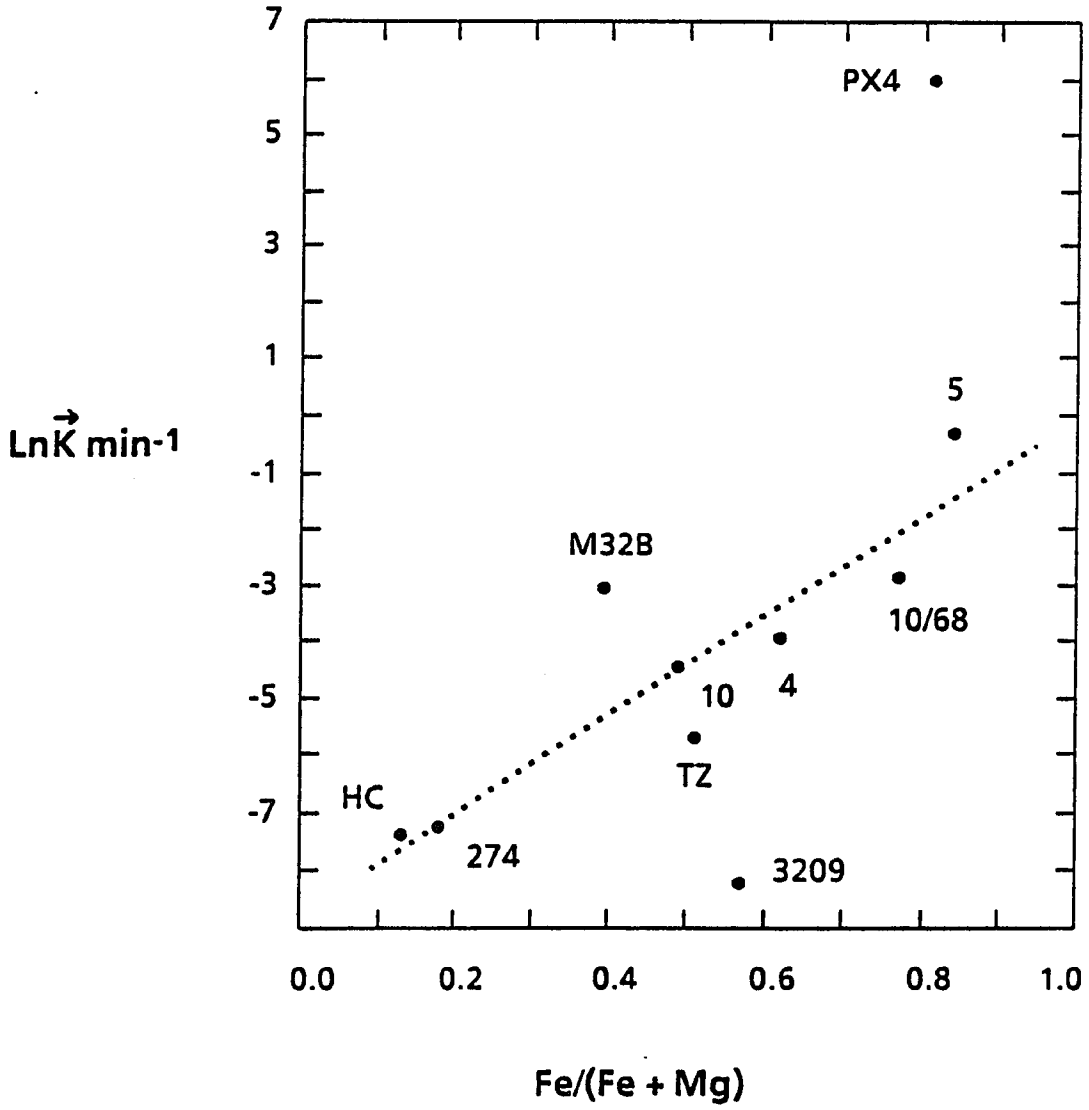

Figure 3.17. Plot of ln$\vec{K}$ against total iron content at a constant temperature of 650°C. The dotted line indicates the trend for the majority of the samples.

The rate constants for orthopyroxene sample #3209 of Virgo and Hafner (1969) are different from all the other data. As Virgo and Hafner state, their data are too sparse to analyze the kinetics in detail (three at 1000°C and 700°C, two at 800°C and only 1 at 600 °C, none with a heating period of less than 2 hours). They estimate rate constants for ordering and disordering based on site occupancies calculated using an ideal distribution model. Comparison of this sample to the experimentally derived rate constants (Table 3.5) shows that the estimated rate constant of Virgo and Hafner (1969) for 500°C is the correct order of magnitude to agree with sample 4 and sample TZ; the estimated rate at 1000°C is much too slow. This is reflected on Figure 3.17, where this sample shows an rate constant much slower than the general trend. This sample is not included in further comparisons.

Ordering rates for sample M32B and especially sample PX4 are orders of magnitude faster than the other samples. This could be explained, for sample M32B, if we return to equation (3.3) which states that $\vec{K} / \overleftarrow{K} = K_D$. The value of K_D, as defined for the disordering equation, is always significantly less than one, and this then indicates that the ordering rate constant will always be larger (or faster) than the disordering rate constant. In the ideal case, at equilibrium, K_D, (for either the ordering or the disordering reaction but defined in the same way) will be the same for both ordering and disordering experiments. However, the rate constants will still be different as they are modified by the concentration of the species on opposite sides of the equation for the ion-exchange. This does not explain the "orders of magnitude" difference for sample PX4. This sample is highly anomalous and Anovitz et al. (1988), stated that the results could not

be interpreted and did not use this sample in their calculations. However, a faster rate would be expected due to the fact that this is an ordering experiment.

Sample 5 is also faster than would be expected compared to the other samples. This may be due to the very high iron-content of this sample which could be changing the lattice structure and hence the nature of the exchange reaction (discussed later).

Activation energies as a function of composition are shown in Figure 3.18 and Table 3.6. The activation energies of the Mg-rich samples are approximately 60 kcal/mol. This includes sample M32B, for which the ordering activation energy, not the disordering activation energy, is calculated. The more Fe-rich samples show activation energies of less than 50 kcal/mol. Again the ordering sample, PX4, shows an activation energy similar to the disordering samples. Sample 10 and sample TZ show significantly different activation energies for approximately the same composition. As sample 10 is only based on two measurements, sample TZ on four, sample 10 may be in error and further experimentation should be done on this sample. However, the activation energy is in agreement with the high-iron samples. The decrease in activation energy, for orthopyroxene, with increasing iron content is consistent with that of olivine (Buening and Buseck, 1973). The trend for olivine, however, is linear and not divided into two distinct groups.

The significant change in activation energy from the Mg-rich samples to the Fe-rich samples is shown by several different site occupancy studies and two very different site defining techniques. This could be attributed to a change in process at approximately Fs 50-60.

TABLE 3.6 Summary of All the Kinetic Data for Orthopyroxene Ion-exchange

SAMPLE	Fe/(Fe+Mg)	Q (kcal/mole)	K*/minute	REFERENCE
HC	0.13	62.2	2.46 E+11	Besancon 1981a
274	0.18	59.8	1.05 E+11	Saxena et al. 1988
M32B	0.39	61.6	2.02 E+13	Anovitz et al., 1988
10	0.49	46.4	1.25 E+09	Saxena et al., 1988
TZ	0.51	60.7	1.06 E+12	Besancon et al., 1988
4	0.62	48.9	8.60 E+09	This study.
10/68	0.77	43.7	1.04 E+09	Saxena et al., 1988
PX4	0.81	45.9	3.35 E+13	Anovitz et al., 1988
5	0.84	50.6	5.18 E+11	This study.

Disordering rate constant is given by $\vec{K} = K^* \exp(-Q/RT)$

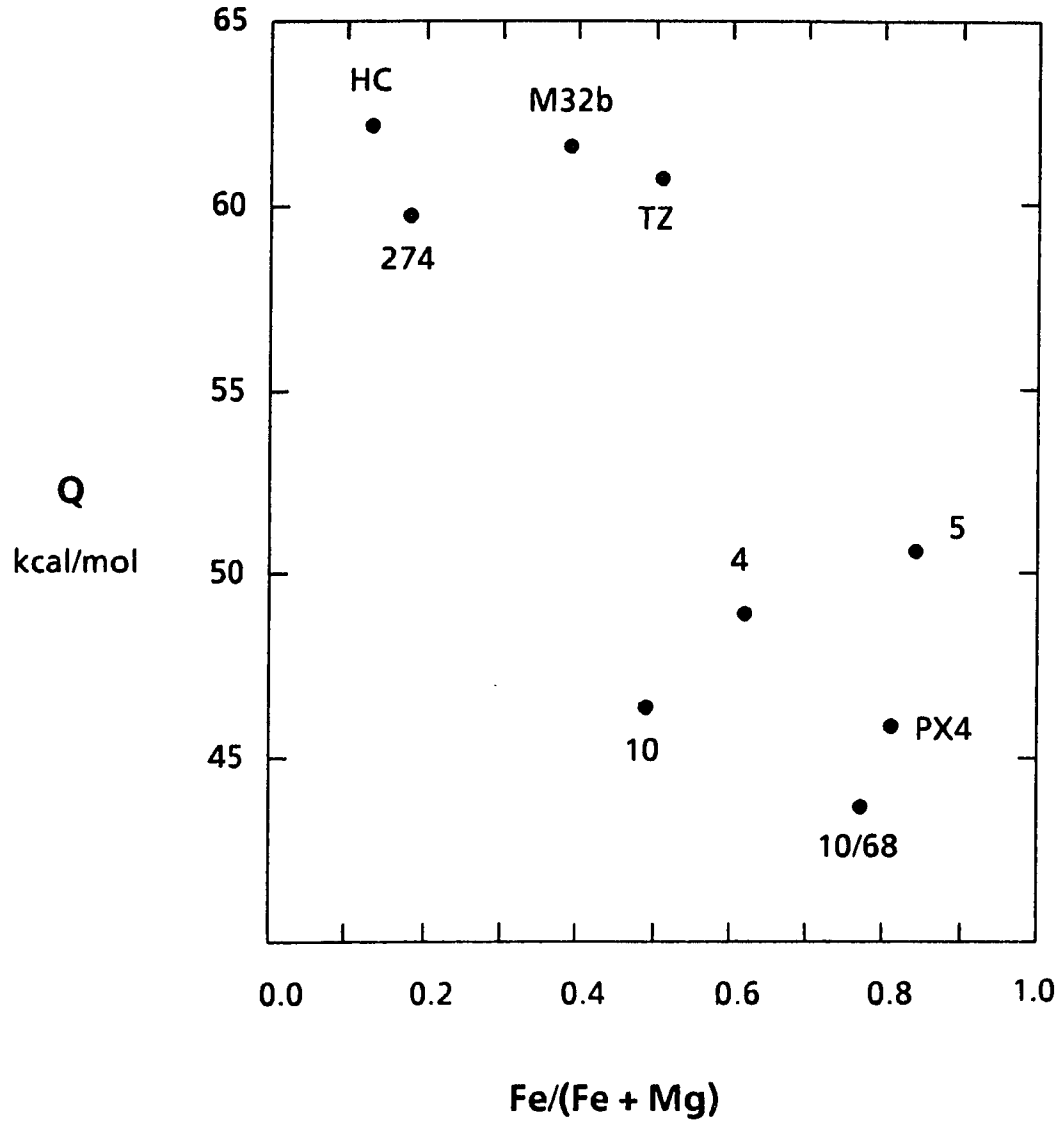

Figure 3.18. Activation energy, Q, plotted against composition. Two distinct groups can be noted with a higher and a lower activation energy. These groups may represent different diffusion mechanisms.

Several factors could affect the activation energy, such as defect density or the type of defect in the crystal. It is possible that at higher iron concentrations the amount of Fe^{3+} will increase. This will cause more vacancies in the lattice and increase the probability that a site will be available for exchange i.e. increase the entropy. This would lower the activation energy. In this composition range the M2 site is almost saturated with iron and iron begins to enter increasingly into the M1 site (Figure 3.7). This affects the lattice structure of the crystal, increasing the lengths of the M2-O3A and M2-O3B (see earlier and Domeneghetti et al., 1985). The opening up of the lattice structure could make the exchange reaction easier, again lowering the activation energy needed.

The two distinct groups for the activation energy suggests a definate change in the reactions at approximately Fs 50-60. It is interesting to note that a further, possibly connected feature has been found at this compositional range for the macro-crystals. A break in slope of the Fe^{2+}-Mg partitioning between Ca-rich and Ca-poor pyroxene has been determined (see Huebner, 1982, p 227).

Due to the differences in activation energy, two figures, both in figure 3.19, have been drafted to show the plot of $\ln\vec{K}$/min against $10^4/T(K)$. The slopes of sample HC, 274, TZ, and M32B are very similar, as expected, due to the closeness of the activation energies. The general trend, also seen for olivine, is for the samples to plot further to the right with increasing iron content. (It should be noted in these figures that extrapolation to much higher or lower temperatures will result in large errors and only the temperature range 500-800°C should be considered.) Sample M32B (ordering) plots much further to the right

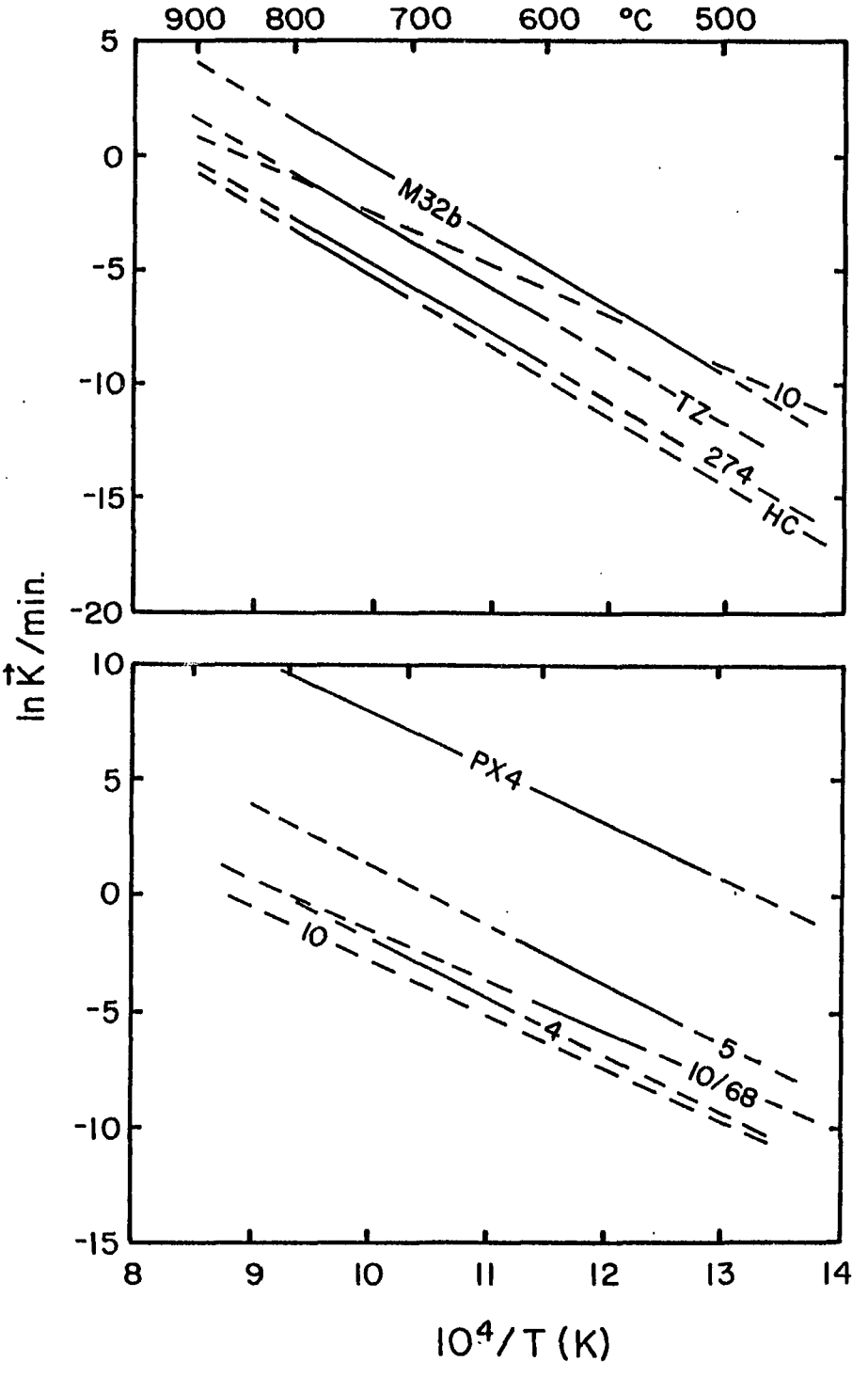

Figure 3.19. Arrhenius plot of $\ln \vec{K}$ per minute for all samples. Samples with higher activation energy (steeper slope) are plotted in the top diagram and those with lower activation energy are plotted below. Solid line indicates experimental range for each sample.

on this figure than the other samples. In Figure 3.19 the slopes are again very similar due to the activation energy, again the trend for samples 4, 10/68 and 5 is to plot to the right with increasing iron-content, and again sample PX4 (ordering) plots much further to the right than the other samples. This again emphasizes the difference in the rate constants obtained from the disordering experiments $\vec{K}$ and the ordering experiments $\overleftarrow{K}$. Sample 10 (dotted on both figures) shows a very different trend than any other sample and is probably in error as suggested before.

An indication of the dependence of K* on the actual rate constant compared to the activation energy can be seen in Table 3.7 for samples 4 and 5. These values have been calculated by changing the rate constant from seconds to minutes to years. The value of K* (the intercept) is drastically changed whereas the value of the activation energy (the slope) is constant. I believe this is shown in the relative positions of M32B and PX4 on these figures. The rate constants are higher, as shown in Table 3.5, and this is affecting the value of K* while the activation energy agrees with the other experiments.

The final comparison of these samples can be made using the Compensation Law relating the activation energy and the pre-exponential factor (see Lasaga, 1981). For a given mineral group, an increase in K* may be compensated by a corresponding increase in Q. Such a plot is shown in Figure 3.20. The relationship is expected to be linear in most cases, and again, the samples that correlated before do lie on a straight line.

Table 3.7

Sample	Q (Kcal/mol)	K*
4	49.0	4.93 E+15 / year
4	48.8	8.49 E+09 / minute
4	48.8	1.42 E+08 / second
5	50.6	2.72 E+17 / year
5	50.6	5.18 E+11 / minute
5	50.4	8.01 E+09 / second

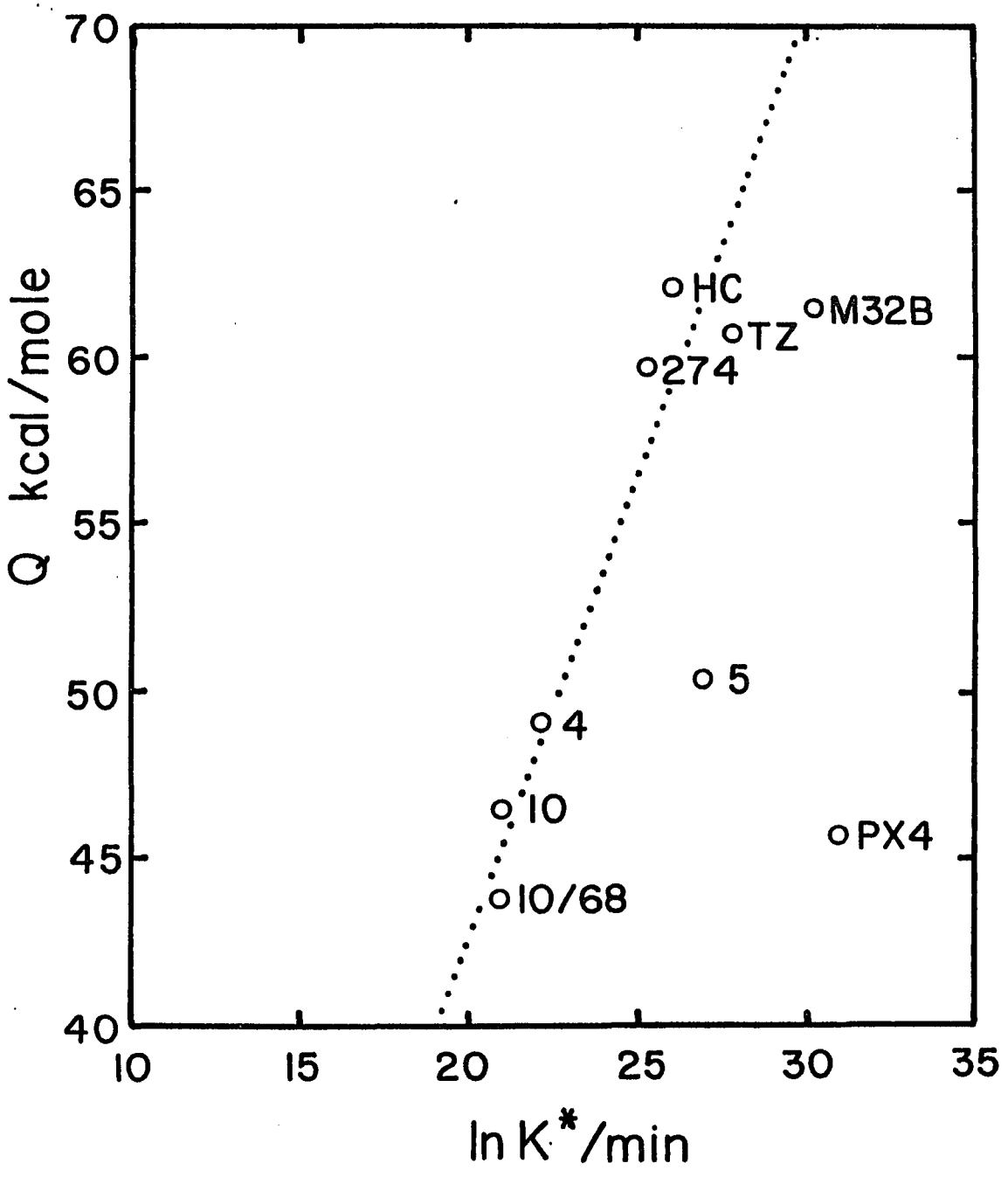

Figure 3.20. Compensation plot of activation energy, Q, against the preexponential factor, K*. The dotted line indicates the trend for the majority of the samples.

In summary, the rate constants for all studies, including samples 4 and 5, all show the expected increase with temperature and iron-enrichment. The ordering rate constants are expectedly much faster than the disordering rates. The activation energies calculated for all samples indicate that there is a large change between the more Mg-rich samples and the Fe-rich samples. The break is at approximately 50-60% Fs. This coincides with changes in the manner of site infilling and tie-line rotations between coexisting pyroxenes. The value of K* varies only slightly between the disordering samples, however, on the Arrhenius plot the samples lie progressively to the right with increasing iron; a trend also found for olivine. The values of K* for the ordered samples are very different. Finally the samples appear to follow the Compensation Law.

IV. EQUILIBRIUM SITE OCCUPANCY DATA

As explained in previous sections, we need equilibrium site occupancy data for orthopyroxene and clinopyroxene as a function of temperature and X_{Ca}. This is needed for work on kinetics of the ion-exchange reaction and for the development of a complete thermodynamic model for the pyroxene system. Much data is available on the equilibrium site occupancies of orthopyroxene; Virgo and Hafner (1969); Saxena and Ghose (1971); Khristoforov et al. (1974); Besancon (1981a); Domeneghetti et al. (1985); Anovitz et al. (1988); Saxena et al. (1988). We have very meager data on clinopyroxene equilibrium occupancies (Virgo and Hafner, 1970, McCallister et al., 1977, Dal Negro et al., 1982 and Rossi et al., 1983). The site occupancy data are also affected by pressure and concentration of other important elements but the simple system needs to be established first and therefore, the data of Saxena et al. (1988b) on Al-rich orthopyroxene and similar studies are not considered.

When attempting to evaluate the results of site occupancy studies there are several major factors that must be considered; the temperature and the duration of the experiments, whether they are ordering or disordering, and the composition of the samples. These problems are further compounded by the differences in experimental techniques (e.g. sample selection and gas mixture used for heating the sample), the differences between the Mössbauer and the X-ray refinement methods, and the problem of phase equilibria for the Fe-rich samples.

The method of single-crystal X-ray refinement has been discussed in detail in chapter III (p. 71). The Mössbauer effect is a totally different approach to obtaining the same data and the general theory and

techniques will be discussed before a comparison of the data is attempted.

A. Mössbauer Theory

The Mössbauer effect (or nuclear gamma resonance) was discovered in 1957 by R.L. Mössbauer. It is a basic resonant technique employing a photon source, an adsorber and a photon detector. The source used dominantly in geology is ^{57}Co which decays ($t_{\frac{1}{2}}$ = 270 days) by electron capture to ^{57}Fe. This atom is also in a nuclear excited state and three gamma rays (14, 123, and 137 keV) are emitted on decay to the ^{57}Fe stable ground state (Fig 4.1). Resonant adsorption is fundamental to the method. If the nuclei in the resonator (absorber or sample, in this case ^{57}Fe being paired with a source of ^{57}Co) are identical to the source nuclei the photons will be resonantly adsorbed. The resonator nuclei will themselves be excited and then will decay again with the re-emission of gamma rays to the ground state. However, although this effect is easily seen in such energy levels as the infrared region of the electromagnetic spectrum, early attempts to observe nuclear resonance were unsuccessful for several reasons. A brief outline of these problems and Mössbauer's solution follows. For a more detailed review see Bancroft (1973), May (1981), and Hawthorne (1983).

The emitted gamma-rays are not completely monoenergetic (although the spread is normally very narrow) but are distributed about a mean energy level, E_o. The distribution is Lorentzian in shape and is characterized by the mean energy level, E_o, and the full width at ½ maximum intensity or the half-width, Γ (Fig 4.2). The half-width determines the degree of sensitivity of the Mössbauer experiment.

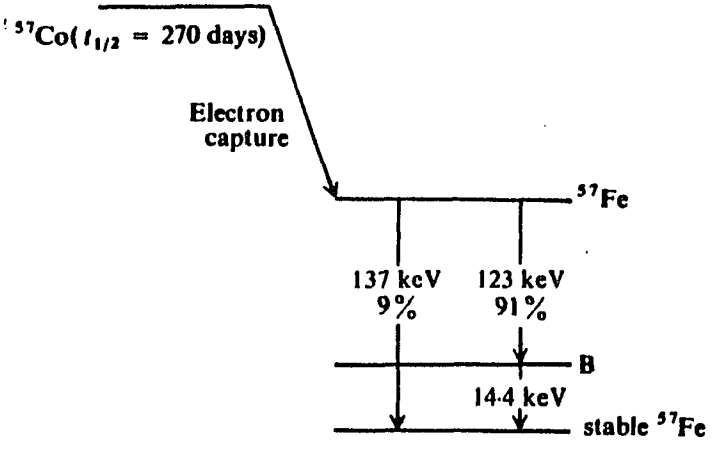

Figure 4.1. The decay of ^{57}Co to stable ^{57}Fe ground state. Three different gamma rays are emitted. From Bancroft (1973).

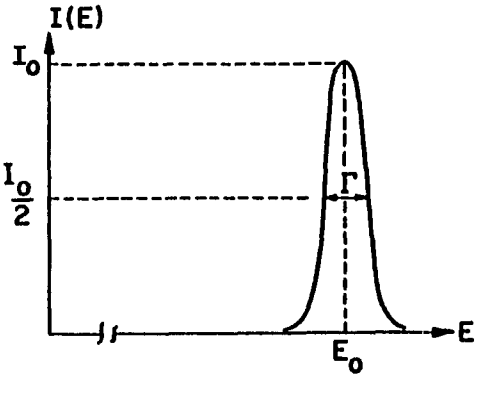

Figure 4.2. The distribution of gamma rays plotted on a figure of energy, E, against intensity, I. The Lorentzian shape is defined by the mean energy level, E_0, and the half width, Γ. From May (1971).

The decay of a radioactive substance follows the exponential law

$$N = N_0 e^{-\lambda t} \qquad (4.1)$$

where N is the number of atoms at time t, N_0 is the number of atoms at t=0 and λ is the decay constant for the particular species. At time $t = t_{1/2}$, $N = \frac{1}{2}N_0$ and $t_{1/2} = 0.693/\lambda$. The sensitivity of the experiment is also determined by the mean life $\tau = t_{1/2}/0.693$ and the Heisenberg uncertainty principle

$$\Gamma_H \tau = h / 2\pi = \hbar$$

where h = Planck's constant (6.626×10^{-34} J/sec). As 1.0 J = 6.24×10^{18}eV

$$\Gamma_H(eV) = 4.56 \times 10^{-16}/t_{1/2}$$

for the excited state β of ^{57}Fe, $t_{1/2} = 97.7 \times 10^{-9}$ sec and therefore, $\Gamma_H = 4.67 \times 10^{-9}$ eV. The line width is very small compared to the energy E_0 of 14.4keV. The sharpness of the peak $\Gamma_H/E_0 = 3.24 \times 10^{-13}$ is a very small number indicating extremely high precision.

Gamma rays are very energetic photons and the emitting atom recoils on emission (like a gun after firing a bullet). This effect can be calculated by the laws of conservation of momentum. The recoil energy loss, R, is small compared to the decay energy but it is large compared to the line width (Fig. 4.3). For resonance to occur the incident radiation must have the energy E_0, the excitation energy of the atomic or nuclear level. Due to the effects of recoil the incident gamma ray has an energy of E_0-R and cannot excite the nucleus. An initial gamma ray of E_0+R would be needed to excite the nucleus.

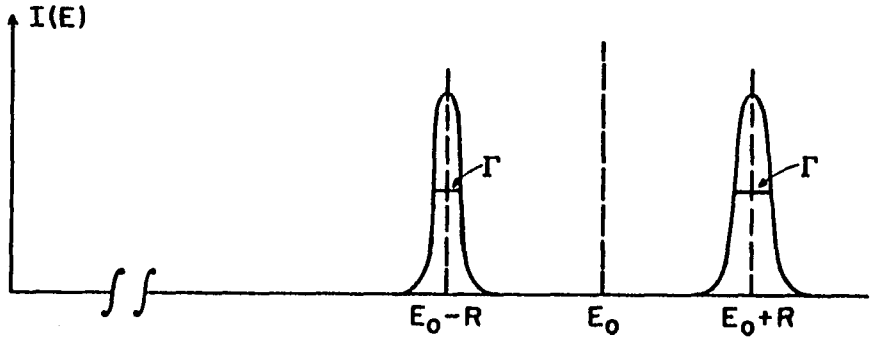

Figure 4.3 Recoil effects are seen by the loss in energy, E_0-R, for the peak on the left hand side. An initial energy of E_0+R would be needed to excite a nucleus of energy E_0. From May (1971).

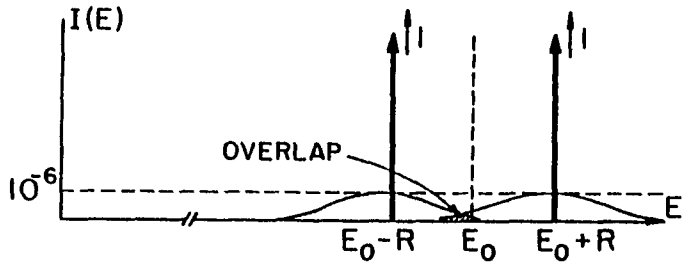

Figure 4.4. Doppler broadening leads to widening of the half width and a small area of overlap can be seen between the two peaks. Symbols as figure 3.3. From May (1971).

A further effect is that of Doppler broadening of the energy band. In any phase the nuclei are not at rest but are moving with large velocities. Doppler broadening is the effect in which apparent sound or electromagnetic frequencies are altered by motion of the emitter relative to the observer. This leads to a broadening of the half-width (Fig. 4.4). Although we now have an overlap of energies and some resonance can occur, there are very few photons and the half-width is much larger and therefore the sensitivity is lowered.

Mössbauer's discovery was that for some low energy gamma-rays the recoil energy is very low. If we consider an excited nucleus held in a rigid lattice, the emitting atom cannot recoil as R is less than the chemical binding energies. Therefore the source and adsorber energy profiles will completely overlap. This is not strictly the case as the atoms even in a solid do vibrate and the recoil energy could be transferred to the lattice. Using an Einstein model of a solid where the energy is quantized, for excitation of the lattice an energy E_E of $\pm h\nu$, $\pm 2h\nu$; $\pm 3h\nu$ is needed where v is the recoil velocity. R must be greater than E_E to excite the lattice. If $R<E_E$ the lattice cannot vibrate and R becomes minute and resonance is observed. This can be seen to occur for the different Fe isotopes

	^{57}Fe	^{56}Fe
Decay Energy	14 keV	800 keV
R	0.002eV	6eV
E_E	0.04eV	0.04eV

The 14 keV is emitted without recoil. In addition, there is no thermal

excitation of the lattice and hence there is no Doppler broadening. In the second case, the solid is excited very highly and the expected loss in energy due to recoil occurs; this causes vibrations of the atoms in the solid and Doppler broadening occurs.

In the natural case, however, some of the energy excites the solid and the energy is slightly less than E_o. The fraction that takes place without recoil is known as the Mössbauer fraction

$$f = \exp\left|\frac{-4\pi^2\langle x^2\rangle}{\lambda^2}\right|$$

An example of the Mössbauer effect can be seen if we used ^{57}Co in stainless steel as a source and ^{57}Fe in stainless steel as an adsorber. The source is then made to vibrate over a range of velocities and the number of gamma rays transmitted through the adsorber are counted. A one line spectrum will result (Fig. 4.5a). The source and the adsorber are identical. If however, a different adsorber is used one or more peaks will be observed (Fig. 4.5b). This shows that the energy levels are sensitive to the extranuclear environment.

There are two main effects on the energy levels. A change in the s-electron density at the nucleus will shift the nuclear energy levels, a phenomenon known as the Isomer Shift. This is due to both the valence state and degree of covalent bonding. Also, if the nucleus does not have a uniform charge density a quadrupole moment arises which can affect the electric field gradient (EFG) at the nucleus and can split the energy levels. This gives rise to a doublet in the energy spectrum and is known as Quadrupole Splitting. The changes in the EFG are due to the valence state and the non-spherical component of the crystal field,

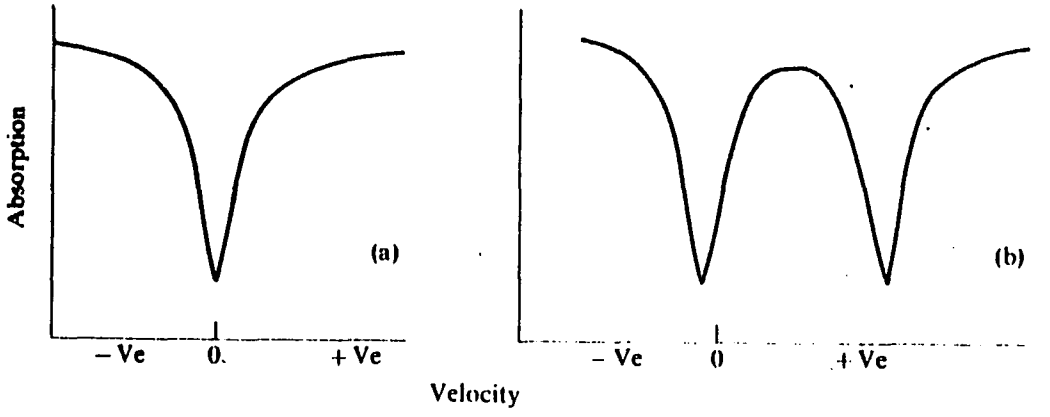

Figure 4.5a If the source and the adsorber are identical a one line spectrum will result, however, if they are different, multiple peaks will occur as in Figure 4.5b. From Bancroft (1973).

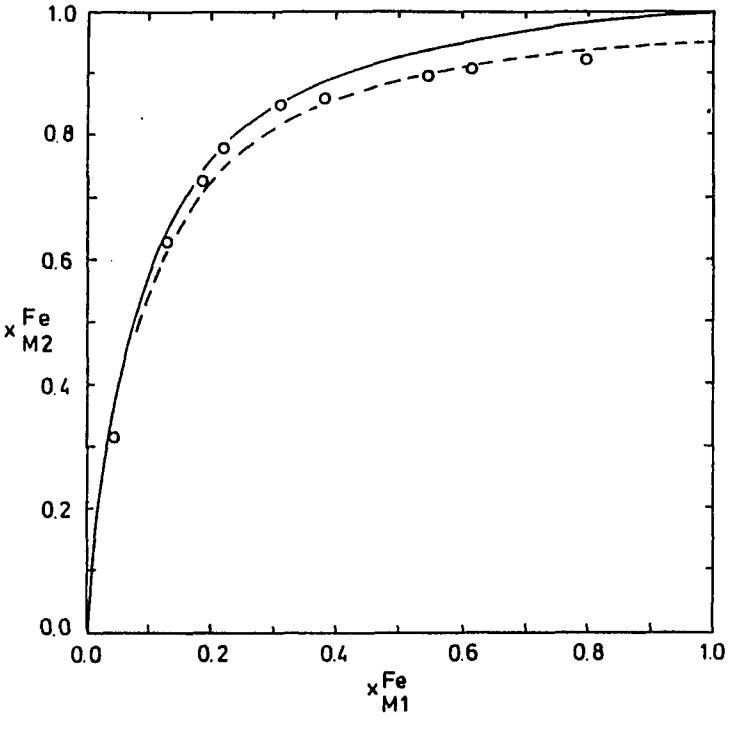

Figure 4.6 Effect of different recoiless fractions for M1 and M2 sites. The solid curve represents an ideal distribution, the dotted line the effect of varying the recoiless fractions by 10%. From Siefert (1987).

i.e. the structural environment.

Recently, Seifert (1987) has summarized some of the recent advances in the Mössbauer technique and suggested that some results need to be complemented by independent techniques. He suggests that the recoilless fraction (or Debye-Waller factor) is different for the M1 and M2 sites. In earlier studies they had been assumed to be so similar that the results would not be affected. The assumption is based on both theory and experiments on ferrosilite. In theory, we can expect Fe in M1 to be more tightly bonded than Fe in M2 (see section on bond lengths, chapter III p.82.) and recent experiments (Seifert, 1987, pers. comm.,) seem to show that the peaks are not equivalent in a ferrosilite sample. In this example he moves the K_D distribution curve from ideality to "fit" with the samples of Saxena and Ghose (1971) by varying the recoilless fractions by 10% (Fig. 4.6). He states that this is not to imply that Fe-Mg distribution in orthopyroxenes is ideal but to demonstrate the idea. Seifert (1987, oral comm.), suggested a more feasible value would be a 4% decrease in the recoiless fraction of the M2 site compared to the M1 site.

The Mössbauer determinations, therefore, probably have to be recalculated. This is especially important for the iron-rich samples. In addition, most of these earlier studies only have data on the natural and quenched sample. It is possible that there may have been a change in the crystal, as we noted, (and probably seen by Anovitz et al., 1988) which would give results with less Fe^{2+} in the M2 site.

B. Comparison of Site Occupancies for Orthopyroxene

The main factors affecting the ability of the crystal to attain equilibrium are temperature, time of heating and composition of the crystal

(1) Temperature. Kinetic studies show that samples of the same composition will react faster at higher temperatures (see Table 3.5).

(2) Duration. The length of time required to reach equilibrium. It was originally believed that a longer time was preferable to ensure equilibrium had been reached. This is probably still true for the Mg-rich samples (per. comm., Molin, Domeneghetti and Tazzoli, 1986), however, as indicated by the recent site occupancy results on Fe-rich samples (p.107, this study) a long time period enables other reactions to take place. Therefore, the changes with time for these Fe-rich samples needs to be closely monitored.

(3) Composition. This is a problem for both the magnesium-rich and the Fe-rich samples. The very Mg-rich samples are a problem for the Mössbauer method as "for magnesium-rich orthopyroxenes,...the outer doublets amount to small shoulders on the strong inner doublets and are not clearly resolvable even at 77 K, and the precision is considerably lower (than for the iron-rich)" (Ghose, 1982). For the iron-rich samples the problem is one of decomposition. Pressure, of course, stabilizes the iron-rich orthopyroxene phase.

From these observations it seems that great care must be taken when evaluating this data. The various problems and results will now be evaluated separately.

1. Mössbauer Studies

The early studies on site occupancy in orthopyroxene (Virgo and Hafner, 1969, Saxena and Ghose, 1971 and Besancon 1981a) all used Mössbauer techniques for their analyses. This has been continued by Anovitz et al., (1988) and the unpublished works of Spasato et al., (1988) and Grammenopolus (1981). More detail can be found in the respective papers.

a. Sample Preparation and Heating Conditions.

Virgo and Hafner (1969) hand picked crystals from a sieved separation of crushed rock. A purity greater than 99% is claimed. The three most iron-rich samples were heated under pressure in iron capsules. This was done to prevent decomposition to olivine and quartz or the phase transition to a monoclinic phase (see Huebner, 1982 and fig 3.9). These samples were, therefore, well within the stability field for Fe-rich orthopyroxenes. The f_{O_2} was low as they were in equilibrium with metallic iron. The other samples were sealed in quartz tubes with a vacuum of 5x10-4 mm Hg. A few of the samples were subjected to multiple runs i.e. the quartz tube was quenched, opened, some sample removed for study and then the tube resealed and heating continued. Heating times for all the runs was always less than 1 week.

Saxena and Ghose (1971) did a more systematic study over a wider range of temperatures for various compositions. A sample purity of 98% is stated, using crystals selected under a microscope. The crystals did not show zoning or any significant amount of unmixing. In addition, the crystals were examined for homogeneity by microprobe analysis. The sample was placed in an open gold capsule and heated under a freely-flowing argon pressure of 0.5-1.5 k bar. Heating times were 500°C, 3

weeks; 600°C, 2 weeks; 700°C, 1 week; 800°C, 1 week. No multiple runs were performed.

Besancon (1981a) continued with this work. The samples were crushed and separated by heavy liquids and magnets. Impurities still remained (amphiboles, clinopyroxene, magnetite, chromite, serpentine, plagioclase) which were seen optically, by electron microscope and by X-ray diffraction. It is to be noted that over 3% of these phases must be present to in order to be identified by powder X-ray diffraction (per. comm., J.S. Huebner; G.L. Nord 1986). This suggests the samples were quite impure. The samples were heated in platinum capsules with a small opening at the top. A H_2-CO_2 atmosphere was used (gas-mixture apparatus) with the proportion of CO_2 changed to keep the temperature-atmosphere conditions outside the graphite stability field. Multiple samples were loaded symmetrically into the cold furnace and brought up to temperature. After 30 minutes one sample was quenched (for initial site occupancy) and others were quenched at various times after that. The longest runs were for 70 hours.

Anovitz et al. (1988), studied two samples. The crystals of orthopyroxene were crushed and quartz and garnet inclusions were removed by magnetic separation and hand picking. In addition, the low-Fe sample was treated by oxalic acid to remove hematite staining on cleavage surfaces. The sample was further crushed to 35-100 mesh size and further hand picking was done. X-ray diffraction showed only orthopyroxene.

Runs of under 2 hours were done in a CO-CO_2 gas-mixing furnace (0.5 log units above the iron-wustite buffer). Longer runs were done in evacuated tubes with a piece of iron wire to control the oxygen

fugacity. Samples were first disordered at 900°C for two hours and then the ordering experiments were started. In addition one sample was disordered for the same time as the longest ordering experiment.

In all of these experiments the heating conditions were significantly different - especially the atmosphere used (or lack of it). Experiments on the effect of a vacuum on the kinetic rates of the experiments were done by Anovitz et al., (1988) and no significant difference was noted.

b. Mössbauer Settings, Site Occupancy Calculations and Errors.

The Mössbauer settings were fairly similar for all three groups of experiments. All used a constant acceleration velocity generator with either a 400 or 512 channel analyser. Velocity increment per channel varied from 0.04 to 0.02 mm/sec. All spectra were taken at 77 K except Anovitz et al., which were taken at 125 K. Absorbers were made by mixing orthopyroxene powder with lucite to give a concentration of between 3-5 mg Fe/cm^2. It is noted that very little information on the procedure is given by Besancon (1981a).

All authors fitted the peaks to Lorentzian curves, usually with no constraints. This method has 13 variables, 3 for each Lorentzian and 1 for the off-resonance count rate. Anovitz et al., (1988) used a maximum of 18 variables but imposed several constraints to reduce this number, including the assumption that the width of all peaks are equal. Besancon (1981a) constrained two peaks for Fe^{3+} to be equal for sample TZ. Chi squared varied between 150-300. The site occupancy was then calculated from I, the peak height and r the width at half-height as obtained from the fit to the Lorentzians which is calculated to match

the chemical data (see Saxena and Ghose, p. 539, for equation details). Mössbauer yields only a relative, not an absolute value.

Repeated spectra on different but unheated samples were conducted and errors of less than ± 0.003 for Virgo and Hafner (1969) and Besancon (1981a) and ± 1% for Saxena and Ghose (1071) were stated. Anovitz et al., (1988) give an average precision of ± 0.005 for the Fe in the M1 site and ± 0.008 for the M2 site for repeated spectra. Errors for microprobe analysis, sample impurities, and heating are not included in the data for the site occupancies. Therefore it seems that these "generous error estimates" (Besancon 1981a) are likely to be much smaller than the true errors. As sample purity is questionable, the chemical analysis error is at least ± 1 wt. percent of the various oxides and a larger overall error of ± 0.01 is suggested. This will be used in comparing the data.

2. X-ray techniques

Ganguly (1982) used the Mössbauer site occupancies to calculate cooling histories, however, he found the cooling rates to be "very sensitive to uncertainties in the site occupancy determination" and "cannot usually be relied upon when all uncertainties are considered, as anything better than "order of magnitude" numbers". He suggested further studies were needed using both Mössbauer and single-crystal X-ray techniques. Hence, work on site occupancies has been continuing (Domeneghetti et al., 1985, Saxena et al., 1988, and this study) using single crystal x-ray analysis to compare the techniques. It is also believed that errors may be lower, especially as this method can also record changes in the overall structure of the crystal reinforcing the

site occupancy data.

a. Sample Preparation and Heating Conditions

Domeneghetti et al., (1985) did the first systematic study of structural variations as a function of chemical composition and degree of ordering. All of their samples have been equilibrated at 700°C. The samples were treated in the same manner as that described on page 77. The only difference is that the gas was nitrogen at a pressure of 1 atmosphere and Fe-filings were added to absorb residual oxygen. However, the overall effect of these differing atmospheres should be very similar. Again a heat-quench cycle was performed on the same crystal but data collection finished as soon as equilibrium appeared to be reached, i.e. the experiments were not continued and so any further changes - if they would have occurred - were not seen. For details concerning the work done in this study see section III. The same procedure was used by Saxena et al. (1988).

b. X-ray Settings, Site Occupancy Calculations and Errors.

The work of Domeneghetti et al., (1985) was carried out using a Philips PW 1100 four circle diffractometer at the University of Pavia. All studies used monochromatic MoKα radiation. Structural refinements followed that described on page 77. The values obtained by this method are absolute, the exact chemical data are not part of the input data for the refinement. However, a check should be made between the site occupancy results and the chemical analysis (see Table 3.3).

The errors for this method depend essentially on the fit of the observed structural factors to the calculated ones. The differences between the samples and sample purity errors can be eliminated as only one single, carefully selected crystal is used. Repeated heatings of the

same crystal remove absorption problems. For sample #4 repeated heatings have been performed for several differing durations and the fit is well within the error (see Fig. 3.8). Again, an error value of 0.01 is suggested. This is three times the estimated standard deviation of the site occupancy and is believed to be a highly realistic error.

3. Comparison of the Site Occupancy Data

The Mössbauer data have been well summarized by Anovitz et al., 1988 and are shown in figure 4.7. The points shown are for the original site occupancy and the direction of movement. They include both ordering and disordering experiments. As stated by Anovitz et al., (1988) the experiments on solely disordering or ordering can only be regarded as half reversals. This is especially true of the earlier studies when only an initial (natural) site occupancy and a final (or equilibrium) site occupancy are known. The later studies, where the change with time is well monitored and several points confirm the equilibrium value, this is less of a problem but should still be taken into account.The results have been fitted to the equation

$$RT\ln K_D = RT\ln K + W^{M1}(1-2X^{M1}_{Fe}) - W^{M2}(1-2X^{M2}_{Fe})$$

For Anovitz et al., (1988) this results in the data

$$\ln K = 1203/T(K) + 0.1272$$

$$W^{M1} = 5449 \text{ J/mol}$$

$$W^{M2} = 2083 \text{ J/mol}$$

and this is shown as the solid curve Figure 4.7. The values obtained by Ganguly, 1982 are:-

$$\ln K = -1562/T(K) + 0.1435$$

$$W^{M1} = 6377 \text{ J/mol}$$

$$W^{M2} = 4519 \text{ J/mol}$$

and is shown by the dashed curve (Fig 4.7). The difference in sign for the lnK value is due to Anovitz et al., (1988) defining K_D for the ordering reaction whilst Ganguly (1982) defines K_D for the disordering reaction. Onto these curves I have added the data from the single X-ray analysis of this study and those of Saxena et al, 1988 (Fig. 4.8).

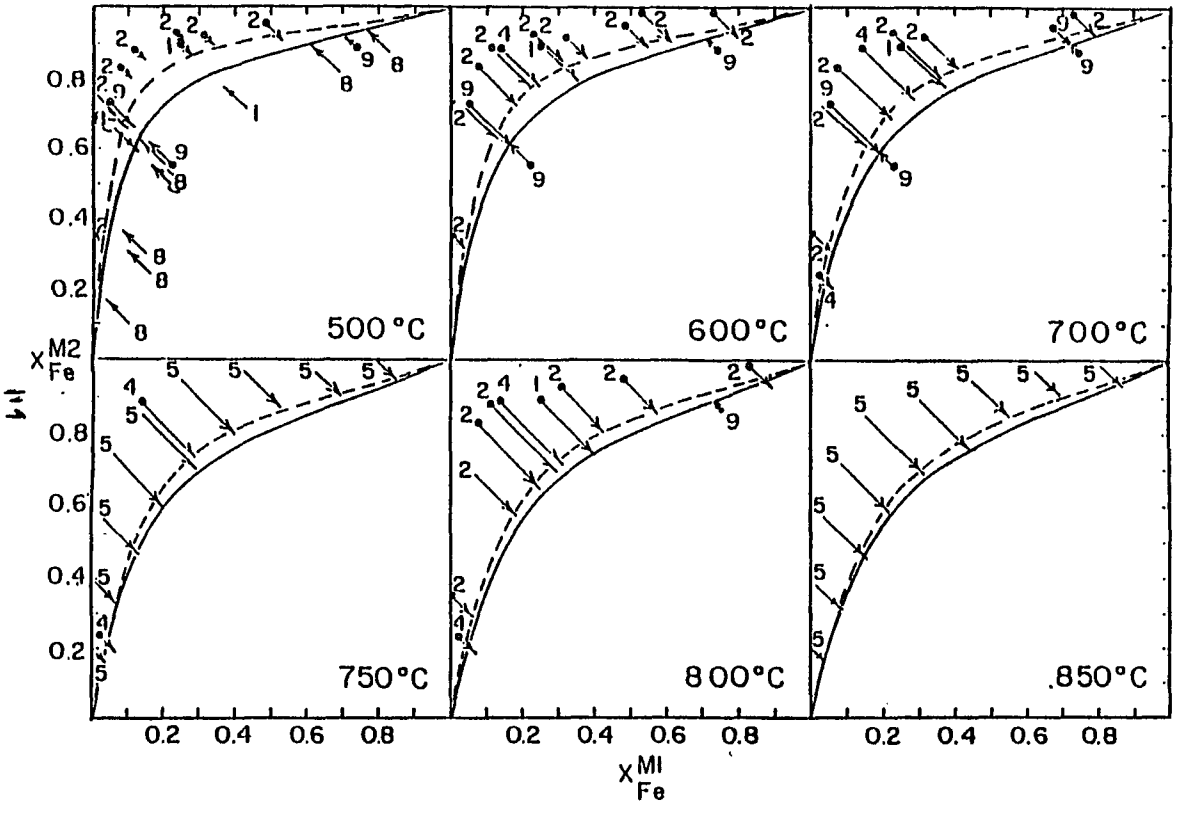

Figure 4.7. Results of the equilibrium site occupancies for orthopyroxene obtained experimentally by Mössbauer. From Anovitz et al. (1988). The numbers are 1) Virgo and Hafner (1969); 2) Saxena and Ghose (1971); 4) Besancon (1981a); 5) Grammenopoulou (1981); 6) Khristoforov et al. (1974); 8) Besancon, Sposato and Grover (in Anovitz et al.,1988); 9) Anovitz et al. (1988). The starting values are shown as dots, the equilibrium values by the tip of the arrow. The models indicated are Ganguly (1982), dashed lines, and Anovitz et al. (1988), solid lines.

The samples in this study were heated at 525, 575, 625, 675, and 725 °C, therefore, they can not be expected to lie on the actual isotherms but to straddle the 600 and 700°C isotherms and to plot on the more disordered side of the 500°C isotherm. However, all the data points plot to the more ordered side of the curve of Anovitz et al., 1988. It is highly unlikely that the higher temperature experiment of both of these pairs did not attain a more disordered value than the lower temperature isotherm.

However, if the recoilless fraction was different between the M1 and M2 site as suggested by Seifert (1987), the difference between the two techniques could be accounted for. The new isotherms are calculated by increasing the value Fe^{2+} in the M2 site by 4% and readjusting both values to the original bulk composition. The resulting values for the above equation are:-

$\ln K = 1208/T(K) + 0.2545$

$W^{M1} = 4303$ J/mol

$W^{M2} = 3179$ J/mol

The effect of changing the values is shown at 600 and 700°C on figure 4.8, Also shown are the original curves of Anovitz et al., 1988. This calculation only affects the more Fe-rich compositions significantly.

The resulting curves on figure 4.8 are then the least-squares fit to all the Mössbauer data assuming the recoilless fraction is different for the two sites. The X-ray data from this study corresponds quite well to these adjusted isotherms, especially for the 700°C curve. The data from Saxena et al. (1988) all lie to the more disordered side of the isotherms suggesting further heating is still needed to attain equilibrium.

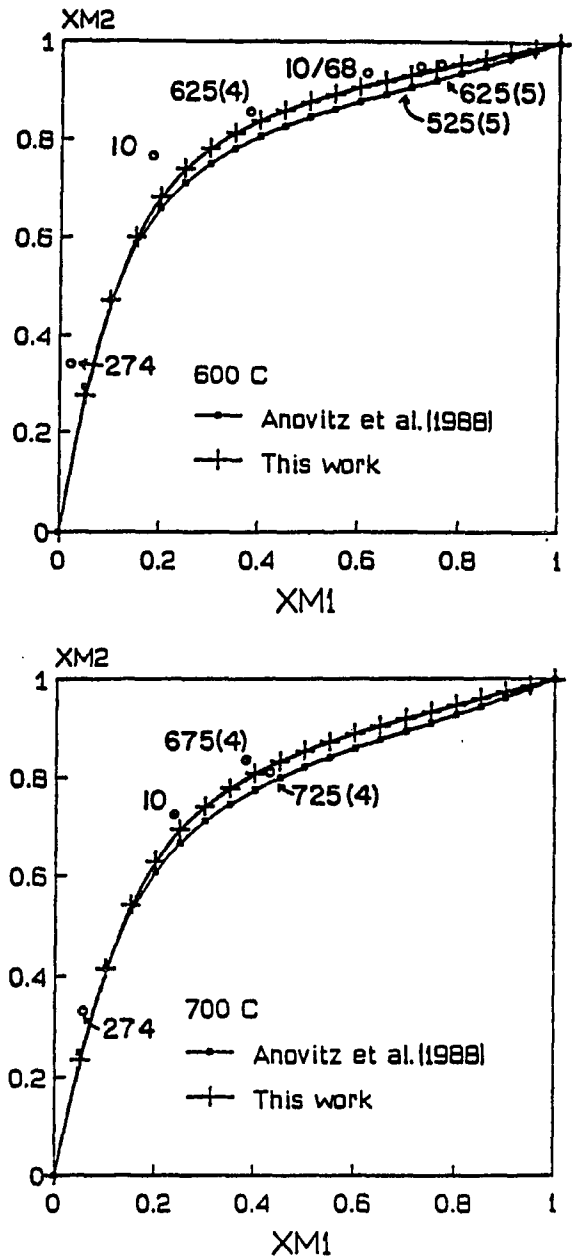

Figure 4.8. Equilibrium site occupancies for X-ray diffraction studies shown with respect to the model of Anovitz et al. (1988) and the adjusted model (this work). Samples 274, 10 and 10/68 from Saxena et al. (1988) are for 600 and 700°C on the corresponding isotherm. Samples 4 and 5 from this study have the temperature indicated.

V. MACROSCOPIC-MICROSCOPIC MODEL

Solutions to some petrogenetic problems pertaining to the formation and evolution of the earth's crust and mantle will be aided by the completion of a pyroxene-geothermometer that includes both thermodynamic and site occupancy data. The compositional sensitivity of such a thermometer is likely to lead to a more complete and probably more interesting interpretation of the thermal history.

Models comparing macroscopic and microscopic parameters are currently being developed see Thompson (1970); Sack (1980); Davidson et al. (1982); Saxena (1983a); Davidson (1985); and Davidson and Lindsley (1985). These workers used convergent and non-convergent site-disorder models for pyroxenes and their work clearly demonstrates the importance of site occupancy studies.

The site occupancy data provide a means to interpret the pyroxene equilibrium compositions, and complete the work on quadrilateral pyroxene geothermometry. Such a study is an integral part of the phase equilibrium studies on pyroxenes being conducted by others. Note that the experimental study of Fe-Mg order-disorder in pyroxenes is crucial in the interpretation of phase equilibrium data irrespective of whether the theory as discussed here for a totally macroscopic approach is used or another model for the site-activity-composition model is preferred.

A. Theory

The theory connecting the macroscopic parameters (chapter II, p.9) to the site occupancy data is developed here to show the interaction between the two parameters. This description essentially follows that of Putnis and McConnell (1980).

For every solid solution, the microscopic features of the crystal such as the shape and size of the individual sites change with composition. This also varies with the type of site and the cations that occupy them. For a solid solution we can again consider the changes in enthalpy and entropy on mixing. The free energy change on mixing is defined as

$$Gmix = Hmix - TSmix \qquad (5.1)$$

Considering this on a microscopic scale, we can consider two atoms A and B mixing in a solid and can count the number of sites occupied by each atom. The crystal consists of N atoms, where Na is the number of atoms of A and Nb is the number of atoms of B.

Considering first the entropy term. The number of ways in which Na and Nb atoms can be arranged over N sites is a measure of the configurational entropy of mixing (ΔS).

$$\text{Number of arrangements} = \frac{N!}{(Na)!(Nb)!} \qquad (5.2)\ (5.2)$$

from the second law of thermodynamics we have

$$\text{Configurational energy } (\Delta S) = k\log_e \omega = k\log_e \frac{N!}{(Na)!\ (Nb)!} \qquad (5.3)$$

simplified by using $\log_e N! = N \log_e N - N$

$$\text{Configurational energy } (\Delta S) = -Nk(a\log_e a + b\log_e b) \qquad (5.4)$$

If we take a mole of atomic sites, R = Nk = 1.987 cal/mol and equation 5.4 becomes

$$(\Delta S) = -R\ (a\log_e a + b\log_e b) \qquad (5.5)$$

As a and b are fractions, (ΔS) is positive and hence, the term -TS is always negative.

Next consider the change in the enthalpy. This can be assumed to be dependent on the interaction between the nearest neighbour pairs. There are three models for the interaction energies V_{AA}, an A-A bond, V_{BB}, a B-B bond and V_{AB}, an A-B bond. To evaluate the internal energy we need to know the total number of each type of bond, which involves knowing the amount of A and B present and the number of nearest neighbours around each atom.

The total energy can be summarized as

$$\text{Total energy} = \frac{ZN}{2}\ [aV_{AA} + bV_{BB} + ab(2V_{AB} - V_{AA} - V_{BB})] \qquad (5.7)$$

see Putnis and McConnell (1980) for further details. As the first two terms are the energies of the pure end members before mixing, the third term determines whether the energy on mixing is higher or lower than the mechanical mixture.

There are three possibilities; that similar atoms will be attracted to each other; that disimilar atoms will be attracted to each other; and that both types are attracted equally to each other. The first example is when $2V_{AB} > V_{AA} + V_{BB}$. This case occurs when the internal energy of

the solution is raised by replacing A-A and B-B bonds with A-B bonds. Therefore, H_{mix} is positive and the solution will tend to unmix. The second case is the opposite, with $2V_{AB} < V_{AA} + V_{BB}$. This indicates a tendency for the formation of a compound with the maximum number of A-B bonds. In this case H_{mix} is negative and the solution will tend to mix. The final case occurs when $2V_{AB}=V_{AA} + V_{BB}$. In this case the H_{mix} = 0 and the solution is said to be ideal. For this to occur the two atoms must be similar in their volume and forces and hence the structural framework will remain essentially unchanged. These three cases can be seen graphically in Fig 5.1.

It is to be noted that even in the case where H_{mix} is positive the Gibbs Free Energy of mixing is dominated by the negative entropy term for a weak solution. This indicates that for these compositions the tendency is towards mixing and this explains why pure end members are rarely found in nature. A small amount of impurity will lower the free energy of the crystal.

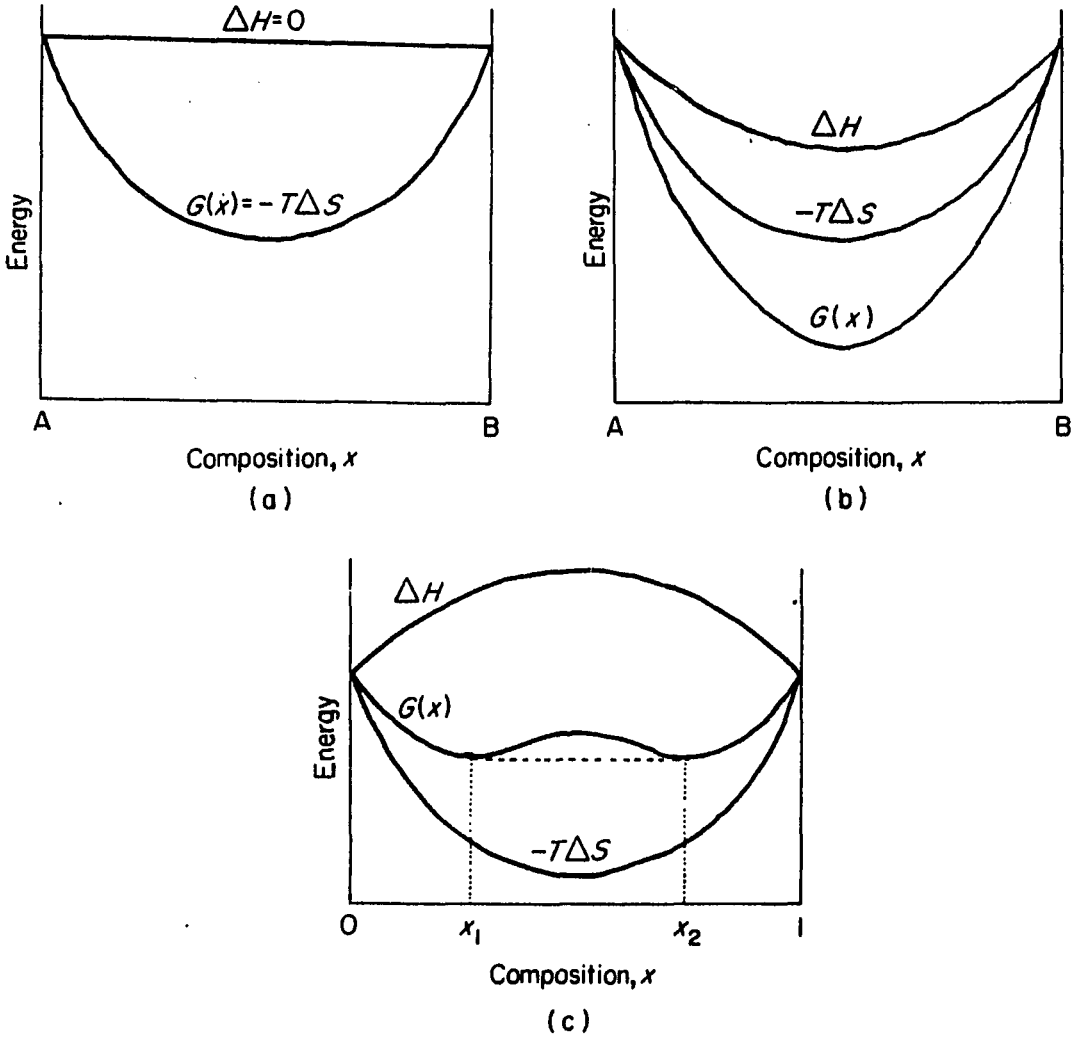

Figure 5.1. Curves for ΔH, -TΔS and G(x) as a function of composition in three different cases: (a) when $2V_{AB} = V_{AA} + V_{BB}$, i.e. $\Delta H = 0$; (b) when $2V_{AB} < V_{AA} + V_{BB}$, i.e. $\Delta H < 0$; (c) when $2V_{AB} > V_{AA} + V_{BB}$, i.e. $\Delta H > 0$. From Putnis and McConnell (1980).

B. Method of Calculation and Data

To model the pyroxene quadrilateral theoretically, from a macroscopic viewpoint, we need information on the activation energy and energies of the individual sites for the site exchange reactions (see Thompson, 1970; Sack, 1980; Saxena, 1983a; Davidson, 1985; and Davidson and Lindsley, 1985). As noted in section IV, however, the site occupancy data currently available are not without problems and, therefore, the resulting models are not highly constrained.

In this section, therefore, we have attempted a different approach to this problem. We have recalculated the site occupancy data on a pyroxene crystal and expressed it in terms of five end-members, enstatite, diopside, hedenbergite, ferrosilite and ordered hypersthene (all Fe in M2, all Mg in M1) (Figure 5.2 and Table 5.1). The ordered hypersthene is needed to completely express the site occupancy. The model is very similar to that developed in chapter II apart from the additional component.

Enthalpy, entropy and specific heat data are available for all end members (see Table 2.2) but ordered ortho- or clino-hypersthene. These two new end members can be estimated as we know the thermochemical data for the end members, enstatite and ferrosilite, and also the thermochemical data for the binary solution. These values, once obtained, are not considered fixed but can vary slightly in the model. In addition we already calculated the binary solutions for most of the model (Table 2.3) except those for ortho- or clino-hyperthene (5). The W_{ij} needed are W_{15}, W_{51}, W_{25}, W_{52}, W_{35}, W_{53}, W_{45}, and W_{54}. Again these are partly constrained. We can expect exsolution for the binary solutions with either diopside (2) or hedenbergite (4) as an endmember.

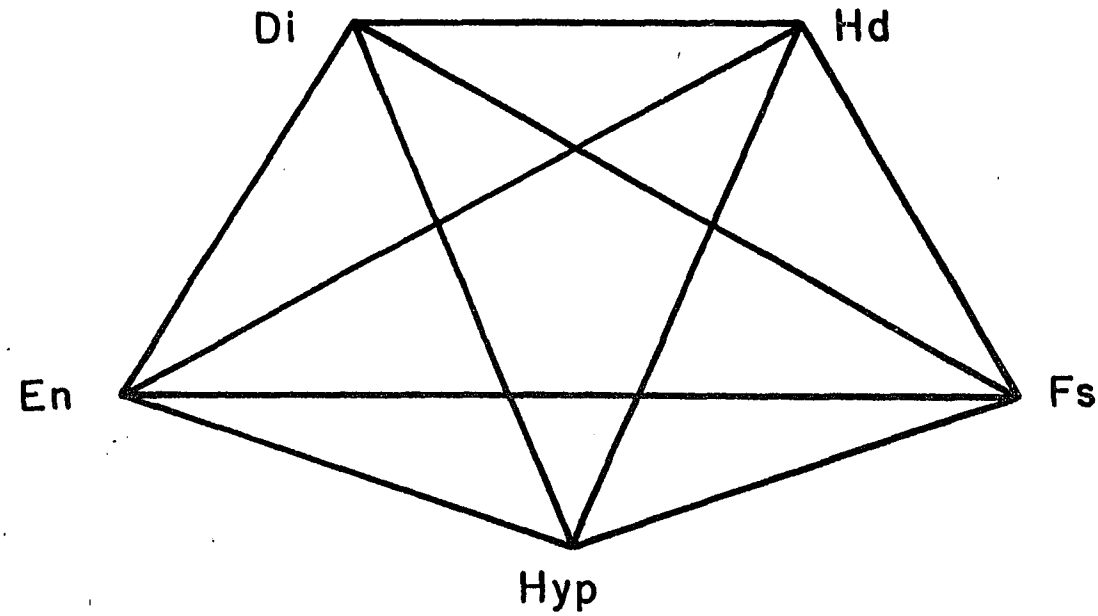

Figure 5.2 Binary solutions needed to model the equilibrium site occupancy of a single orthopyroxene crystal. Endmembers are: (1) enstatite; (2) diopside; (3) ferrosilite (4) hedenbergite; (5) ordered hypersthene.

Table 5.1. Mole fractions of ordered endmembers

Mole Fractions (Ternary)		Equilibrium site occupancy	Calculated end members	
Mg	0.534	$X_{Fe}^{M1} = 0.186$	En:	0.254
Fe	0.456	$X_{Fe}^{M2} = 0.726$	Di:	0.011
Ca	0.010		Fs:	0.177
			Hd:	0.009
			Hyp:	0.549

The binary solutions between ordered hypersthene and enstatite or ferrosilite may be closer to ideality.

Again, the method used was the minimization of total Gibbs Free Energy (Saxena and Eriksson, 1983) as described in chapter II. The model again uses the Kohler formulation for the interaction of the binary solutions. The method of calculation was the same as in chapter II, except this time we minimized the free energy for a single crystal rather than for two pyroxenes or for a complete assemblage. The equilibrium site occupancies for orthopyroxenes discussed in chapter IV can be used to test the models. Again, the W_{ij} values are not independent and should not be used for any other calculations. The additional constraints are as stated in section II.

Attempts at modeling the equilibrium site occupancies of a single crystal, from a macroscopic viewpoint, were unsucessful. The main problem areas were again in the high iron and high magnesium compositional range. The samples in the central compositional range were often acceptable (the modeled value being ±0.02 from the experimental site occupancies). Changing the permissible W_{ij} values or the estimated values for ordered hypersthene to bring the site occupancies of the iron-rich side into alignment resulted in a greater difference between the model values and the experimental data of the magnesium-rich and vice-versa. All the binary solutions were changed in an attempt to model the system apart from those defined in the model in chapter II.

The experimental data used to test this model have not been fully evaluated (see section IV). However, the differences between the various samples are small compared to the differences between the site

occupancies predicted by the model and the experimental values.

The problems in the macroscopic model in the Fe and Mg rich areas will have to be resolved before this method can be retried. Although this model tested well against the macroscopic data (i.e. coexisting pyroxenes) it may not be valid as a model for the microscopic data (i.e. site occupancies). However, to redesign the macroscopic model we need tighter constraints. This will include more experimental data and further thermodynamic modeling of systems containing the same elements and perhaps some of the same binary solutions. Such work is currently in progress (e.g. Chatterjee, 1987).

When the problems concerning the equilibrium site occupancy data are understood and resolved and more data is available to test the macroscopic model this idea can be tried again. There seems to be no reason why this simple model should not succeed in the future.

VI. APPLICATION OF MODELS

In section III, a theoretical method for obtaining equilibrium site-occupancy data for any composition at any temperature was discussed. In section V the relationship between the energies defined by the binary solutions and the site-occupancy was also reviewed. Together these methods make a detailed thermal history of any pyroxene-bearing rock possible. In this section the theory of using conventional geothermometry along with site-occupancy data to calculate a cooling history is used.

In section II the theory to calculate the rate constant ($\vec{K}$) for the disordering reaction

$$Mg^{2+}(M1) + Fe^{2+}(M2) \rightarrow Fe^{2+}(M1) + Mg^{2+}(M2) \qquad (3.b)$$

was developed resulting in the equations

$$-\vec{K}\Delta t = \frac{1}{(b^2-4ac)^{\frac{1}{2}}} \ln \left| \frac{+(2aX_{M2}^{Fe} + b) - (b^2 - 4ac)^{\frac{1}{2}}}{(2aX_{M2}^{Fe} + b) + (b^2 - 4ac)^{\frac{1}{2}}} \right| \begin{matrix} X_{M2}^{Fe}(t_1) \\ X_{M2}^{Fe}(t_o) \end{matrix} \qquad (3.6)$$

for ordering, and

$$-\vec{K}\Delta t = \frac{1}{(b^2-4ac)^{\frac{1}{2}}} \ln \left| \frac{-(2aX_{M2}^{Fe} + b) + (b^2 - 4ac)^{\frac{1}{2}}}{(2aX_{M2}^{Fe} + b) + (b^2 - 4ac)^{\frac{1}{2}}} \right| \begin{matrix} X_{M2}^{Fe}(t_1) \\ X_{M2}^{Fe}(t_o) \end{matrix} \qquad (3.6)$$

for disordering.

where

$$a = \tfrac{1}{2}\,(1-K_D^{-1})$$

$$b = \tfrac{1}{2} - X_{Fe} + K_D^{-1}(X_{Fe}+\tfrac{1}{2})$$

$$c = -K_D^{-1}X_{Fe}.$$

A. TTT diagrams.

The kinetic rate of the intracrystalline reaction (the transformation) can be displayed on a time-temperature-transformation (TTT) diagram. The progress of the exchange reaction plots as a series of C-shaped curves on a graph of temperature against log time. As the rate of reaction differs for each composition, faster with increasing iron-content, an individual TTT diagram must be drawn for each composition.

To plot the TTT diagram we must obtain the value of Fe^{2+} in M2 for an initial (highest) temperature (T_o), the peak metamorphic temperature from which cooling commences. This can be estimated from conventional geothermometry techniques i.e. two pyroxene geothermometry. (Several TTT diagram were plotted changing T_o. The curves are not sensitive to changes up to 100°C because the rate constant changes correspondingly.)

The value of Fe^{2+} in M2 with respect to temperature can be obtained by plotting $\ln K_D$ against 1/T for the equilibrium experimental data. Completely defined,

$$RT\ln K_D = -\Delta G^o_a + W^{M2}(1-2X^{M2}_{Fe}) - W^{M1}(1-2X^{M1}_{Fe}) + \Delta G^o_b\,(X^{M2}_{Fe} - X^{M1}_{Fe}) \qquad (6.1)$$

where

ΔG^o_a is for the ion-exchange reaction (1)

ΔG^o_b is the reciprocal reaction

and W^{M2}, W^{M1} are the interaction parameters on each site.

This equation has been discussed at the end of chapter IV. Three different models were proposed (Ganguly, 1982; Anovitz et al., 1988; This study). However, due to the problems with resolving this equation

(i.e. do the Mössbauer samples need to be adjusted in the high iron range), the simpler method of Ganguly (1982) has been followed here for the TTT diagrams, where

$$\ln K_D = A/T + B \qquad (6.2)$$

This method is believed to be a good approximation.

The resulting values of A and B are shown in Table 6.1 and can be seen in Figure 6.1 for samples 4 and 5. (Data used is from Tables 3.3a and 3.3b.) Conditional errors, as described previously, have been added to the diagram. The maximum temperature range for the natural samples is included. Equation (6.2) can be used to calculate the value of K_D at T_0. From this the site occupancy of Fe^{2+} in M2 can be calculated using the following equation from Ganguly (1982).

$$X_{Fe}^{M2} = \frac{-B + (B^2 - 4AC)^{\frac{1}{2}}}{2A}$$

where $A = \frac{1}{2}(K_D - 1)$

$B = K_D(\frac{1}{2} - X_{Fe}) + X_{Fe} + \frac{1}{2}$

$C = -X_{Fe}$.

Table 6.1 Regressed constants for $\ln K_D = A/T + B$

Sample	A	B
4 (Av)	-4605	2.82
4	-4605	2.57-2.97
4	-4451 - -4844	2.82
5 (Av)	-2753	1.24
5	-2753	1.04-1.42
5	-2603 - -1913	1.24

Regressed constants for $\ln K_D$ versus 1/T (K) for samples 4 and 5. Where $\ln K_D = A/T + B$. Conditional errors have been calculated.

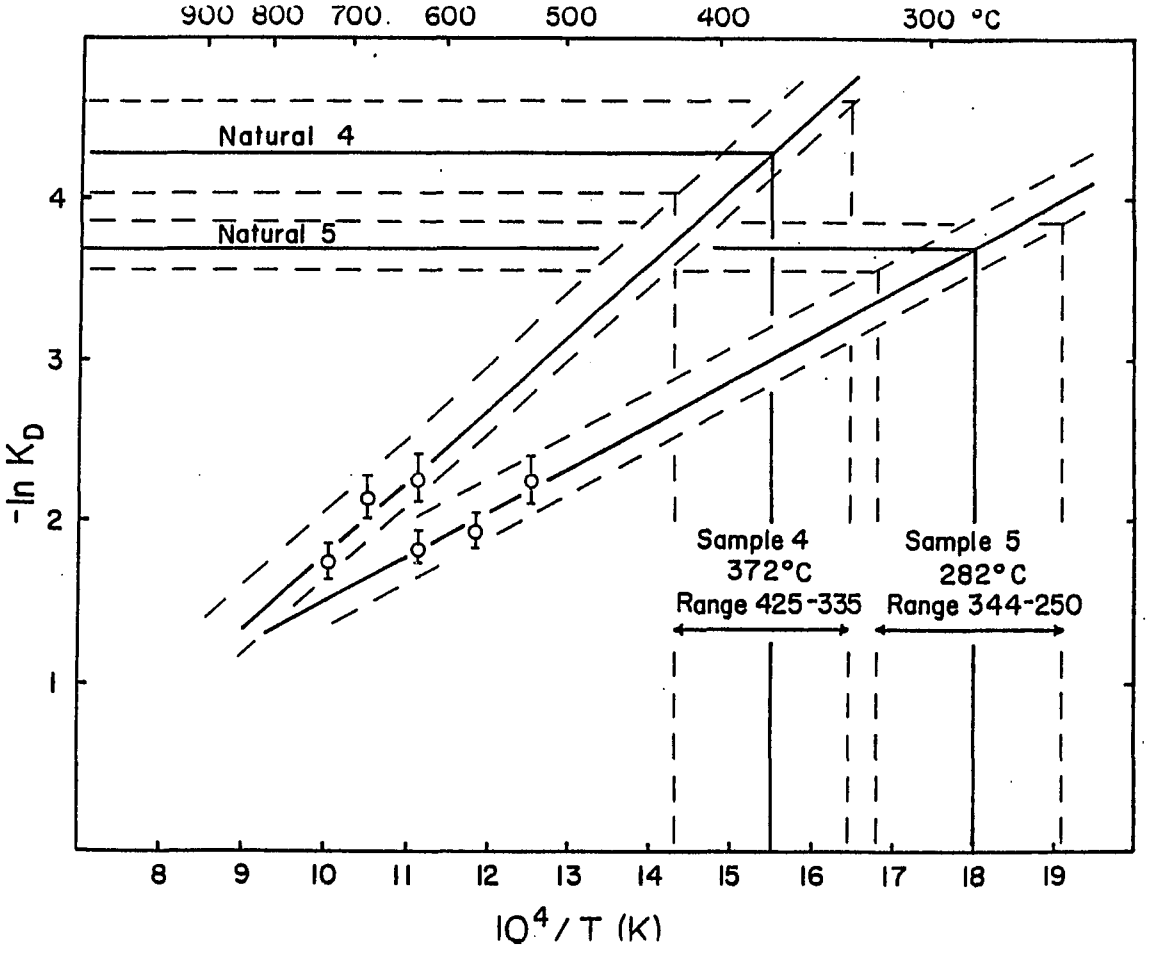

Figure 6.1. Plot of the equilibrium values of $\ln K_D$ against $10^4/T$ for samples 4 and 5. Error bars drawn are two standard deviations. Thick solid lines indicate the least squares fit to the data points, dashed lines indicate conditional errors. Superimposed onto this are the values of K_D for the natural (unheated) samples. The range indicated is $K_D \pm 0.004$ for both samples. The average equilibrium temperature for the natural samples and the range of temperature, combining all errors, are indicated in the lower right of the Figure.

The TTT diagram can be used to study simple metastability due to kinetics. A schematic diagram of the different cooling rates, applicable for slowly cooled metamorphic rocks can be seen in Figure 6.2. Again, if we assume that a rock cools with a constant rate, the cooling rate can be plotted as a horizontal straight line (a). The rate of intracrystalline ion-exchange decreases with temperature and ion-exchange equilibrium cannot be maintained. At temperatures below T_1 ion-exchange does continue, but at a slower pace.

The corresponding values of K_D are shown on the lower diagram where curve (c) represents the path if equilibrium was constantly attained. This would be the path indicated by extrapolation of heating experiments at temperatures above T_1 such as those used in figure 6.1. Curve (d) shows a possible path (below T_1) when the intracrystalline exchange reaction has slowed but not stopped. The change in K_D is less than in the equilibrium situation. Path (d) results in a non-equilibrium K_D that is different than the predicted equilibrium value.

The value of K_D found in the natural sample is shown on the lower diagram. This yields a different temperature for curves (c) and (d). The closure temperature T_c, (the same as that calculated from figure 6.1.) is higher than the quench temperature T_q obtained from curve (d). The quench temperature can be defined as the temperature below which the observable ion-exchange ceases. This problem can be addressed using the TTT diagram and T_q will be indicated.

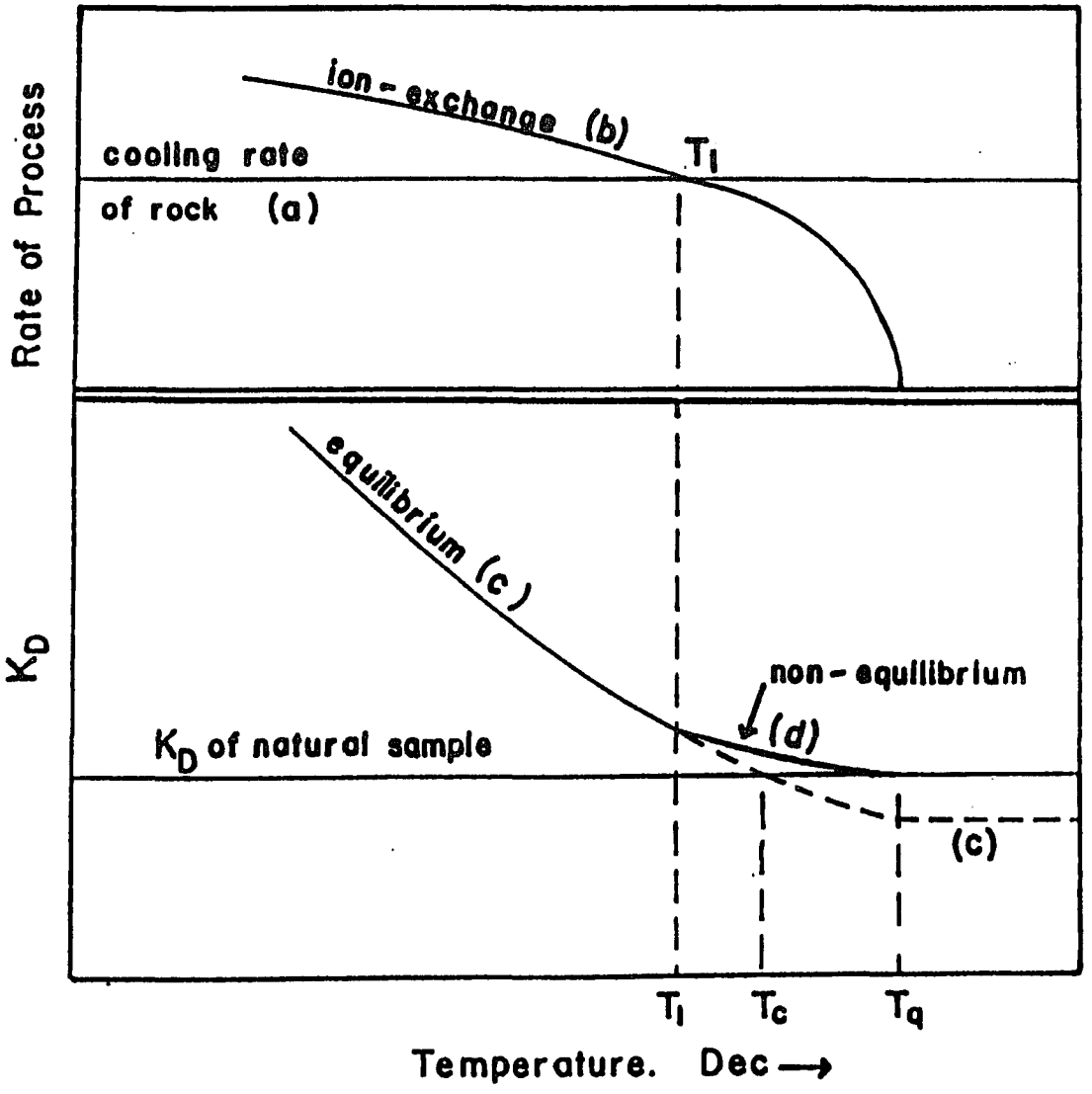

Figure 6.2. Relationships of the rates of intercrystalline ion-exchange and the cooling history of the whole rock. Shown both as a function of process rate and as the effect on K_D. See text for details

For drafting the TTT diagram, equation 3.6 for ordering can be rearranged to yield the value of Fe^{2+} in M2 for any temperature at any time. The symbols used follow those of Ganguly (1982).

$$X_{Fe}^{M2}(t) = \frac{(b^2 - 4ac)^{\frac{1}{2}}(1+FD) - b(1-FD)}{2a(1-FD)} \qquad (7)$$

where $F = \exp[-\vec{K}\Delta t(b^2 - 4ac)^{\frac{1}{2}}]$

and $$D = \frac{[2aX_{Fe}^{M2}(t_o) + b] - (b^2 - 4ac)^{\frac{1}{2}}}{[2aX_{Fe}^{M2}(t_o) + b] + (b^2 - 4ac)^{\frac{1}{2}}}$$

The values of Q and K* already calculated can be used to calculate $\vec{K}$ and values A and B are used to calculate Fe^{2+} in M2, both at the temperature of interest. The values used in these calculations are shown in Table 6.2. Also indicated are the calculated values of Fe^{2+} in M2 at T_0.

Figures 6.3 and 6.4 show the TTT diagrams for samples 4 and 5 respectively. It must be stressed at this time, as stated by Ganguly (1982), a thermal history calculation based on Fe^{2+}-Mg^{2+} exchange in orthopyroxene, assumes that the time required by a crystal to attain a certain equilibrium and ordering state under isothermal (experimental) conditions is the same as that in a continually cooling (natural) system.

The TTT diagrams show that isothermally, the change in Fe^{2+} in M2 with ordering is small at higher temperatures and occurs rapidly; at lower temperatures the change in Fe^{2+} in M2 is greater but the transformation is slower. After a certain period of time equilibrium

Table 6.2. Values used to calculate TTT diagrams

	Sample 4	Sample 5
Q cal/mol	49000	50600
K*/year	4.93 E+15	2.72 E+17
A	-4605	-2753
B	2.82	1.24
X_{Fe}	0.62	0.86
$T_0(K)$	1023	873
$X_{M2}^{Fe}\ T_0$	0.805	0.947

will be attained and the value of Fe^{2+} in M2 will remain constant with time. This is the flat upper part of the C-curve parallel to the time axis. The lower part of the C-curves are simply contours of equal amounts of Fe^{2+} in M2 and do not represent an equilibrium situation at that temperature.

The cooling curve of the rock is superimposed on the TTT diagram. In this study the asymptotic model for a cooling rock has been used following Ganguly, (1982). This model corresponds to the equation

$$\eta t = 1/T_q - 1/T_o$$

where t is time and η is the cooling time constant. The cooling curve for the whole rock is plotted using the same time and temperature scales as the C-curves for site occupancy. Following the cooling curve, the value of Fe^{2+} in M2 increases with increasing time. Knowing the amount of Fe^{2+} in M2 in the natural sample we can constrain the value of η and hence obtain the cooling history.

The cooling curve must touch the C-curve at the point corresponding to the value of Fe^{2+} in M2 for the natural sample. If just the equilibrium situation is considered, the cooling curve would touch the C-curve at the point where it becomes parallel to the time axis i.e. no further change in Fe^{2+} in M2 with time. This corresponds to the temperature T_c. If the cooling curve is drawn such that it touches the C-curve tangentially this corresponds to a temperature T_q. This is not the equilibrium value for Fe^{2+} in M2 for this temperature.

Knowing the difference in temperature between T_o and T_q and the time needed to reach the value of Fe^{2+} in M2 for the natural sample value at T_q, a rate in degrees per year can be calculated. The results can be seen in Table 6.3.

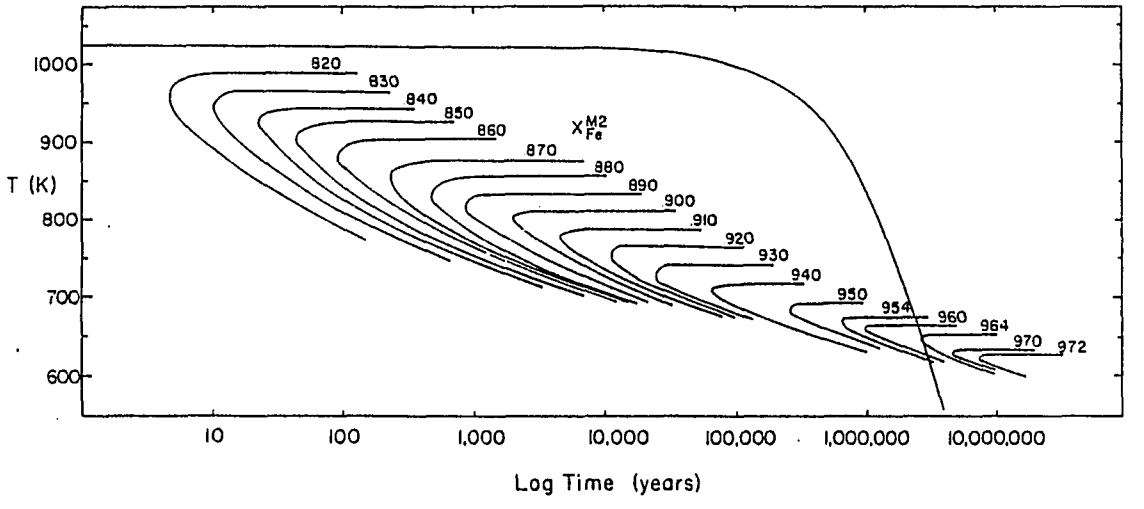

Figure 6.3. Time-temperature-transformation (TTT) diagram for sample 4. The diagram is contoured in values of Fe^{2+} in the M2 site, with increasing ordering as temperature decreases, see text for details. Superimposed on these contours is a cooling curve, using the asymptotic model.

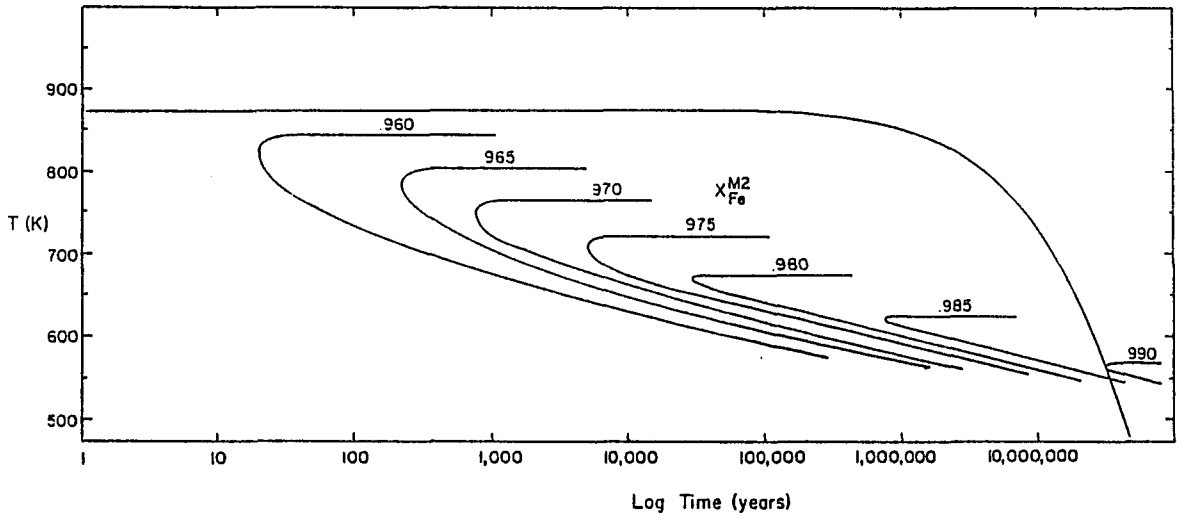

Figure 6.4. Time-temperature-transformation (TTT) diagram for sample 5. See Figure 6.3 for details.

Table 6.3. Summary of cooling rates.

	Sample 4	Sample 5
T_0(K)	1023	873
T_q(K)	646	560
X_{M2}^{Fe}(natural)	0.964	0.990
η / year	2.11 E-10	2.19 E-11
Cooling rate °/ million years	140	11

B. Cooling Histories

The range of cooling rates for these two samples is quite large. It should be noted at this time that the exact location of sample 4, within its province is not known. In addition, the oxygen fugacity within the rock during cooling is unknown. The composition of the orthopyroxene crystal should not affect the cooling rate calculated. Fe-rich or Mg-rich samples from the same areas should give approximately the same cooling rates. However, they may be influenced by the Fe^{2+}-Mg^{2+} exchange continuing to lower temperatures in the Fe-rich samples and resulting in lower T_q's for the iron-rich samples.

Sample 4 is from a Precambrian terrain in southern Finland (Saxena, 1968). The sample area is in the Svecofennian formation, an area of metasediments affected by the Svecokarelidic orogeny 1800-1900 m.y. ago. Regional metamorphism was amphibolite grade with areas of granulite. This was followed by a long period of erosion, intrusion in some areas of rapakivi granites (1700-1400 m.y.), deposition of red beds (1300-1400 m.y.) and finally the intrusion of diabase dikes. The rocks are little changed since this time. Geothermometry on the Attu zone in the central area yields temperatures of 700-780°C (Schellekens, 1980), and further north, around Tampere, temperatures of 690-750°C are demonstrated (Campbell, 1980).

The cooling rate was calculated using Q, K*, A and B from our experiments and an average of the natural samples for the value of $Fe^{2+}M2$. The cooling rate of 140°/ milion year is slightly faster than would be expected for this area. This area has experienced a relatively stable tectonic history. In comparison, a cooling rate calculated for rapid decompression of granulites due to erosion from the Central

Massif, France, is 20-26°/m.y. (Albarede, 1980). Therefore, the cooling rate calcualted for sample 4 is too fast, unless this sample has been affected by either the granitic intrusions or the diabase dikes.

Sample 5 is from a high-grade metamorphosed iron formation within the Archean rocks of the Wind River Mountains, Wyoming. The area has had a very complex history with at least three periods of deformation (Mitra and Frost, 1981) and two periods of metamorphism both in the Archean and at least to amphibolite facies (Koesterer et al., 1985). The area was eroded during the Late Precambrian, then a thick sequence of sedimentary rocks was deposited. The Laramide orogeny in Late Cretaceous to Early Eocene times resulted in folding, faulting and overthrusting of the range.

An initial temperature of 600°C was chosen, the average temperature of many two-pyroxene samples studied from the iron-rich body from which this sample was taken (Sykes, 1984, unpublished Master's thesis). The rest of the data is listed in Table 6.3. The cooling rate calculated, 11°/ million years is well within the expected range for a granulitic rock.

C. Errors

Figure 6.5 has been drafted to show schematically, for any sample, the tremendous problems due to error propagation for this method of study. Five variables interact to yield the TTT diagram. As stated earlier, changing T_0 does not have an effect on the TTT diagram as the rate changes accordingly. These errors have all been estimated separately; the interactions are not investigated which would add to the errors.

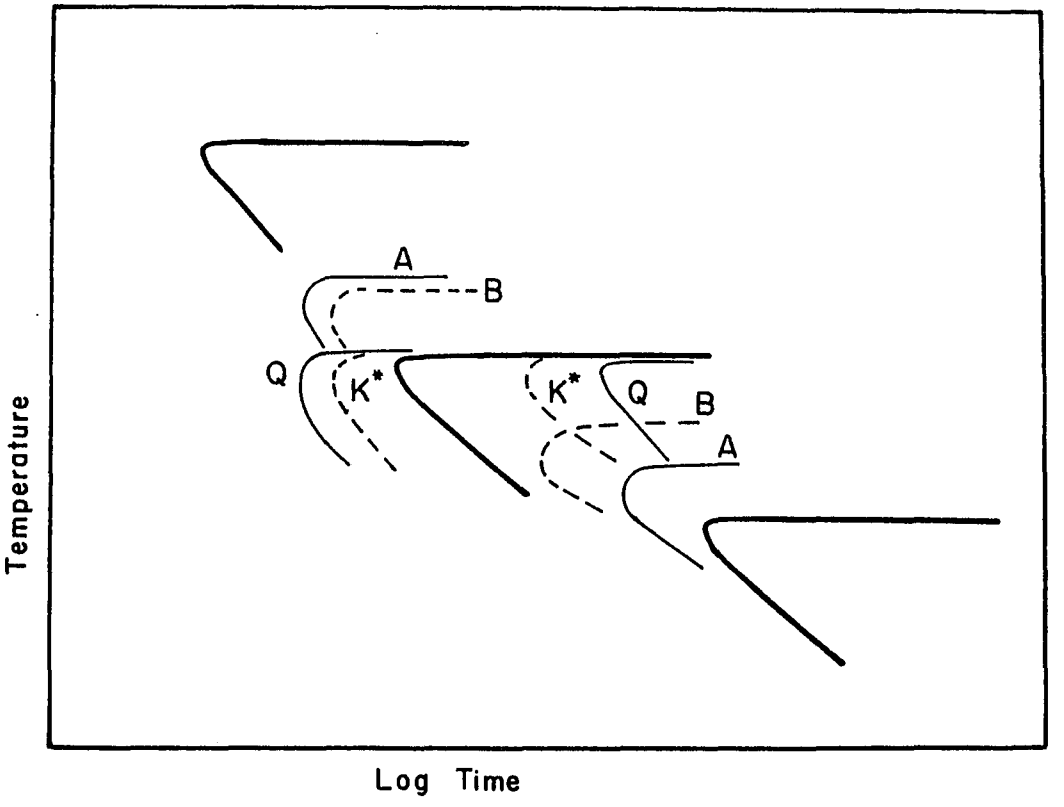

Figure 6.5. Schematic diagram of errors for the TTT diagram. See text for details.

The heaviest lines on Figure 6.5, central, upper left and lower right, indicate the range in the composition (one standard deviation of ± 0.008) of the Fe^{2+} in M2 in the natural sample. Although not shown, each of these values would have a corresponding set of curves similar to that of the average value (central). It is found that changing Q and K* (hence $\vec{K}$) within the conditional errors derived from the Arrhenius plot affects the equilibrium curve with respect to the time axis only. The position relative to temperature remains unchanged. Changing A and B (hence K_D) within the conditional errors affects the equilibrium curve with respect to both axes.

It can be seen that these changes (all reasonable errors) drastically affect the position of the equilibrium cooling curve and, therefore, can change the cooling rate by several orders of magnitude.

D. Conclusions

Due to the errors inherent in the initial site occupancies, rate constants calculated, activation energies and the plot of $\ln K_D$ against 1/T, cooling rates obtained are still "order of magnitude" and are expected to remain at this level. The calculated cooling rates can correspond to those expected from a geophysical (or a simple geologic) standpoint, but some rates are faster that that expected in nature. Several areas of further exploration are necessary to establish why this is so.

Experimental factors such as oxygen fugacity and pressure may play a role, also the time taken for the quench to occur may be significant. The reaction measured in the laboratory may be different to that occuring in nature, especially at low temperatures and very slow diffusion rates, when the sample is highly ordered. Also, we do not

know at what temperature the ion-exchange reaction ceases, we have simply extrapolated the experimental data to very low temperatures to find the C-curve corresponding to the site occupancy of the natural sample.

It has become obvious that if this method is to be used for calculation of cooling rates of various areas much more care needs to be taken in sample selection. The samples here have all undergone long and complex histories. Even in the initial stages it is obvious that if the sample is part of a upthrusted area, the cooling rate calculated must be dependent on the location of that sample within the slab. It is suggested that samples from much studied areas where the geology is tightly controlled and the cooling history is well known (either by geophysics and/or fission tracks) could be used to help to understand the results obtained thus far.

VII. SUMMARY

This study has involved both theory and experiments concerning the intercrystalline or macroscopic reactions (between coexisting orthopyroxene and clinopyroxene), and the intracrystalline or microscopic reactions (between sites in orthopyroxene) in pyroxenes.

Thermodynamic modeling calculations of the topology of the pyroxene quadrilateral solvus was done in the first part (Chapter II). The model was tested by its ability to reproduce experimentally derived, intercrystalline equilibrium ion-distribution between orthopyroxene and clinopyroxene. The fit of the model to the data was good, the only problems being for the very high iron and very high magnesium compositions.

The application of this model was to calculate a pyroxene geothermometer. Two graphical geothermometers were created from the thermodynamic data set to investigate the theory that the Fe^{2+}-Mg exchange reaction had a lower closure temperature than the Ca-transfer reaction. These two graphical geothermometers were tested for all rock types.

For rapidly cooling igneous rocks (a dike and a pumice rock), the geothermometers predicted the expected coinciding quench temperatures. The plutonic rocks showed a substantial range of temperature between the two geothermometers with the Fe^{2+}-Mg exchange reaction giving the lower temperature. The agrees with the theory that this exchange reaction proceeds to a lower temperature than the Ca-transfer reaction and indicates that the kinetics of these two reactions are different.

For contact metamorphic rocks and regionally metamorphosed rocks, the two graphical geothermometers compare favorably with two-pyroxene geothermometers derived in other studies. In addition, the Fe^{2+}-Mg exchange geothermometer records lower temperatures. The two geothermometers also indicate interesting relationships for two other regionally metamorphosed areas and may help unravel the complex history of such terranes. A further, highly favorable feature of these two geothermometers is the ease of their use.

Intracrystalline ion-exchange was studied experimentally for two samples in the second part of this study. This reaction, in comparison to the intercrystalline exchange reactions, occurs over smaller lengths of diffusive paths and, therefore, continues to a much lower temperature. With heating, the Fe^{2+} and Mg ions in the orthopyroxene structure become more ordered, with the larger Fe^{2+} ion going into the larger, irregular M2 site, and Mg entering into the smaller M1 site.

The structural changes in bond lengths, cell volumes, etc. with increasing heating of the crystals have been studied. These compare favorably with other studies. Instability in the structure of the iron-rich samples for longer heating periods has been studied by SEM and TEM. No external oxidation products or secondary phases in the crystals were found. An internal oxidation reaction with the formation of Fe^{3+} and a vacancy in the lattice is suggested to explain the phenomenom.

The kinetic rate and activation energy of the ion-exchange reaction were calculated for both samples and compared to other studies. All the kinetic rate constants showed an increase with both increasing temperature and increasing iron. Rate constants for the ordering experiments are found to be faster, as expected theoretically. The

activation energies divide the samples into two groups; high activations energy, approximately 60 Kcal/mol, for the Mg-rich samples and a lower activation energy group, approximately 50 Kcal/mol for the Fe-rich samples. This coincides with a change in the relative rates of site infilling in orthopyroxene and with a change in tie-line slope for coexisting pyroxenes. The two groups of samples show the same systematic trends for the value of the frequency factor as other silicates, and also follow the Compensation Law established for diffusive processes.

A possible equation, relating equilibrium site occupancies from different experimental techniques and studies, was discussed and developed in the third part of this study. There are still many discrepancies and a model for obtaining equilibrium site occupancies for any temperature and composition is still unattainable.

Theory and calculations for the development of a thermodynamic model for both the inter- and intra-crystalline reaction were discussed in section four. The theory seems valid. The model includes the data set developed for the macroscopic reactions from the first section, extended to include the microscopic reactions. The model produced did not yield the equilibrium site occupancies obtained experimentally. The problems in the high iron and magnesium range found with the initial thermodynamic model seem to expand when applied to the microscopic model.

Finally, thermal histories of the two samples studied experimentally are derived. Average cooling rates of 11° and 140° per million years are calculated. The first rate is well within the range expected for a granulite rock, the second rate is much faster. The

error propagation is investigated and it is found that these cooling rate estimates can never be better than "order of magnitude"; equivalent in many ways to the other methods of estimating cooling rates. In addition, many of the samples chosen for this method of study come from areas with highly complex thermal histories and, therefore, evaluation of which part of the history of the rock relates to the rate calculated is very difficult. It is suggested that samples from well studied areas with geophysical and fission track data on uplift rates should be studied in the future to realise the validity of the method.

APPENDIX A

Values of Fe in M2 at time t for different rate constants.

```
10 REM TO CALC VALUES OF FEM2 FOR DIFFERENT VALUES OF K
20 REM EQUATION FOR FEM2 FOR DISORDERING
30 REM X5;((FE1/FE2)/2 FOR SAMPLE)
40 INPUT "FE/(FE+MG) FOR THE SAMPLE";X5
50 REM FE3;(FE IN M2 AT INITIAL TEMP)
60 INPUT "FEM2 OF NATURAL SAMPLE";FE3
70 REM FE2, FEM2 FOR THE SAMPLE AT EQUILIBRIUM
80 INPUT "FEM2 FOR SAMPLE AT EQUILIBRIUM";FE2
90 INPUT "CHOOSE A COOLING RATE"; K1
100 P=.5
110 Q=.5
120 FE1=(2*X5)-FE2
130 KD=(FE1*(1-FE2))/((FE2)*(1-FE1))
140 READ T
150 IF T=0 THEN 270
160 A = P*(1-(1/KD))
170 B = Q-X5+(1/KD)*(X5+P)
180 C = -(1/KD)*(X5)
190 R = (B*B - (4*A*C))^.5
200 J =EXP(-K1*T*R)
210 S1 = (2*A*FE3) + B
220 G1 = (-S1+R)/(S1+R)
230 G2 = G1*J
240 L = (R*(1-G2)-B*(1+G2))/(2*A*(1+G2))
250 PRINT T,L
260 GOTO 140
270 INPUT"TO EXIT FROM PROGRAM TYPE 1",Z
280 IF Z=1 THEN 350
290 INPUT "TO CHANGE ALL;2 JUST FEM2 EQLIB TYPE 3, COOLING RATE RETURN";P2
300 RESTORE
310 IF P2 = 2 THEN 60
320 IF P2=3 THEN 80
340 GOTO 90
350 END
```

APPENDIX A

Least-squares regression for Q (activation energy) and K^*.

```
10 INPUT "N=";N
20 FOR I=1 TO N
30 READ K(I),T(I)
40 Y(I)=K(I)
50 X(I)=1/T(I)
60 X=X+X(I)
70 Y=Y+Y(I)
80 XY=XY+X(I)*Y(I)
90 XX=XX+X(I)^2
100 NEXT I
110 A=(Y/X-XY/XX)/(N/X-X/XX)
120 B=(Y/X-A*N/X)
130 PRINT "Ln(K*)= ";A,"K*= ";EXP(A),"Q= ";-B*8.314/4.184
150 SY=A+B*X(I)
180 DATA 7.22, 823, 8.75, 873, 10.51, 973
190 END
```

APPENDIX A

Least-squares regression for constants A and B, where $LnK_D = A/T + B$

```
10 INPUT "N=";N
20 FOR I=1 TO N
30 READ K(I),T(I)
40 Y(I)=K(I)
50 X(I)=1/T(I)
60 X=X+X(I)
70 Y=Y+Y(I)
80 XY=XY+X(I)*Y(I)
90 XX=XX+X(I)^2
100 NEXT I
110 A=(Y/X-XY/XX)/(N/X-X/XX)
120 B=(Y/X-A*N/X)
130 PRINT "B";A,"A= ";B
180 DATA -1.969, 798, -1.748, 848, -1.476, 898
190 END
```

APPENDIX A

Equilibrium values of Fe in M2 at time t (for TTT diagrams)

```
10 REM TO CALC RATES FROM SITE OCCUPANCY DATA
20 REM FROM GANGULY EQN 31 PAGE 91 APC II
30 REM INSERT IN PROGRAM BEFORE RUNNING, FE3;(FE IN M2 AT INITIAL TEMP)
40 REM Q AND K FOR SAMPLE, X5;((FE1/FE2)/2 FOR SAMPLE)
50 REM A1, B1 FOR THE SAMPLE FROM EQUILIBRIUM KD'S
60 INPUT "TEMPERATURE OF INTEREST IN K",V
70 REM FE3 IS FE IN M2 AT TO presently 1023
80 FE3=.8
90 PRINT "VALUE OF FEM2 AT INITIAL TEMPERATURE",FE3
100 REM TO CALC K (RATE) AT TEMP OF INTEREST
110 Q=49000!
120 K=4.93E+15
130 REM X5 IS (FE1+FE2)/2 FOR THE SAMPLE
140 X5=.62
150 K1=(EXP(LOG(K)-Q/(1.987*V)))
160 PRINT "RATE OF K AT T OF INTEREST",K1,K6
170 REM TO CALC KD AT TEMP OF INTEREST
180 A1=-4194
190 B1=2.6
200 KD=EXP(A1/V+B1)
210 PRINT "VALUE OF KD AT T OF INTEREST",KD
220 REM TO CALCULATE EQUIL SITE OCC AT TEMP OF INTEREST
230 P=.5
240 Q=.5
250 A2=P*(KD-1)
260 B2=KD*(Q-X5)+X5+P
270 C2=-X5
280 FE2=(-B2+(B2*B2-4*A2*C2)^.5)/(2*A2)
290 PRINT "FE2 AT TEMP OF INTEREST",FE2
300 READ T
310 IF T=0 THEN 450
320 A = P*(1-(1/KD))
330 B = Q-X5+(1/KD)*(X5+P)
340 C = -(1/KD)*(X5)
350 R = (B*B - (4*A*C))^.5
360 J= EXP(-K1*T*R)
370 S1 = (2*A*FE3) + B
380 G1 = (S1-R)/(S1+R)
390 G2 = G1*J
400 G3 = (2*A *(G2+1))
410 L = (R*(1+G2)-B*(1-G2))/(2*A*(1-G2))
420 PRINT T,L
430 GOTO 300
450 INPUT"TO EXIT FROM PROGRAM TYPE 1",Z
455 RESTORE
460 IF Z=1 THEN 470
462 GOTO 60
465 DATA 3, 5, 10, 15,20,30, 50, 100, 300, 600, 1000, 0
470 END
```

REFERENCES

Albarede, F. (1976) Thermal models of post-tectonic decompression as exemplified by the Haut-Allier granulites (Central Massif, France). Bulletin Societe Geologie France, 7, 1023-1032.

Anovitz, L.M., Essene, E.J. and Dunham, W.R. (1988) Order-disorder experiments on orthopyroxenes: Implications for the orthopyroxene speedometer. American Mineralogist, 73, 1060-1073.

Atkins, F. B. (1969) Pyroxenes of the Bushveld Intrusion, South Africa. Journal of Petrology, 10, 222-249.

Bancroft, G. M. (1973) Mössbauer spectroscopy. An introduction for inorganic chemists and geochemists. John Wiley and Sons, 252p.

Barron, L.M. (1978) The geometry of multicomponent exsolution. American Journal of Science, 278, 1269-1306.

Berg, J.H. and Docka, J.A. (1983) Geothermometry of the Kiglapait Contact Aureole, Labrador, American Journal of Science, 283, 414-434.

Barnes,.C.G., Allen, C.M. and Saleeby, J.B. (1986) Open- and closed-system characteristics of a tilted plutonic system, Klamath Mountains, California. Journal of Geophysical Research, 91, 6073-6090.

Barnes, C.G. (1987) Mineralogy of the Wooley Creek batholith, Slinkard pluton, and related dikes, Klamath Mountains, northern California. American Mineralogist, 72, 879-901.

Besancon, J.R. (1981) Rate of cation disordering in orthopyroxenes. American Mineralogist, 66, 965-973.

Besancon, J.R. (1981b) Cooling rate of orthopyroxene-bearing rocks estimated from magnesium-iron intersite distribution. Transactions of the American Geophysical Union, EOS, 62, 437.

Bohlen, S.R. and Boettcher, A.L. (1981). Experimental investigations and geological applications of olivine-orthopyroxene geobarometry. American Mineralogist, 66, 951-964.

Brady, J.B. and McCallister, R.H. (1983). Diffusion data for clinopyroxene from homogenization and self-diffusion experiments. American Mineralogist, 68, 95-105.

Brousse, C., Newton, R.C. and Kleppa, O.J. (1984). Enthalpy of formation of fosterite, enstatite, Åkermanite, monticellite and merwinite at 1073 K. Geochimica et Cosmochimica Acta, 48, 1081-1088.

Buening, D.K. and Buseck, P.R. (1973) Fe-Mg Lattice diffusion in Olivine. Journal of Geophysical Research, 78, 6852-6862.

Cameron, M. and Papike, J.J. (1980) Crystal chemistry of silicate pyroxenes. Reviews in Mineralogy, 7, 5-92.

Campbell, D.S. (1980) Structural and metamorphic development of migmatites in the Svecokarelides, near Tampere, Finland. Transactions of the Royal Society of Edinburgh, Earth Sciences, 71, 185-200.

Cannillo, E., Germani, G. and Mazzi, F. (1983) Nuovo software crstallografico per il diffracttometro a cristallo singolo Phillips Pw 1100. C.N.R., Centro diStudio per la Crystallographica Strutturale, International Report 2, 1983.

Chatillon-Collinet, C., Newton, R.C. Perkins III, D. and Kleppa, O.J. (1983) Thermochemistry of $(Fe^{2+},Mg)SiO_3$ orthopyroxene. Geochimica et Cosmochimica Acta, 47, 1597-1603.

Chatterjee, N. (1987) Evaluation of thermochemical data on Fe-Mg olivine, orthopyroxene, spinel and Ca-Fe-Mg-Al garnet. Geochimica et Cosmochimica Acta, 51, 2515-2526.

Clifford, A.A. (1973) Multivariate error analysis. Applied Science, Publishers Ltd., Essex, England.

Colby, J.W. (1972) MAGIC IV, a computer program for quantitative electron microprobe analysis. Bell Telephone Laboratories Inc., Allentown, PA.

Coleman, L.C. (1978) Solidus and subsolidus compositional relationships of some coexisting Skaergaard pyroxenes. Contributions to Mineralogy and Petrology, 66, 221-227.

Dal Negro, A., Carbonin, S., Molin, G.M., Cundari, A. and Piccirillo, E.M. (1982) Intracrystalline cation distributions in natural clinopyroxenes of tholiitic, transitional and alkaline basaltic rocks. Advances in Physical Chemistry, 2, 117-150.

Davidson, P.M. (1988) Phase separation in pyroxenes and olivines. Advances in Physical Geochemistry, 7 (in press).

Davidson, P.M. (1987) Internally consistent thermodynamic analysis of pyroxene-olivine-quartz equilibria. Transactions of the American Geophysical Union, EOS, 68, 459.

Davidson, P.M. (1985) Thermodynamic analysis of quadrilateral pyroxenes: Part I. Derivation of the ternary non-convergent site-disorder model. Contributions to Mineralogy and Petrology, 91, 383-389.

Davidson, P.M., Grover, J.E. and Lindsley, D.H. (1982) $(CaMg)_2Si_2O_6$ clinopyroxenes: a solution model based on nonconvergent site-disorder. Contributions to Mineralogy and Petrology, 80, 88-102.

Davidson, P.M. and Lindsley, D.H. (1985) Thermodynamic analysis of quadrilateral pyroxenes: Part II. Model calibration from experiments and applications to geothermometry. Contributions to Mineralogy and Petrology, 91, 390-404.

Deer, W.A., Howie, R.A. and Zussman, J. (1978) Rock forming minerals, 2A, Single chain silicates. 2nd. edition, J. Wiley and Sons N.Y., 668p.

Deines, G.J. (1955) Kinetics of order-disorder transformations. Acta Metallurgica, 3, 549-557.

Docka, J.A., Berg, J.H. and Klewin, K.W. (1985) Geothermometry in the Kiglapait Aureole: Part II. Evaluation of exchange thermometry in a well-constrained thermal setting. Journal of Petrology, 27, 605-626.

Domeneghetti, M.C., Molin, G.M. and Tazzoli, V. (1985) Crystal-chemical implications of the Mg^{2+}-Fe^{2+} distribution in orthopyroxenes. American Mineralogist, 70, 987-995.

Eriksson, G. and Rosen, E. (1973) Thermodynamic studies of high temperature equilibria, Chemica Scripta, 4, 193-194.

Evans, B.J., Ghose, S. and Hafner, S. (1967) Hyperfine splitting of ^{57}Fe and Mg-Fe order-disorder in orthopyroxenes ($MgSiO_3$-$FeSiO_3$ solid solution), Journal of Geology, 75, 306-322.

Fei, Y., Saxena, S.K., and Eriksson, G. (1986) Some Binary and ternary silicate solution models. Contributions to Mineralogy and Petrology, 94, 221-229.

Fonarev, V.I. and Graphchikov, A.A. (1982) Experimental study of Fe-Mg and Ca distribution between coexisting ortho- and clinopyroxenes at P = 294 MPa, T = 750 and 800°C. Contributions to Mineralogy and Petrology, 79, 311-318.

Ganguly, J. (1982) Mg-Fe order-disorder in ferromagnesian silicates. Advances in Physical Geochemistry, 2, 58-100.

Ganguly, J. and Ghose, S. (1979) Aluminous orthopyroxene: order-disorder, thermodynamic properties and petrological implications. Contributions to Mineralogy and Petrology, 69, 375-385.

Ganguly, J. and Saxena, S.K. (1984). Mixing properties of aluminosilicate garnets: constraints from natural and experimental data, and application to geothermo-barometry. American Mineralogist, 69, 88-97.

Ghose, S. (1982) Mg-Fe order-disorder in ferromagnesian silicates. Advances in Physical Geochemistry, 2, 4-57.

Ghose, S. (1965) Fe^{2+}-Mg^{2+} order in an orthopyroxene, $Mg_{0.93}Fe_{1.07}Si_2O_6$. Zeitschrift fur Kristallographie, 122, 81-99.

Ghose, S. (1961) The crystal structure of a cummingtonite. Acta Crystallographica, 14, 622-627.

Grammenopoulou, S. (1981) Eigenschaften und oxidationbestandigkeit synthetischer orthopyroxene. Ph.D. Dissertation, Christian-Albrechts University, Keil.

Guggenheim, E.A. (1967) Thermodynamics. North-Holland Publishing Co., Amsterdam, 437p.

Guggenheim, E.A. (1952) Mixtures. Clarendon Press, Oxford, 365p.

Guggenheim, E.A. (1937) Theoretical basis of Raoult's Law. Transactions of the Faraday Society, 33, 151-159.

Haselton, H.T. (1979) Calorimetry of synthetic pyrope-grossular garnets and calculated stability reaction. Ph.D. Thesis, University of Chicago.

Hawthorne, F.C. (1983) Quantitative characterization of site-occupancies in minerals. American Mineralogist, 68, 287-306.

Hedge, C.E., Houston, R.S., Tweto, O.L., Peterman, Z.E., Harrison, J.E. and Reid, R.R. (1986) The Precambrian of the Rocky Mountain Region, U.S. Geological Survey Professional Paper, 1241-D.

Helgeson, H.C., Delaney, J.M., Nesbitt, H.W. and Bird, D.K. (1978). Summary and critique of the thermodynamic properties of rock-forming minerals. American Journal of Science, 278A, 1-250.

Holland, T.J.B. (1980) The reaction albite = jadeite + quartz determined experimentally in the range 600-1200°. American Mineralogist, 65, 129-134.

Huebner, J.S. (1982) Pyroxene phase equilibria at low pressure. Reviews in Mineralogy, 7, 2nd. edition, 213-288.

International Tables for X-ray Crystallography (1974) Kynock Press, Birmingham G.B., Vol IV, 99-101.

James, F. and Ross, M. (1975) MINUIT, a system for function minimization and analysis of the parameter errors and correlations. Computer Physics, 10, 343-347, CERM/DD, International Report 75/20.

Khristoforov, K.K., Nikitina, L.P., Krizhansky, L.M. and Yakimov, S.P. (1974) Kinetics of disordering of distribution of Fe^{2+} in orthopyroxene structures. Dolkady Akademmii Nauk SSSR, 214, 909-912.

Koesterer, M. E., Frost, C.D. and Frost, B.R. (1985) Evidence for the presence of two supracrustal sequences in the Central Wind River Mountains. Geological Society of America, Programs with Abstracts, 17, 632.

Kohler, F. (1960) Zur berechnung der thermodynamoschen daten eines ternaren systems. Monatshefte fur Chemie, 91, 738-740.

Kretz, R. (1982) Transfer and exchange equilibria in a portion of the pyroxene quadrilateral as deduced from natural and experimental data. Geochimica et Cosmochimica Acta, 46, 411-421.

Kretz, R. (1981) Site-occupancy interpretation of the distribution of Fe and Mg between orthopyroxene and clinopyroxene in metamorphic rocks. Canadian Mineralogist, 19, 493-500.

Kretz, R. (1963) Distribution of magnesium and iron between orthopyroxene and calcic pyroxene in natural mineral assemblages. Journal of Geology, 71, 773-785.

Kretz, R. (1961) Some applications of thermodynamics to coexisting minerals of variable composition. Examples: orthopyroxene-clinopyroxene and orthopyroxene-garnet. Journal of Geology, 69, 361-387.

Lasaga, A.C. (1983) Geospeedometry: An extension of Geothermometry. Advances in Physical Geochemistry, 3, 81-114.

Lawson, C.A., Nord, Jr., G.L. and Champion, D.E. (1987) Fe-Ti oxide mineralogy and the origin of normal and reverse remanent magnetization in dacitic pumice blocks from Mt. Shasta, California. Physics of the Earth and Planetary Interiors, 46, 270-288.

Lindsley, D.H. (1983) Pyroxene thermometry. American Mineralogist, 68, 477-493.

Lindsley, D.H. (1981) The formation of pigeonite on the join hedenbergite-ferrosilite at 11.5 and 15 kbar: experiments and a solution model. American Mineralogist, 66, 1175-1182.

Lindsley, D.H. (1976) The crystal chemistry and structure of oxide minerals as exemplified by the Fe-Ti oxides; Experimental studies of oxide minerals. Reviews in Mineralogy, 3, L1-L88.

Lindsley, D.H. and Anderson D.J. (1983) A two-pyroxene thermometer. Proceedings of the Thirteenth Lunar and Planetary Science Conference, Part 2. Journal of Geophysical Research, 88, Supplement, A887-A906.

Lindsley, D.H. and Dixon S.A. (1976) Diopside-enstatite equilibria at 850 to 1400°C, 5 to 35 kbars. American Journal of Science, 276, 1285-1301.

Lindsley, D.H., Grover, J.E. and Davidson, P.M. (1981) The thermodynamics of the $Mg_2Si_2O_6$-$CaMgSi_2O_6$ join: a review and an improved model. Advances in Physical Geochemistry, 1, 149-175.

Lindsley, D.H., King, H.E., Jr. and Turnock, A.C. (1974) Composition of synthetic augite and hypersthene coexisting at 810°C: Application to pyroxenes from lunar highland rocks. Geophysical Research Letters, 1, 134-136.

Loomis, T.P., Ganguly, J. and Elphick, S.C. (1985) Experimental determination of cation diffusivities in aluminosilicate garnets. Contributions to Mineralogy and Petrology, 90, 45-51.

Matsui, Y. and Banno, S. (1965) Intracrystalline exchange equilibrium in silicate solid solutions. Proceedings of the Japan Academy, 41, 461-466.

May, L. (1971) An introduction to Mössbauer spectroscopy. Plenum Press, 203p.

McCallister, R.H. and Yund, R.A. (1977) Coherent exsolution in Fe-free pyroxenes. American Mineralogist, 62, 721-726.

McCallum, I.S. (1968) Equilibrium relationships among coexisting minerals in the Stillwater Complex, Montana. University of Chicago, Ph.D Thesis. 175p.

Mitre, G. and Frost, B.R. (1981) Mechanisms of deformation within Laramide and Precambrian deformation zones in basement rocks of the Wind River Mountains. Contributions to Geology, University of Wyoming, 19, 161-173.

Mueller, R.F. (1969) Kinetics and thermodynamics of intracrystalline distribution. Mineralogical Society of America, Special Paper, 2, 83-93.

Mueller, R.F. (1967) Model for order-disorder kinetics in certain quasi-binary crystals of continuously variable composition. Journal of Physics and Chemistry of Solids, 28, 2239-2243.

Mueller, R.F. (1962) Energetics of certain silicate solid solutions. Geochimica et Cosmochimica Acta, 26, 581-598.

Naeser, C.W. (1979) Fission track dating and geological annealing of fission tracks. In Lectures in Isotope Geology, Ed. Jager, E. and Hunziker, J.C., Springer-Verlag.

Nobugai, K., Tokonami, M. and Morimoto, N. (1978) A study of subsolidus relations of the Skaergaard pyroxenes by analytical electron microscopy. Contributions to Mineralogy and Petrology, 67, 111-117.

North A.C.T., Phillips, D.C. and Matthews, F.S. (1968) A semi-empirical method of adsorption correction. Acta Crystallographica, A24, 351-359.

Powell R. (1978) Equilibrium thermodynamics in petrology. John Wiley and Sons, New York, 543 pp.

Powell, R. (1985) Geothermometry and geobarometry: a discussion. Journal of the Geological Society of London, 142, 29-38.

Putnis, A. and McConnell, J.D.C. (1980) Principles of mineral behaviour. Geoscience Texts, Vol. 1, Elsevier, 257 pp.

Raedeke, L.D. (1982) Petrogenesis of the Stillwater Complex. PhD Thesis, University of Washington, Seattle, Washington, 212p.

Robie, R.A., Hemingway, H.S. and Fisher, J.R. (1978). Thermodynamic properties of minerals and related substances at 298.15 K and 1 bar (105 Pascals) pressure and higher temperatures. U.S. Geological Survey Bulletin, 1452, 456 pp.

Ross, M. and Huebner, J.S. (1975) A pyroxene geothermometer based on composition relationships of naturally occuring orthopyroxene, pigeonite and augite. International Conference on Geothermometry and Geobarometry, Extended Abstracts., Pennsylvannia State University.

Ross, M. and Huebner, J.S. (1979) Temperature-composition relationships between naturally occurring augite, pigeonite, and orthopyroxene at one bar pressure. American Mineralogist, 64, 1133-1155.

Rossi, G., Smith, D.C., Ungaretti, L. and Domeneghetti, M.C. (1983) Crystal-chemistry and cation ordering in the system diopside-jadeite: a detailed study by crystal structure refinement. Contributions to Mineralogy and Petrology, 83, 247-258.

Sack, R.A. (1980) Some constraints on the thermodynamic mixing properties of Fe-Mg orthopyroxenes and olivine. Contributions to Mineralogy and Petrology, 71, 257-269.

Saxena, S.K. (1983a) Problems of two-pyroxene geothermometry. Earth and Planetary Science Letters, 65, 382-388.

Saxena, S.K. (1983b) Exsolution and Fe^{2+}-Mg order-disorder in pyroxenes. Advances in Physical Geochemistry, 3, 61-80.

Saxena, S.K. (1982) Computation of Multicomponent Phase Equilibria. Advances in Physical Geochemistry, 2, 225-241.

Saxena, S.K. (1976) Two-pyroxene geothermometer: a model with an approximate solution. American Mineralogist, 61, 643-652.

Saxena, S.K. (1973) Thermodynamics of Rock Forming Crystalline Solutions. Springer-Verlag, Heidelberg, 182p.

Saxena, S.K. (1969) Distribution of elements in coexisting minerals and the problem of chemical disequilibrium in metamorphosed basic rocks. Contributions to Mineralogy and Petrology, 20, 177-197.

Saxena, S.K. (1968) Chemical study of phase equilibria in charnockites, Varberg, Sweden. American Mineralogist, 53, 1674-1995.

Saxena, S.K. and Dal Negro, A. (1983) Petrogenetic application of Mg-Fe^{2+} order-disorder in orthopyroxene to the cooling history of rocks. Bulletin de Mineralogie, 106, 443-449.

Saxena, S.K., Domeneghetti, M.C., Molin, G.M. and Tazzoli, V. (1988) X-ray diffraction study of Fe^{2+}-Mg order-disorder in orthopyroxene: some kinetic results (submitted to Physics and Chemistry of Minerals).

Saxena, S.K. and Eriksson, G. (1983) High temperature phase equilibria in a solar-composition gas. Geochimica et Cosmochimica Acta, 47, 1865-1874.

Saxena, S.K. and Ghose, S. (1971) Mg^{2+}-Fe^{2+} order-disorder and the thermodynamics of the orthopyroxene crystalline solution. American Mineralogist, 56, 532-539.

Saxena, S.K. and Nehru, C.E. (1975) Enstatite-diopside solvus and geothermometry. Contributions to Mineralogy and Petrology, 49, 259-267.

Saxena, S.K., Tazzoli, V. and Domeneghetti, M.C. (1988b) Kinetics of Fe^{2+}-Mg distribution in aluminous orthopyroxenes. Physics and Chemistry of Minerals (in press).

Schellekens, J.H. (1980) Application of the garnet-cordierite geothermometer and geobarometer to gneisses of Attu, SW Finland; an indication of P and T conditions of the lower granulite facies. Neues Jahrbuch Mineralogie Monatsheft, 1, 11-19.

Seifert, F. (1987) Recent advances in the mineralogical application of the ^{57}Fe Mössbauereffect. In Physical Properties and Thermodynamic Behaviour of Minerals. Advanced Study Institute, NATO, 687-704.

Seifert, F. and Virgo, D. (1975) Kinetics of Fe^{2+}-Mg order-disorder reaction in anthophyllites: Quantitative cooling rates. Science, 188, 1107-1109.

Sposato, K.A. and Besancon, J.R. (1987) Determination of the 500°C equilibrium Fe-Mg site distribution isotherm in orthopyroxenes by Mössbauer spectroscopy. Geological Society of America, Abstracts with Programs, 19, 853-854.

Stephenson, N.C.N. (1984) Two-pyroxene thermometry of Precambrian granulites from Cape Riche, Albany-Fraser Province, Western Australia. Journal of Metamorphic Geology, 2, 279-314

Stout, G.H. and Jensen, L.H. (1968) X-ray structure determination. A practical guide. Macmillan Co., 467p.

Sueno, S., Cameron, M. and Prewitt, C.T. (1976) Orthoferrosilite: high-temperature crystal chemistry. American Mineralogist, 61, 38-53.

Sykes, J.A. (1984) High-grade metamorphism of iron-rich bodies in Archean Gneiss, Wind River Mountains, Wyoming. Master of Science Thesis, University of Minnesota, Duluth, 131p.

Sykes-Nord, J.A. and Molin, G.M. (in review) Kinetics of Fe^{2+}-Mg order-disorder in orthopyroxene. Submitted to American Mineralogist.

Thompson, J.B. (1970) Chemical reactions in crystals: corrections and clarification. American Mineralogist, 55, 528-532.

Thompson, J.B. (1969) Chemical reactions in crystals. American Mineralogist, 54, 341-375.

Tokonami, M. (1965) Atomic scattering factors for O^{2-}. Acta crystallographica, 19, 486.

Turnock, A.C. and Lindsley, D.H. (1981). Experimental determination of pyroxene solvi for 1 kbar at 900° and 1000°C. Contributions to Mineralogy and Petrology, 19, 255-267.

Tweto, O. (1975) Laramide (Late Cretaceous-Early Tertiary) orogeny in the Southern Rocky Mountains. Geological Society of America Memoir, 144, 1-44.

Upadhyaya, G.S. and Dube, R.K. (1982) Problems in Metallurgical Thermodynamics and Kinetics. Pergamon Press, 252p.

Van Zeggeren, F. and Story, S.H. (1970) The Computation of Chemical Equilibria. Cambridge University Press, New York.

Virgo, D. and Hafner, S.S. (1969) Order-disorder in heated orthopyroxenes. Mineralogical Society of America, Special Paper, 2, 67-81.

Virgo, D. and Hafner, S.S. (1970) Fe^{2+}-Mg order-disorder in natural orthopyroxenes. American Mineralogist, 55, 210-223.

Wandless, M.-V. and Nord, Jr., G.L. (1986) Sample preparation techniques for Transmission Electron Microscopy of geologic materials. U. S. Geological Survey Open-file Report 86-255, 20p.

Wells, P.R.A. (1977) Pyroxene thermometry in simple and complex systems. Contributions to Mineralogy and Petrology, 62, 129-139.

White, W.B., Johnson, S.M. and Dantzig, G.B. (1958) Chemical equilibria in complex mixtures. Journal of Chemistry and Physics, 28, 751-755.

Wohl, K. (1953) Thermodynamic evaluation of binary and ternary liquid systems. Chemical Engineering Progress, 49, 218-219.

Wood, B.J. and Banno, S. (1973) Garnet-orthopyroxene and orthopyroxene-clinopyroxene relationships in simple and complex systems. Contributions to Mineralogy and Petrology, 42, 109-124.

Wood, B.J. and Holloway, J.R. (1982) Thermodynamic properties of minerals in the system CaO-MgO-Al_2O_3-SiO_2. Abstracts with programs, Geological Society of America, 14, 649.

Wood, B.J. and Nicholls, J. (1978) The thermodynamics properties of reciprocal solid solutions. Contributions to Mineralogy and Petrology, 66, 389-400.

Zachariasen, W.H. (1963) The secondary extinction correction. Acta Cristallographica, 16, 1139-1144.